ON THE CRYSTALLOGRAPHY OF BAINITIC TRANSFORMATION IN STEELS

ON THE CRYSTALLOGRAPHY OF BAINITIC TRANSFORMATION IN STEELS

By

Raheleh Hadian, M.Sc.

A Thesis

Submitted to the School of Graduate Studies

in Partial Fulfilment of the Requirements

for the Degree

Doctor of Philosophy

McMaster University

DOCTOR OF PHILOSOPHY (2013) McMaster University

(Department of Material Science and Engineering) Hamilton, Ontario

TITLE: On the crystallography of bainitic transformations in steels

AUTHOR: Raheleh Hadian, B.Sc., M.Sc.

SUPERVISORS: Dr. Gary R. Purdy, Dr. Gianluigi Botton

NUMBER OF PAGES: xviii, 132

Abstract

Bainite is a low temperature transformation product of austenite decomposition in steels. Its unique range of microstructures offers promising combinations of strength with ductility. At low transformation temperatures the crystallography of a phase transformation often plays an important role in the overall microstructure and how it develops. Therefore in this study the structures of ferrite/cementite and ferrite/austenite interfaces in bainite were investigated from a crystallographic viewpoint. After describing these interfaces, the idea of interphase boundary nucleation of cementite on a ferrite/austenite interface was investigated.

An O-line model (a special case of the O-Lattice) was used to explain the observed experimental results on orientation relationship, habit plane and good matching direction between ferrite and cementite. The calculated orientation relationship was used in an NCS (near coincident site) model to describe several possible edge facets of cementite precipitates. The major observed edge facet in cementite is deviated from the more favored interfaces based on the NCS model. This deviation could imply that the edge facets are non-equilibrium interfaces whose orientations and morphologies are kinetically determined.

Focused Ion Beam sectioning, conventional transmission electron and optical microscopy were used to shed more light on the three dimensional nature of a complex cementite-free bainitic microstructure. The faceted interfaces of bainitic ferrite were characterized and it was shown that the habit plane contains edge misfit dislocations. The orientation of the bainitic ferrite lath did not match an O-line model. Transformation time was considered to play an important role on the orientation and morphology of the bainitic laths and interfacial dislocation character.

Finally, with the aid of known crystallographic relations and interfaces between the ferrite/cementite, ferrite/austenite and austenite/cementite phases, a model for cementite nucleation was proposed. This interphase boundary nucleus is assumed to form on a

coherent ferrite/austenite interface and to possess ferrite/cementite and austenite/cementite calculated habit planes as two main facets surrounding the nucleus. It was shown that cementite nucleation would be viable if interfacial energies of all surrounding facets of a nucleus are in a semi-coherent energy range.

Acknowledgment

I would like to acknowledge my supervisors Dr. Gary Purdy and Dr. Gianluigi Botton for all their aid, their scientific support and inspiration during the course of my PhD over the last four years. I would also like to thank my supervisory committee member, Dr. Jeff Hoyt for his valuable scientific input and patience with my visitations and questions.

I'm highly indebted to Dr. Hatem Zurob and Dr. Marek Niewszas for their creative ideas and feedbacks.

My sincere gratitude goes to Dr. Wenzheng Zhang for providing me with the opportunity of visiting Tsinghua University, for her continuous help with my work and for all of our friendly discussions.

I would like to express my gratitude to CCEM staff for their help, especially to my humorous friend "Fred Pearson". I am very grateful to Elvira Evangelista, Diana Maltese, Jane Mah and Nanci Cole at the Materials department office for a pleasant friendship during the last four years.

My friends and family have always been kind and supportive of my work and I can't thank them enough. I specifically acknowledge my friends Xinfu and Damon for numerous discussions.

This work would not have been completed without the patience and support of my very special friend, Mostafa.

To:

J.S.Bach, *(for his cello suites)*

W.A.Mozart, *(for his requiem)*

S.V.Rachmaninoff *(for his piano concertos)* ***and***

Miles Davis *(for his" Ascenseur pour l'echafaud")*

Whose work composed my mind to write.

Declaration of academic achievement

1- "***On the crystallography of cementite precipitates in bainite'*** submitted to *Acta Materialia* on March 27, 2013.

The following papers are in preparation for publication:

2- "***Near coincident site modelling of cementite interfaces in bainite*** for publication in *Scripta Materialia*

3- "On the nucleation of cementite on ferrite /austenite interphase boundaries in bainite" *for publication in Acta Materialia*

The following published paper is the result of a collaborative work during the summer of 2011:

"Growth of austenite from as-quenched martensite during intercritical annealing in an Fe–0.1C–3Mn–1.5Si alloy"

Acta Materialia, Volume 61, January 2013, Pages 697-707

R. Wei, M. Enomoto, R. Hadian, H.S. Zurob, G.R. Purdy

Table of Contents

List of Figures

List of Tables

List of commonly used acronyms and symbols:

TEM	Transmision electron microscope
FIB	Focused ion beam
SEM	Scanning electron microscope
OR	Orientation relationship
WBDF	Weak beam dark field
HRTEM	High resolution transmission electron microscope
STEM	Scanning transmission electron microscope
BF	Bright field
DF	Dark field
PTMC	Phenomenological theory of martensite crystalloraphy
IPS	Invariant plane strain
ILS	Invariant line strain
CSL	Coincident site lattice
DSCL	Displacement shift lattice
EBSD	Electron backscattered diffraction
GT	Gibbs-Thomson
STM	Scanning-Tunneling microscopy
CBED	Convergent beam electron diffraction
NCS	Near coincident site lattice
KS	Kurdjumov-Sachs
NW	Nishiyama-Wasserman

IBP	Interphase boundary precipitation
G-W	Gibbs-Wulff
Cs	Spherical aberration corrected
$\mathbf{g}_i$	Reciprocal vector in crystal lattice i
$\mathbf{R}$	Rotation matrix
$\mathbf{A}$	Transformation strain matrix
$\mathbf{b}_i$	Burgers vector in crystal lattice i
$\mathbf{B}$	Bain strain matrix
$\mathbf{x}^o$	O-Lattice vector
$\mathbf{T}$	Displacement matrix
$\mathbf{G}_{CSL}$	CSL lattice in reciprocal space
$\mathbf{S}_{DSC}$	DSC lattice in direct space
$\Delta\mathbf{g}_i$	O-Lattice planes(Moiré planes) in crystal lattice i
$\mathbf{b}^*_i$	Reciprocal Burgers vector in crystal lattice i
$\mathbf{Oc}^*_i$	Reciprocal vector of the O-cell walls
$\mathbf{\Omega}_n$	Cubic symmetry matrix
μ_i	Chemical potential of component i
ΔG_m	Migration driving force on an interface
ΔG_v	Nucleation driving force
M	Intrinsic mobility
ΔG^*	Activation energy for nucleation
d_{dis}	Dislocation spacing
$d_{\mathbf{u}}$	Displacement of vector **u** after the transformation
$\boldsymbol{\varepsilon}$	Interfacial energy vector

γ	Scalar interfacial energy

Overview

Bainite has been the subject of study and also controversy for years. Different definitions of this transformation, each emphasizing a certain characteristic, have been proposed. Transformation kinetics, the morphology and crystallography of bainite have been studied several times and although the controversy still remains, the definitions and differences are not as distinct and sharp any more. The two major books on this phase transformation, "Bainite in steels" [1] and a more recent publication, "phase transformations in steels" [2], collect and summarize different works, ideas and interpretations on bainite. In spite of an enormous amount of documented research and discussion, there remain certain aspects of the bainite reaction that are not well understood. This thesis addresses several of these.

The focus of this work is the study of the crystallography of two well known types of bainitic microstructure: bainite with cementite and cementite-free bainite. The former microstructure was used to study the structure of ferrite/cementite interface and the latter was used to study the structure of ferrite/austenite interface and the morphology of cementite-free bainite.

The former microstructure (as developed in one of the alloys studied here and at the temperatures of interest) is composed of bainitic ferrite plates containing univariant cementite precipitation. The structural details of the ferrite/cementite interface in this microstructure, including the dislocation and/or step structure have not been previously reported. In addition, a unique aspect of cementite precipitation that can be attributed to a three phase relationship between ferrite, austenite and cementite on nucleation has not been rigorously described from a crystallographic and energetic viewpoint.

The latter microstructure, cementite-free bainite, is composed of bainitic ferrite and carbon-enriched retained austenite. Unlike the bainitic ferrite plates containing cementite, the two dimensional microstructure of cementite-free bainite in a random plane of section that is usually shown in the literature, can be exceedingly difficult to interpret. Depending on the transformation temperature and time, several interface planes rather than a distinct

habit plane is often observed in this case. Therefore, to characterize and interpret these interfaces, an overall understanding of the three dimensional microstructure of bainitic ferrite can be helpful. In addition, there are conflicting reports on the character of misfit dislocations of the ferrite/austenite interface in the literature. [3, 4]

In this study, diffraction contrast transmission electron microscope (TEM) will be used to study the details of the interfaces, described above. Also optical microscopes and scanning electron microscope (SEM) equipped with focused ion beam (FIB) will be used in this work to clarify the morphology of cementite-free bainite.

Geometrical modeling will be applied to interfaces under study to interpret the observations. Mainly, the O-Lattice construction [5-8] and the invariant line concept from martensite phenomenological theory [9, 10] will be utilized to rationalize the microscopic observations. Application of these geometrical models aims implicitly at minimizing the structural part of interfacial free energy.

After describing the ferrite/cementite interface, the idea of a three phase crystallographic relationship between austenite, ferrite and cementite will be explored to account for the unique variant of cementite precipitates in bainite. Eventually, the viability of thermodynamic nucleation of cementite on ferrite/austenite low energy interfaces at the temperature of interest in this work will be investigated.

In order to facilitate the understanding of the results and discussions of this study, **Chapter 1**, will give a brief summary of the relevant theories of this work. Basics of the theory and literature on the crystallographic rearrangement after a phase change, diffraction contrast microscopy, thermodynamics/kinetics of interface migration and finally bainite, the microstructure under study.

Chapter 2, describes the methodology used in this study; the experimental procedure and different types of models that were used.

In three different sections, **Chapter 3**, displays and discusses the results of the study of ferrite/cementite interfaces, austenite/ferrite interfaces and explores a model for the

nucleation of cementite on a semicoherent interphase boundary linking austenite and ferrite. At the end of each section the relevant results will be discussed.

Finally, **Chapter 4** summarizes the conclusions on the results and discussions of **Chapter 3** and offers suggestions for future work.

Chapter 1: Introduction

1- 1 Crystallography of precipitation

Phase transformations in solids are usually accompanied with a change of crystal structure. When an interface can be defined between the two crystal structures, the minimization of interfacial free energy plays an important role in the relationship between the crystallographic product and the parent.

At the product nucleation stage, the thermodynamic driving force should be balanced with the interfacial energy and elastic strain energy of the transformation. It is at this stage that an orientation relationship (OR) in the form of one matching direction and one or two matching planes, forms between the two phases.

The interfacial energy of an interface, between two dissimilar crystals has both chemical and structural components and, the latter has been considered to fall under 3 main categories, each associated with a range of values: coherent, semicoherent and incoherent interfaces (in order of increasing energy). The structural part of interfacial energy will be the main theme of this section.

To define an interface crystallographically, 5 degrees of freedom need to be fixed. These are of course the three variables* defining the OR and two variables defining the interface orientation. The OR usually exists between the coherent and/or semicoherent interfaces and the interface plane is usually sharp in these two types of interfaces. [5]

Fully Coherent interfaces of the phase transition products generally give rise to maximum elastic strain in the alloys. In such cases minimization of elastic strain energy is the key factor in determining the precipitate shape. An example of this case can be seen in particle splitting during coarsening of coherent ordered precipitates in nickel based super alloys. [11] On the other hand a semi coherent interface, relaxed after the introduction of

*Axis and angle of rotation

dislocations in the interface, is more likely to be influenced by the overall minimization of its interfacial energy. The latter form of minimization is the basis of many geometrical models that describe the precipitation crystallography and will be discussed in section 1-1-2. [12]

Crystallographic information that is required for any investigation on precipitation has been provided from X-ray diffraction and electron microscopy. The focus of section 1-1-1 will be diffraction and reciprocal space where most of the crystallographic data about the real space crystals are taken.

An orientation relationship between the parent and the product phase, depending on the symmetry of the parent crystal, can take various forms otherwise known as crystallographic variants. Lately the advances of electron back-scattered diffraction and synchrotron X-ray diffraction have made it possible to characterize different variants of an OR. Investigations on these different variants and their relationship were used for the first time to describe the zig-zag microstructure of martensite plates. [13]

Finally, in the last part of section 1-1-2 of precipitation crystallography, the theory and literature on orientation variants will be reviewed.

1-1-1 Diffraction and the reciprocal lattice

Electrons are scattered by both electrons and the nuclei in a sample [14] while X-rays are scattered only by electrons. Contrary to the field-field nature of the X-ray scattering, electrons directly interact with the specimen, both the electrons and the nucleus, and therefore they are scattered much more strongly and through smaller angles. To study diffraction, we are mainly dealing with elastic scattering. Namely, the diffracted wavelets have the same energy as the primary electrons or X-rays.

Von Laue won the Nobel Prize for the mathematical description of the diffraction process. Simply put, waves interfere constructively if they are in phase or if between the scattered waves from atoms have a path difference that is only an integer multiple of the

wavelength.[14] Later Bragg simplified his description with his famous formula for diffraction:

$$n\lambda = 2d\sin\theta_B \qquad \textit{Eq.1-1}$$

Where λ is the wavelength and θ_B is the Bragg diffraction angle. To understand diffraction better, the reciprocal lattice concept is used. d is the spacing between the planes. A plane in direct lattice corresponds to a vector **H** in reciprocal lattice.

In studying crystals we are dealing with periodic electronic densities. That may be written as:

$$\rho(\xi + \mathbf{a_p}) \equiv \rho(\xi) \qquad \textit{Eq.1-2}$$

The function $\rho(\xi)$ is the sum of plane electron waves where ξ is a position vector and $\mathbf{a_p}$ [†] is a unit translation vector in the crystal structure. Therefore the electron density can be represented as:

$$\rho(\xi) = \sum_H F(\mathbf{H})\exp(2\pi i\mathbf{H}\xi) \qquad \textit{Eq.1-3}$$

In which F (**H**) is called the structure factor. F (**H**) is the Fourier transform of the continuum electron density or it can be obtained from the sum of atomic scattering amplitudes of individual atoms in a unit cell. The latter is a discrete form usually used in crystallographic textbooks. (The nomenclature used here is from [12])

It should be mentioned that the intensity of diffracted beams is proportional to the square of the structure factor. X-ray diffraction techniques use this relationship and calculate the structure factor and therefore the electron density/structure of a sample using the measured X-ray intensity.

For *eq.1-2* to hold, exp ($2\pi i\mathbf{Ha_p}$) should be 1, hence:

$(\mathbf{Ha_1}) = h$, $(\mathbf{Ha_2}) = k$, $(\mathbf{Ha_3}) = l$ ***Eq.1-4***

[†] In this text, vectors and matrices will be represented by bold letters.

Where h, k and l are integers.

The solution of the above three equations are given by:

$\mathbf{H} = h\mathbf{a}^*_1 + k\mathbf{a}^*_2 + l\mathbf{a}^*_3$ where:

$$\mathbf{a}_1^* = \frac{\mathbf{a}_2 \times \mathbf{a}_3}{V} \qquad \textit{Eq.1-5}$$

$$\mathbf{a}_2^* = \frac{\mathbf{a}_1 \times \mathbf{a}_3}{V}$$

$$\mathbf{a}_3^* = \frac{\mathbf{a}_1 \times \mathbf{a}_2}{V}$$

In which $\mathbf{a}^*_1$, $\mathbf{a}^*_2$ and $\mathbf{a}^*_3$ are three non co-planar vectors that define a periodic lattice, reciprocal lattice and V is volume of the unit cell. Subsequently the reciprocal lattice point (h, k, l) can be shown to be a plane in crystal lattice normal to vector **H**.

The relationship between the plane wave with the propagation vector of $\mathbf{K_I}$ and the diffracted wave front vector $\mathbf{K_D}$, is expressed as:

$$\mathbf{K} = \mathbf{K_D} - \mathbf{K_I} \qquad \textit{Eq.1-6}$$

Figure 1-1a shows this construction schematically. The magnitude of the difference vector $|\mathbf{K}|$ is given by:

$$|\mathbf{K}| = \frac{2\sin\theta}{\lambda} \qquad \textit{Eq.1-7}$$

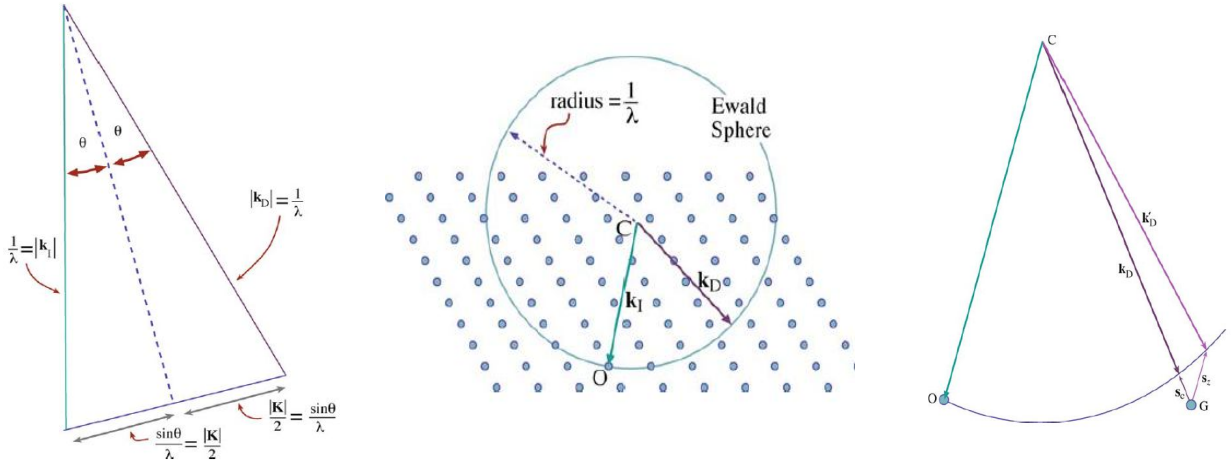

Figure 1-1a-Diffracted beam satisfying the Bragg rule. b-Ewald circle passing through a 2D reciprocal lattice. c- Diffracted beam with deviation parameter **s** from [14].

$\mathbf{K_B}$ associated with the Bragg angle θ_B is thus a special case of the above equation. In this special case, $\mathbf{K_B}$ is referred to as **g**, a diffracted beam, otherwise described as a plane in direct lattice. [14]

A very useful construction, involves an imaginary sphere in reciprocal space (the Ewald sphere) with the radius of $1/\lambda$ that passes through the origin of the lattice and cuts the reciprocal lattice points. According to this construction if any point in the reciprocal lattice intersects the surface of the sphere, it will satisfy the Bragg condition and will be diffracted strongly. The schematic figure of 1-1b, displays the Ewald sphere in two dimensions. Considering that typical electron wavelengths are orders of magnitude smaller than those of X-rays, the Ewald sphere intersects a larger volume of the reciprocal lattice in electron diffraction patterns.

The diffracted intensity of a diffracted spot in reciprocal lattice is a *rod* or a *relrod (reciprocal lattice rod)* and not a point, due to TEM samples' small thickness. Therefore, over a range of angles, the Ewald sphere intersects the *relrods* and diffracted points appear on the diffraction pattern. [14]

The deviation **s** from the exact Bragg condition is the reason why we can see reflections even when the Bragg condition is not exactly satisfied. So in other words, the deviation parameter **s** helps characterize the tilt of the incident electron beam or the sample. Figure 1-1c displays this deviation.

The deviation from the perfect Bragg condition is also the basis of an electron microscopy contrast technique that is useful in characterizing details of an interfacial structure; Weak beam dark field imaging. (WBDF)

Before discussing WBDF, two main diffraction concepts need to be defined: Diffraction contrast, which constitutes the basis of conventional TEM images and Kikuchi lines, a semi elastic scatter concept that is useful in determining the orientation of a crystal.

Diffraction contrast

Bright field (BF) and dark field (DF) imaging in TEM is based on diffraction contrast, in other words, the variation of contrast due to the diffraction intensity in the sample. The diffraction vector **K**, can be written as **g** + **s**. **g** is a reciprocal vector and **s** the deviation parameter. The appearance of the features in BF/DF images depend on three main parameters: **g**: which reflection is used for imaging and **s**: how much deviation from Laue/Bragg condition is and t the thickness of the sample. [14, 15]

"Diffraction contrast" is the form of contrast, usually used to study defects within and /or at the interfaces of crystalline phases. Alternative TEM contrasts such as "phase contrast" or "Z-contrast" are used when diffraction is not very strong, in high resolution TEM (HRTEM) and scanning transmission electron microcopy (STEM) imaging respectively.

To be able to interpret the contrast in TEM images, intensities of the diffracted beams should be calculated. Unlike the case of X-rays, in electron microscopes, this intensity cannot be used to determine the structure of the material because of the fact that the

electron beam gets re-diffracted multiple times in the sample, a phenomenon called *Dynamical diffraction*. Dynamic diffraction is due to strong coulomb interactions between the incident electrons and the atoms. In X-ray diffraction no such dynamics exists and in this sense X-rays diffraction is a pure Kinemtical *diffraction*.

Two basic equations, called the Howie-Whelan equations, can explain the intensity contrast in the images phenomenologically. Although from a rigorous physical point of view, electrons in a periodic potential, the crystal lattice, should be described as a wave function that keeps the symmetry of the crystal (Bloch waves. [14, 15]), for a qualitative interpretation, the following Howie-Whelan equations are appropriate:

$$\frac{d\varphi_{\mathbf{g}}}{dz} = \frac{\pi i}{\xi_{\mathbf{g}}}\phi_0 e^{-2\pi i \mathbf{sz}} + \frac{\pi i}{\xi_0}\phi_{\mathbf{g}} \qquad \textit{Eq.1-8}$$

$$\frac{d\varphi_0}{dz} = \frac{\pi i}{\xi_0}\phi_0 + \frac{\pi i}{\xi_{\mathbf{g}}}\phi_{\mathbf{g}} e^{-2\pi i \mathbf{sz}}$$

These two equations express how the amplitude of two beams, one direct and one diffracted beam, change when they enter the sample. φ_0 and $\varphi_{\boldsymbol{g}}$ are the amplitudes of the direct and diffracted beams that depend on each other's magnitude. *dz* is the thin slice of material (direction **z** is normal to the sample). ξ or the "extinction distance" is a characteristic length and is a function of the material (lattice parameter) and the accelerating voltage of the microscope and finally ***s*** is the deviation parameter that was introduced before.

Knowing that the intensities of direct and diffracted beams are complementary, $I_0 + I_{\mathbf{g}} = 1$ and $I \approx |\varphi_{\boldsymbol{g}}|^2$, many contrast features observed in planar defects such as stacking faults, grain boundaries and interphase boundaries can be explained.

Most defect analyses can be explained through both dynamical and kinematical diffraction. Whether kinematical or dynamical diffraction theory will apply depends on the thickness of the sample, t and the deviation parameter, **s**. The thinner the sample and

the higher the **s** value, the closer the diffraction condition will approach the kinematical regime. Both theories merge together when $|s_g| >> 1/\xi_g$ or when $t << \xi_g$. Details of the two theories and how they are applied to image contrasts are beyond the scope of this text and can be found in advanced microscopy textbooks. [15, 16]

Translations and strain fields

So far we introduced diffraction contrast for perfect crystals. Defects in crystals can be represented by their translations and rotation of the lattice or the strain fields they induce. We can use the Howie-Whelan 2-beam approach again to explain how these features create contrast.

If **R** is the translation (or distortion) caused by the defect, then the phase term in *eq. 1-8* will change to exp (±2πi(**sz**+**g.R**)) and unless **g.R** is zero, we will see a contrast caused by **R** in the images. α=2π**g.R** is called the phase factor. The vector **R** depends on the lattice parameter of the material and the type of defect. For stacking faults in f.c.c. R=1/3<111>. This analysis is used for the contrast study of stacking faults, antiphase boundaries and grain boundaries.

When studying the contrast from dislocations, **R** is not a fixed vector in contrast to translation in the above description. It changes with the distance *r* from the core of the defect. To understand the effect of a dislocation's strain field on the contrast, the column approximation is used in which the intensity of the beam is integrated in increments of dz of the sample over the total thickness. Figure 1-2 will clarify this point. For a dislocation instead of **g.R** we are interested in $\mathbf{g}.\frac{d\mathbf{R}}{dz}$. Based on figure 1-2 and for an isotropic solid, the displacement **R** for edge, screw and mixed dislocations can be expressed through equation 1-9 below, where r and φ are the polar coordinates, **b** is the Burgers vector, $\mathbf{b_e}$ the edge component of the burgers vector, **u** is the dislocation line and ν is the Poisson's ratio.

$$R = \frac{1}{2\pi}(\mathbf{b}\phi + \frac{1}{4(1-\upsilon)}\{\mathbf{b}_e + \mathbf{b}\times\mathbf{u}(2(1-2\upsilon))\ln r + \cos 2\phi)\})$$

Eq. 1-9

Two limiting cases of screw and edge dislocations can be studied from this equation, in the first case, $\mathbf{b_e}$=0 and **b** is parallel with **u** so **g.R** is proportional to **g.b** and in the latter **g.R** is proportional to **g.b**×**u.**

It should be emphasized that the above description applies to an isotropic solid while most materials we study are elastically anisotropic. So even if the **g**.**b**=0 or **g**.**b**×**u**=0, dislocations might have some weak residual contrast.

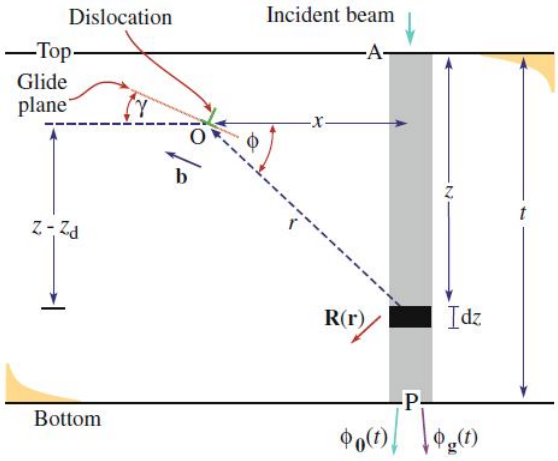

Figure1-2- Translation vector R , a distance r from the core of a dislocation from [14].

SAD and Kikuchi diffractions

The origin of a "Diffraction pattern" was briefly introduced with the Ewald sphere construction. The oldest diffraction pattern technique in TEM is selected area diffraction

pattern (SAD) for obtaining crystallographic information from regions of the radii as small as 0.5 µm with a parallel beam. A convergent beam diffraction pattern (CBED) otherwise known as microdiffraction is formed when the beam is focused and is obtained from regions as small as 10 Å in size.

Both techniques use highly symmetrical two dimensional patterns when the beam is oriented precisely along a crystallographic direction: the zone axis. A zone axis is a direction common to all reciprocal vectors, $\mathbf{g_s}$ (direct lattice planes) that are normal to that direction. These diffraction spots are the result of perfect elastic scattering events. When the samples are not very thin, inelastic and incoherent scattering can also contribute to the features observed in the diffraction patterns. The most important features of this kind are the *Kikuchi lines*.

Diffusely scattered electrons can be Bragg diffracted from (hkl) planes. Because we have a range of inelastic incident **K** vectors, there will be a pair of cones of diffracted beams. Near the optic axis, they appear flat with two bright and dark lines, called excess and deficient respectively.

Kikuchi lines and Kikuchi maps help in accurately (with an accuracy error of $\pm 0.5°$) defining the crystallographic orientations. The details of their applications have been discussed in many diffraction contrast textbooks including Edington's, Williams and Carter's, and Fultz and Howe's. [14-16]

Kikuchi maps can be calculated for both electron backscattered diffraction and TEM employing the dynamical theory of diffraction whereas spot patterns (Ex. SAD) are calculated on the basis of geometry and kinematical diffraction.

Among the tasks that the Kikuchi lines help facilitate, is determining $\mathbf{s_g}$, the deviation parameter.

Weak beam dark field imaging

Two beam, BF and DF imaging is usually used to image precipitates or defects. With DF of a certain reflection **g** centered on the optic axis, s_g (from now on the magnitude of the vector **s**) is adjusted to 0 (dynamical condition) so we can have the highest intensity in the image. When dislocations are to be imaged, the fact that their strain fields buckle the crystal planes around their core will facilitate their detection. In order to do so, dislocations should be imaged in a kinematical condition where the s_g is large for imaging reflection **g**, at locations where the crystal planes bend, Bragg's law can be satisfied locally around the dislocation line with s_g=0.

This process leads to the sharp imaging of dislocation lines but an overall weak background, hence the name.

In order to increase s_g, Kikuchi lines are positioned carefully so that s is greater $0.2nm^{-1}$. To ensure that a second reflection will be Bragg diffracted near the dislocation core, the related kikuchi line for a certain reflection needs to pass through the associated reflection.

By tilting the beam and moving **G** to the optic axis, we permit the reflection 3**G** to intersect the Ewald sphere; the Kikuchi line 3**g** will pass reflection 3**G**. That is why this condition is also called **g (3g)**. [14-16]

1-1-2 Theories of crystal rearrangement

When the crystal lattice of the product phase differs from the parent phase, a homogenous transformation strain can describe the crystal rearrangement. The strain is homogenous because it transforms lines to lines and planes to planes. [12]

The following equation described in the matrix format, summarizes a transformation of this kind:

$$\mathbf{A} = \mathbf{RB} \qquad \textit{Eq. 1-10}$$

$$\mathbf{x}_b = \mathbf{A}\mathbf{x} \qquad \textit{Eq. 1-11}$$

Where **R** is an orthogonal matrix, representing rotation and **B** a symmetric matrix, representing deformation. **x** is a vector in parent lattice, and $\mathbf{x}_b$ is **x** after the transformation. It has been proven that any non-singular (3 by 3) matrix can be factored in the above form. Since **B** is a symmetric matrix (Hermitian in a general sense), it can be diagonalized with eigenvalues λ_is as the diagonal elements. Subsequently principal strains are defined by (λ_i-1). The rotational part of **A** leaves the magnitude of vectors unchanged. Therefore **B** is enough to find unextended vectors after the application of **A**. This formalism is the core of the phenomenological theory of martensite crystallography.

The above transformation strain **A** is applied to vectors in a crystal. In order to find out how the plane normals change after a transformation, the reciprocal lattice transformation associated with **A** needs to be known. It can be shown that:

$$\mathbf{A}_r = (\mathbf{A}^{-1})' \qquad \textit{Eq. 1-12}$$

Where $\mathbf{A}_r$ is the transformation in the reciprocal lattice. **A** or $\mathbf{A}_r$ are matrix representations of an orientation relationship (OR) between the two crystals. Generally speaking, depending on the symmetry of the parent phase, there are multiple ways in which a single OR can be explained. If a symmetry operation is illustrated by an orthogonal matrix $\mathbf{G}_n$,

$$\mathbf{A}_n = \mathbf{G}_n \mathbf{A}_1 \mathbf{G}_n' \qquad \textit{Eq. 1-13}$$

where n refers to a symmetry operation and $\mathbf{A}_1$ is an arbitrary transformation strain. The number of possible transformations, from here on called, variants, depends on how many

‡ In the crystallographic texts, matrices will be expressed in bold capital and vectors in bold lower case letters.

§ ′ Refers to the transpose operation otherwise shown by T.

unique $\mathbf{A}_n$ can be produced from all applied $\mathbf{G}_n$. Further discussions on different variants of a phase transition will be presented in section 1-3.

Martensite Crystallography

Morphologically, martensitic phases are usually formed as thin platelets, needles or lath with well-defined interfaces. Martensite was proven to be a completely diffusionless transformation by Kurdjumov. [17] The product gives rise to a relief effect on the surface of the samples. This feature defines the displacive nature of martensite.

A well defined purely geometrical theory, phenomenological theory of martensitie crystallography (PTMC) explains the features of this transformation consistently.

The basic idea behind the PTMC is finding a specific net transformation strain geometrically that would lead to a zero-strain perfect matching (coherent) interface. [10] This transformation produces an Invariant Plane Strain (IPS). An invariant plane is a unique interface that can be depicted through eq. 1-14 in which **P** represents the IPS value $\mathbf{p}'$ is the invariant plane, **d** is the direction of displacement and **I** is the identity matrix.

$$\mathbf{P} = \mathbf{I} + \mathbf{d}\mathbf{p}' \qquad \textit{Eq. 1-14}$$

Based on experimental observations, a martensitic transformation is a homogenous transformation. Finding a homogenous transformation strain A that can explain an invariant plane is very rare, in fact it has only been observed in f.c.c. to h.c.p. transformations in Co.[10]

PTMC uses a combination of homogenous and inhomogeneous strains otherwise known as lattice variant and lattice invariant transformations to explain it. The simplified idea can be explained graphically in figure 1-3. If the parent phase is assumed to be a sphere, the ellipsoid is the deformed product that has been strained in the x_2 and x_3 directions. If there is no displacement in the x_1 direction (out of paper) the plane A′OC′ and B′OD′ can

be overlapped with AOC and BOD, if a rigid body rotation φ is added. This condition would lead to an IPS

This special deformation matrix, composed of one principal strain equal to 0 (along x_1) and the other two having opposite signs (along x_2 and x_3), does not exist in f.c.c.-b.c.c. martensite. The Bain strain constitutes the deformation matrix and it consists of three non zero principal strains as follows:

$$\mathbf{B} = \begin{bmatrix} \sqrt{2}\frac{a_b}{a_f} & & \\ & \sqrt{2}\frac{a_b}{a_f} & \\ & & \frac{a_b}{a_f} \end{bmatrix}$$

Where a_f and a_b are the lattice parameters of austenite and ferrite respectively.

Therefore a simple shear or twinning is the lattice invariant part of the transformation that helps create an IPS.

F.c.c.-B.c.c. martensite can be described by a deformation **B**, a shear $\mathbf{P}_2$ and a rigid body rotation **R**. The theory is phenomenological therefore mathematically, the order of physical events is immaterial. For simplicity we assume that shear $\mathbf{P}_2$ happens first and it makes the sphere tangent with the ellipsoid along x_1. Then the homogenous part, **RB**, easily creates an unextended , unrotated plane. In the following formula $\mathbf{P}_1$ is the final shape change:

$$\mathbf{P}_1\mathbf{P}_2^{-1} = \mathbf{RB} \qquad \textit{Eq. 1-15}$$

$$\mathbf{RB} = (\mathbf{I} + \mathbf{d}_1\mathbf{p}_1')(\mathbf{I} + \mathbf{d}_2\mathbf{p}_2') \qquad \textit{Eq. 1-16}$$

Where $\mathbf{d_1}$ and $\mathbf{p'_1}$ are the direction and plane of the shape change $\mathbf{P}_1$ and $\mathbf{d_2}$ and $\mathbf{p'_2}$ are the direction and the plane of shear $\mathbf{P}_2$. Both the shear and final shape change are IPS types of

transformation and their multiplication creates an invariant line strain, **RB**. Therefore, to solve the shape change $\mathbf{P}_1$ numerically, once the lattice parameters and correspondence between f.c.c., b.c.c. lattices are known, an assumption for plane and direction of the simple shear $\mathbf{P}_2$, enables the determination of $\mathbf{P}_1$ and the habit plane $\mathbf{p}'_1$. [9]

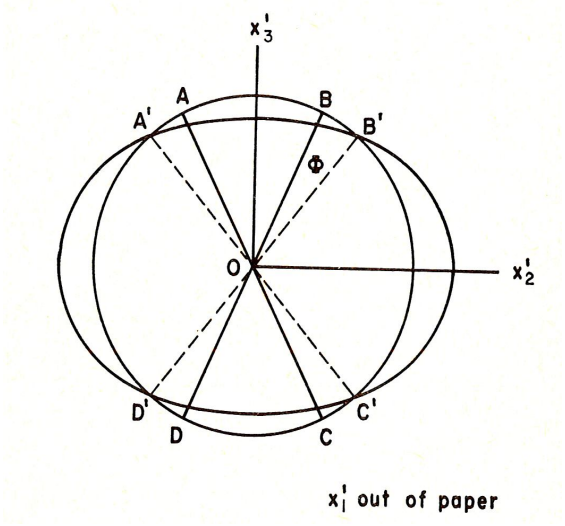

Figure1-3- Bain strain applied to sphere austenite, transforms it into an ellipse. AOB and A′OB′ represent initial and final cones of unextended lines from [9]

The algebraic details of martensite crystallography following the two well known approaches by Lieberman and Read, or Bowles and McKenzie are best described in Wayman's "Introduction to crystallography of martensitic transformations". [9] The first step in the calculation is finding invariant lines and invariant normals and this can also be done graphically using the stereographic analysis by drawing the initial and final cone of unextended lines and the trace of the shear plane. This stereographic construction will be used later in chapter 3 in order to describe a non-martensitic transformation.

Elements of the inhomogeneous part of the transformation have been observed experimentally using TEM. In plate martensite twinning shear and in lath martensite, slip shear in the form of screw interfacial dislocations have been observed to satisfy these inhomogeneities. [18]

In the treatment of Bowles and McKenzie, a dilatation parameter δ is added to **RB** to make the theory more flexible. When this parameter changes between 0.98 to 1.02, a distortion up to 2% is acceptable for the interface plane. Srinivasan and Wayman used such a parameter to apply PTMC to the bainitic transformation. [9, 19]

It can be shown based on a continuum approach for the calculation of the volume strain energy according to Khachaturyan [12] that given the stress free transformation strain, ε^0_{ij}, a martensitic product " with an infinitesimal thickness" will be the favorite shape for the transformation if volume strain energy were the defining criterion for martensite shape .

Invariant line strain (O-Line)

The application of PTMC to non-martensitic transformations has been the topic of investigations intended to explain transformations such as bainite and Widmanstaetten ferrite. Muddle and Nie [20] successfully applied PTMC to precipitation in Ag_2Al, AuCu and CuZn. Although the martensite theory has been confirmed by many experimental results, [9] this rare condition of transformation strain cannot always be found to explain the platelet microstructures that are often observed experimentally. Dahmen was the first to use the martensite crystallography concept of invariant line strain (ILS), which is a less demanding condition than invariant plane strain and apply it to many non-martensitic transformations extensively. [21, 22] It is worth mentioning that Invariant Line Strain (ILS) is the general form of IPS.

Dahmen [23] and Luo and Weatherly [24, 25] looked at the observed orientation relationships in Cu-Cr and Ni-Cr alloys and showed how, several experimental

orientation relationships can be explained as a combination of rigid body rotation **R** and a dilatational strain **S**, an ILS.

In his paper in 1982, Dahmen calculated the rotation necessary to produce an invariant line when the axis of rotation was the normal to close packed planes {111}f.c.c.//{110}b.c.c. and {0001}h.c.p.//{110}b.c.c., given different ratios of lattice parameters. The calculated ORs matched several experimental results but the approach was limited because it was two dimensional. [21]

A habit plane containing an invariant line and another direction of small misfit strain can minimize the elastic strain energy of a coherent nucleus. After the loss of coherency, the morphology of a semicoherent precipitate will be determined by interfacial energy considerations and growth conditions. [21]

The above suggestion from Dahmen explains the line that is usually drawn between the effects of interfacial energy vs. elastic strain energy in determining the equilibrium shape of a precipitate.

This distinction was not recognized later on by Luo and Weatherly [25] and Zhang and Purdy [6, 26] who used the invariant line theory in connection with the O-Lattice model by Bollman, [7, 8] to show that both models make the same prediction for the invariant line. The O-Lattice model was proposed based on the interfacial energy considerations. Interfacial energy minimization is the basis of almost all geometrical approaches that explain interfaces. It will be seen in the next section that the invariant line is only a specific form of an O-Lattice.

Geometrical modeling of interfaces: O-Lattice

One of the most comprehensive geometrical theories to describe the interfaces is the O-Lattice construction by Bollmann [8] that will be briefly discussed here. Frank [8] described the dislocation content of an interface between two crystals as follows:

$$\sum \mathbf{b}^{\mathbf{D}} = [\boldsymbol{\theta} \times \mathbf{x}] \qquad \textit{Eq. 1-17}$$

Where $\mathbf{b}^{\mathbf{D}}$ is the summation of discrete dislocations intersected by $\mathbf{x}$ **,** a vector on the boundary and $\boldsymbol{\theta}$ is an angle vector at the interface along the polar coordinate with the magnitude of θ. With this formulation the subgrain boundaries, for example the special cases of tilt and twist boundaries, can be explained. It has been proven that the accuracy of Frank's formula diminishes with increasing misfit between the two crystals. W. Bollman introduced a more general geometric theory called O-Lattice that explains the both the grain boundaries' and heterophase boundaries' structures. It can be shown that Frank's description is a special case of the O-Lattice. [8]

The O-Lattice was introduced to express the relationship between two lattices more mathematically and more generally than the existing rather discontinuous and limited approach of coincident site lattice (CSL[**]) theory. Each crystal structure can be described as:

$$\mathbf{u}_{\mathbf{k}} = e_i s^i{}_k \qquad \textit{Eq. 1-18}$$

Where $\mathbf{u}_{\mathbf{k}}$ are three unit vectors defined in an orthonormal coordinate system with 9 **s** components. There exists a general expression for the Structure matrix **s** that transforms all non cubic lattices to cubic coordinates. [7] In the following description, we use the matrix notation for simplicity. When two lattices 1 and 2 are interpenetrated, the O-points

[**] In short, CSL is a lattice composed of perfectly matching lattice points of the two crystals

are created. These matching positions do not just refer to lattice points as in CSL theory, but also to any internal point within a unit cell.

$$(\mathbf{I} - \mathbf{A}^{-1})\mathbf{x^o} = \mathbf{b}^L \qquad \textit{Eq. 1-19}$$

A is the transformation matrix and $\mathbf{b}^L$ represents lattice translation vectors referring to either of the two penetrating lattices. It can be shown that when the transformation consists only of rotation, $\mathbf{A}^R$, and the angle of rotation is small eq. 1-19 will match Frank's formula eq. 1-17.

To calculate the transformation strain **A** and O-points a common orthogonal coordinate will be defined between the two lattices based on a starting OR. Because there are multiple choices for **A**, the nearest neighbors in the two lattices will lead to $|\boldsymbol{I} - \boldsymbol{A}^{-1}|$ acquiring the smallest absolute value.

$$\mathbf{T} = (\mathbf{I} - \mathbf{A}^{-1}) \qquad \textit{Eq. 1-20}$$

T, defines the displacement between the two crystals. The solutions to the O-Lattice can be categorized into 3 main groups. If rank (**T**)=3, the O-lattice will be a point lattice, if rank (**T**)=2 it will be reduced to a line, O-line (previously introduced as invariant line) and finally if rank (**T**)=1, the solution is an O-plane. (Invariant plane strain in a martensitic transformation)

An O-line can also be called an invariant eigenvector of the transformation A.

$$\mathbf{Ax} = \lambda\mathbf{x} \qquad \textit{Eq. 1-21}$$

If in this case, the transformation conserves the length of a vector and the transformation is an invariant line strain. Bollman describes the possible translation vectors related to the O-elements (point, lines or planes) as forming a b-subspace onto which the O-elements are imaged.

Low index planes of O-Lattice, obtained by, $\mathbf{x^o}_1 \times \mathbf{x^o}_2$, will be good candidates for interfaces. Also good matching regions (O-elements) can be separated by cell walls. If the O-Lattice unit cell is large compared to the crystal lattice, these cell walls are physically meaningful. The intersection of the boundary planes with the cell walls, defines dislocations.

Even though, realistically, by disregarding the interatomic potentials and lattice elastic constants, exact atomic configurations are hard to predict, preferred ideal states can be used to describe interfaces.

When the lattice constants of the two crystals differ largely in magnitude, they belong to a *secondary preferred state*; otherwise a *primary preferred state* can explain the transformation. [7] In the former case the CSL sites are the reference state and in the latter either of the crystal lattices. In a primary state, for example, an f.c.c./b.c.c. case, the ideal semi- coherent interface would be an interface with coherent patches separated by lattice dislocations whereas in the former, for example in an f.c.c./orthorhombic (cementite and austenite in steels), fractional dislocations accommodate the misfit.

To describe the *secondary preferred state* a CSL between the two lattices is studied. Any translation vector in an ideal CSL that still preserves the same pattern of coincidence is a DSC [††]vector. These vectors form a lattice that contains allowed dislocation Burgers vectors in a secondary state.

A CSL/DSC construction is usually used on grain boundaries. To apply them to heterophase boundaries sometimes a lattice needs to be constrained. In such cases a constrained CSL/DSC is used to explain the transformation. [5] Constrained CSL/DSC will be used in chapter 3 to describe the ferrite/cementite interfacial structure. It should be mentioned that a CSL is a sublattice of an O-Lattice. Bollman extended the O-lattice formulation to include CSL as follows:

[††] DSC is the lattice of vectors that upon their translation, the symmetry and the structure of CSL remains unchanged.

$$\mathbf{T} = (\mathbf{I} - \mathbf{U}\mathbf{R}') \qquad \textit{Eq. 1-22}$$

Where **R** is rotation in orthogonal coordinate and **U** is a unimodular transformation so that rank (T) =3 (guaranteeing an O-Point lattice). In this case:

*det (***T***)=n/Σ* , where n is an integer and Σ characterizes a CSL and describes the volume ratio of CSL unit cell to crystal unit cell. It can also mean that 1/Σ of the atoms are in coincidence at the boundary. A convenient way of determining CSL and DSC lattices is through the diffraction pattern (reciprocal lattice) using Grimmer's [27] reciprocity relationship in eq. 1-23.

$$\mathbf{G}_{CSL}\mathbf{S}_{DSC} = \mathbf{I} \qquad \textit{Eq. 1-23}$$

G represents the CSL in reciprocal lattice and **S** represents DSC vectors in Real lattice. Ye and Zhang used CSL/DSC to describe their secondary interface structure in austenite/Widmanstaetten cementite. [28]

Hall et al. [29] applied the O-lattice concept to f.c.c./b.c.c. interfaces related by Nishiyama-Wasserman, Kurdjumov-Sachs and a range of orientation relationships between them. They calculated 7 habit planes (O-Lattice planes) and determined their favorability based on a P and R criteria, (related to the Burgers vector content of an interface and dislocation spacing) described by Ecob and Ralph. [30] Figure 1-4 shows the schematic simple diagram that depicts how O-lattice vectors and interface dislocations are related in their calculations. Their results of the structure and orientation of the habit plane is completely matching the computer models of f.c.c./b.c.c. by Rigsbee and Aaronson. [31]

Zhang and Purdy [6, 26] discuss the distribution of misfit on interfaces using the O-Lattice in both real and reciprocal lattices. They use the Moiré plane concept; high index planes that are formed by the mismatch of low index planes; to refer to O-lattice planes.

Moiré planes are normal to $\Delta\mathbf{g}$[#] (O-Lattice plane) in figure 1-5. They also find a solution for the reciprocal vector of O-cell walls in terms of the Burgers vectors. Therefore possible interface planes are described by:

$$\Delta\mathbf{g} = \mathbf{T}'\mathbf{g}_1 \qquad \textit{Eq. 1-24}$$

Where $\mathbf{g}_1$ is a reciprocal lattice vector, representing a plane in the reference lattice.

To define the cell walls, Bollman assumed that a point x on the wall, should have the same displacement from the two O-elements (point (000) and an adjacent O-point), thus:

$$\left|\mathbf{T(x)}\right| = \left|\mathbf{T(x - x_0)}\right| \qquad \textit{Eq. 1-25}$$

He reached a general expression for the cell walls that only had one distinct answer: $x=x^O/2$, the cell walls bisect the connecting line between the two O-points but are not necessarily perpendicular to the connecting line.

In other words, pairs of O cell walls, each corresponding to one $\mathbf{b}^L$, surround each O-point and the envelope of these walls forms an O-cell. [6] these walls are the O-Lattice transform of the Wigner-Seitz [§§] cell of the reference lattice. Zhang and Purdy define them by vector $\mathbf{Oc}^*$:

$$\mathbf{Oc}^* = \mathbf{T}'\mathbf{b}^{L*} \qquad \textit{Eq. 1-26}$$

Where $\mathbf{T}$ is the displacement matrix and $\mathbf{b}^{L*}$ is the reciprocal burgers vector.

[#] A reciprocal lattice vector that connects $\mathbf{g}_1$ from one lattice to $\mathbf{g}_2$ from the other.

[§§] Wigner-Seitz cell refers to a cell formed by perpendicular planes that are drawn at the midpoint of the lines between the lattice points.

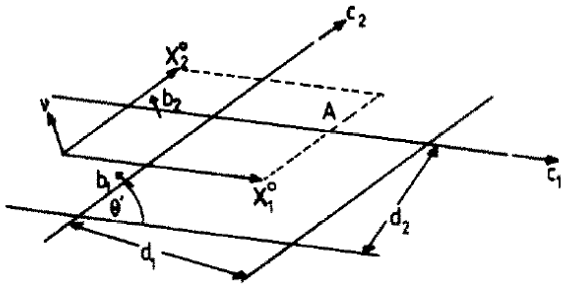

Figure 1-4- A simple representation of O-Lattice vectors and their correlated dislocations.x_1o and x_2o are the O-lattice vectors,c_1 and $c_2$the dislocation lines from [29].

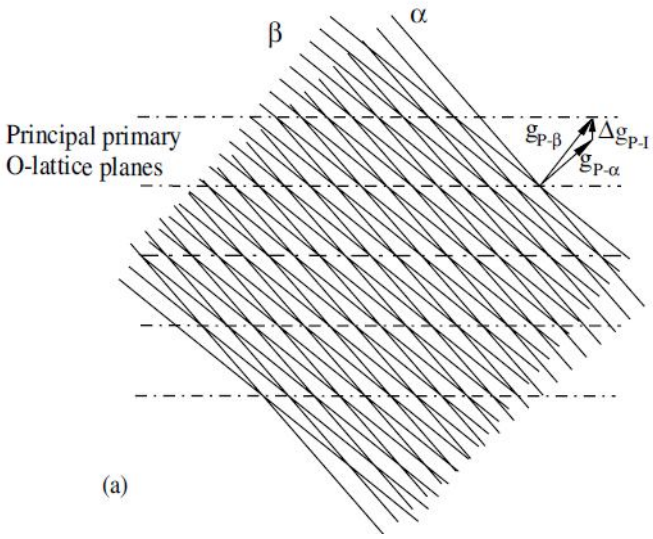

Figure 1-5- Moiré planes formed by gα and gβ lattice planes from [5].

They also show that the largest Δ**g** vector is associated with an O-Lattice plane that has minimum P and R value, in other words the most favorable interface from both the Hall et

al. and the Zhang and Purdy treatments are the same. Experimental evidence in Zr-Nb alloys also confirms this notion. [32]

A summary of other geometrical models

In the previous section the correlation between the predictions of an invariant line strain model and an O-Lattice model was emphasized. It was also mentioned that Hall et al. [29] concluded that the computer models of interfaces by Rigsbee and Aaronson [31] based on the good matching regions predict the same habit planes that they did in their analytical O-Lattice calculations. Rigsbee and Aaronson used a coherency criterion, of less than 3% of the nearest atomic distance[***] to show the good matching sites on f.c.c./b.c.c. close packed planes of {111}//{110}with variation in lattice parameter ratio and orientation relationships. They also incorporated “structural ledges" into their atomic models of interfaces.

Structural ledges were introduced by Hall et al. [33] to increase the frequency of repetition of the good matching sites on the interface. In this model, the criterion for the coherent patches is when the misfit between the nearest neighbors is less than 15%. The computer model of interfaces and the structural ledge model are both limited to two dimensional matching. Later Liang and Reynolds suggested a three dimensional near coincident matching to interpret their observed interfaces. [34]

Structural ledges help to explain the irrationality of the habit planes (deviation from rational close packed planes). The irrational habit planes of an O-Lattice model can also be attributed to ledges that rotate a habit plane from a terrace plane.

The agreement between a near-coincidence criterion, the O-Lattice and structural ledges arises from the fact that these models all predict favored interfaces as ones that contain a high density of good matching sites, higher spacing between dislocations, smaller Burgers

[***] When the spacing between the atoms in one phase and the adjacent atoms in the other phase is smaller than 3% of the nearest atomic distance in either lattice, the positions of these atoms are considered to lie within the coherent region.

vectors or lower step heights. (Sometimes these criteria are overlapping but overall an interface usually satisfies one of these criteria). Each of these models has limitations but because they are correlated, they can be used in a complementary way.

Recently Qiu et al. used an extended near-coincidence model to explain interfaces of a faceted precipitate in an invariant line strain system. [35] F. Ye et al. also described an edge interface in a Ti-Cr alloy using both the Moiré plane concept and near coincident sites. [36]

The elegant yet limited geometrical model of Cahn and Kalonji [37], describes the OR corresponding to interface facets, to be dictated by symmetry elements of both lattices.

Finally, Pond et al. use a topological model, otherwise known as the theory of disconnections, to explain transformation dislocations observed in martensitic phase/parent phase interfaces using HRTEM data. [38, 39]

Crystallographic variant analysis

It was discussed in section 1-2 that the symmetry of the parent crystal lattice would lead to multiple variants of an orientation relationship. Experimental electron diffractions can only give local diffraction information where as X-ray synchrotron or EBSD techniques provide us with all possible variants of an OR taken on the volume scales, up to a few cubic millimeters or cubic centimeters of a microstructure. Nolze [40] explains how one can generate a complete set of variants in an f.c.c./b.c.c. transformation, from a single variant using the cubic symmetry matrices $\mathbf{\Omega}_n$:

$$\mathbf{A}_n = \mathbf{A}\mathbf{\Omega}_n \qquad \textit{Eq. 1-27}$$

A parent cubic crystal with the point group symmetry of the type *m-3m* has 48 multiplicities[†††]. Because f.c.c. is centrosymmetric, 48 will be reduced to 24 independent symmetry elements. This would mean that in f.c.c./b.c.c. orientation relationship 24 different variants of the OR are expected, but if the OR is such that the symmetry elements of the two crystals overlap, the number of variants will be reduced even further. This is the reason why a KS[‡‡‡] orientation relationship in f.c.c./b.c.c. crystals has 24 variants whereas an NW[§§§] OR has 12. The calculated stereographic projections of figure 1-6 show the NW and KS variants of martensite on a [0 0 1] f.c.c. standard orientation. [41, 42] Using variant analysis, the relationship between the variants, their misorientation angle and axis, will be determined.

KS or NW variants can be written both based on symmetry matrixes. (Eq. 1-28) or by calculating rotation matrix with respect to one crystal lattice:

$$\mathbf{T}_1 = \mathbf{M}_1\mathbf{A}^{-1}{}_1 \qquad \textit{Eq. 1-28}$$

$\mathbf{M}_1$ describes the orientation of martensite in a 3 by 3 matrix in terms of austenite orientation matrix $\mathbf{A}_1$. By repeating this for all 24 variants on all {111} planes of austenite, the relationship between the variants, their misorientation angle and axis, will be determined.

In EBSD software, each orientation variant which is a rotation matrix is expressed through three Euler angles. These angles show the orientation of a certain variant with respect to a macroscopic coordinate. When an area on the scale of some square millimeters is scanned, an orientation map and its related pole figure can be drawn.

The experimental pole figures of martensite packets in a single grain of austenite similarly have shown 24 different variants of an OR, implying that upon complete transformation to lath martensite almost all variants of an OR appear in a single grain of

[†††] Multiplicity is the number of symmetry-equivalent positions in a unit cell.
[‡‡‡] Kurdjumov-Sachs (KS) OR describes the parallelism of : <1-11>b//<110>f and {011}b//{1-11}f
[§§§] Nishiyama-Wasserman (NW) describes the parallelism of : <100>b//<011>f and {011}b//{1-11}f

austenite. Experimental pole figures have often been compared with calculated pole figures to measure the deviation from a certain OR.

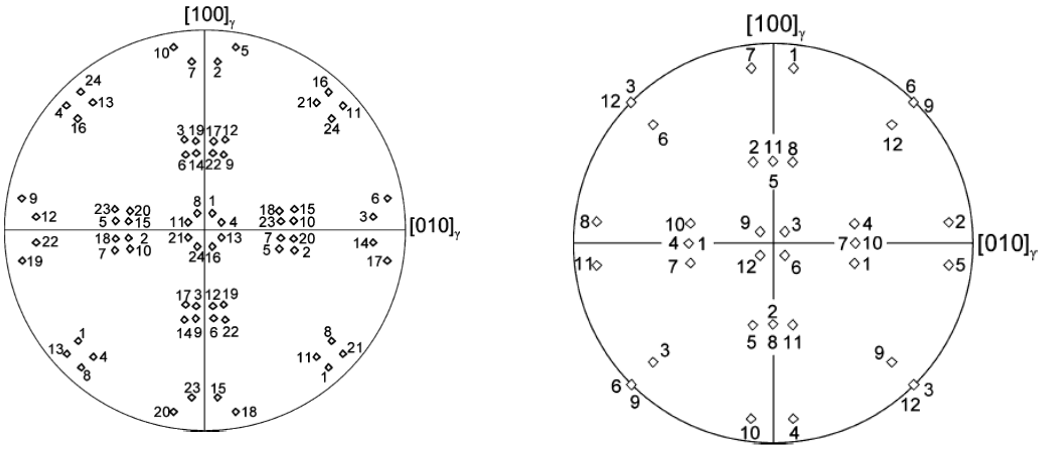

Figure 1-6a- 24 variants of a KS OR and b-12 variants of an NW OR from [41, 42].

Miyamoto et al. developed a method to accurately measure the OR in lath martensite and bainite when the austenite parent phase was no longer present. Their method uses the statistical data analysis and a numerical fitting procedure to find the orientation of the original grain of austenite (and consequently the orientation relationship between austenite and martensite) so that the deviation angle of all variants from a reference OR is minimal. [43]

Although the accuracy of the Kikuchi diffraction (when austenite is present) is higher than the above technique, it lacks the statistical value of a complete variant analysis. Also when the matrix nearby the precipitate is strained, as in martensite or bainite, the local OR would be affected.

Studying the relationship between precipitate variants might help shed some light on the possible variant selection processes. It is well known that plate martensite variants accommodate each other's shape strain by forming selective coupling between variants and in lath martensite 6 variants within a packet also reduce their total shape strain. [44]

1-2 Thermodynamics/Kinetics of precipitation

When dealing with first order phase transformations such as precipitation from a solid solution, two major processes determine the transformation kinetics; Nucleation and Growth. [45] For the nucleation to happen, the thermodynamic driving force needs to balance the generated surface energy and elastic strain energy. For growth to occur, the driving force will be dissipated in such processes as diffusion and interface migration. Nucleation and growth will be briefly summarized in this section. The growth process will be addressed first under the title of interface migration. Nucleation will be summarized later.

These topics will be of interest to this study in relation to diffusional transformations in α/γ/θ (ferrite/austenite/cementite) in steels.

1-2-1 Interface migration

Under constant temperature and pressure, one can equilibrate the driving force with the sum of all the dissipations of Gibbs energy to investigate the progress of a phase transformation. In a γ to α precipitation in steels many models have been proposed to predict how this driving force is being dissipated on the γ/α interface. Schematic figure 1-7, illustrates different portions of free energy dissipation, ΔG_i is the increase in molar energy due to surface tension, otherwise known as Gibbs-Thompson (GT) effect, ΔG_d is the portion dissipated by diffusion and ΔG_m corresponds to interface migration. [46]In other words the chemical driving force D can be written as follows:

$$D_{chem} = PV_m + \Delta G_d + \Delta G_m \qquad \textbf{Eq.1-29}$$

V_m is the molar volume of the precipitate and P is the increased pressure due to curvature.

(GT effect) In a sharp interface model, ΔG_m can also be assumed the driving force for the migration of an interface.

$$J^m V_m = v = M \Delta G_m \qquad \textbf{Eq. 1-30}$$

$$\Delta G_m = x_A{}^{\gamma/\alpha}(\mu_A{}^{\gamma/\alpha} - \mu_A{}^{\alpha}) + x_B{}^{\gamma/\alpha}(\mu_B{}^{\gamma/\alpha} - \mu_B{}^{\alpha}) \qquad \textbf{Eq. 1-31}$$

According to eq. 1-30, the net flux of atoms J_m causes the interface to move. The velocity of this moving interface depends on its intrinsic mobility M and the migration driving force ΔG_m and finally the migration driving force is related to the interface concentration through eq. 1-31.

ΔG_m is associated with interface structure (otherwise referred to as frictional resistance) and ΔG_d is related to trans- interface diffusion necessary for change in composition. In the presence of an alloying element X, the ΔG_d will be strongly correlated with a phenomenon at the moving interphase boundary called"solute drag". [47] When interface migration or solute drag constitute a non-negligible portion of free energy dissipation, assumption of local equilibrium at the interface, represented by eq. 1-32, will be violated.

$$\mu_i{}^{\alpha} = \mu_i{}^{\gamma} \qquad \textbf{Eq. 1-32}$$

Where the index *i* represents an element. In ternary systems of Fe-C-M, alloying element M will substantially influence both the thermodynamics of the transformation and the kinetics of interface. Different models have been proposed to explain the role of alloying elements. Two major models in the literature are, the local equilibrium approach with the assumption of eq. 1-32 and the paraequilibrium expressed by the following equations:

$$\mu_c{}^{\alpha} = \mu_c{}^{\gamma}$$
$$\mu_M{}^{\gamma} - \mu_M{}^{\alpha} = -(\mu_{Fe}{}^{\gamma} - \mu_{Fe}{}^{\alpha}).\frac{X_{Fe}}{X_M} \qquad \textbf{Eq. 1-33}$$

Models that describe a migrating interface in ternary systems generally need to take into account the effect of trans-interface diffusion and interface friction and relate those to interface kinetics. [48]

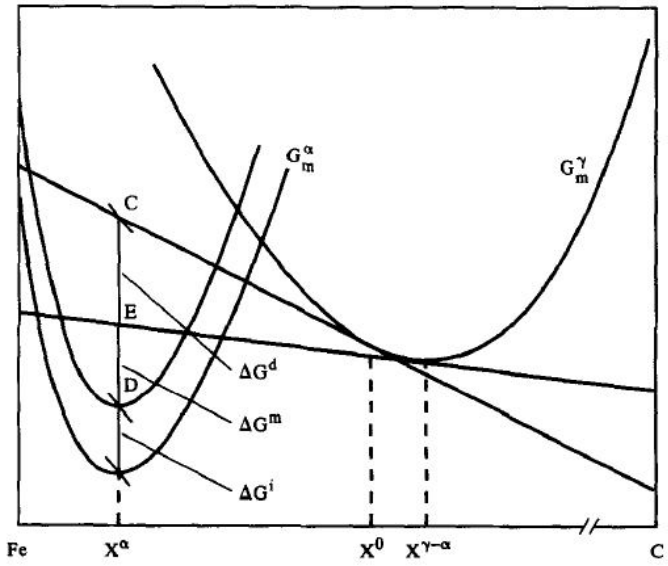

Figure 1-7-Schematic figure showing different portions of driving force dissipation at X^0 concentration. ΔG_i, ΔG_m and ΔG_d represent the curvature effect, dissipation through migration of interface and dissipation through diffusion respectively from [45].

1-2-2 Nucleation

Classical nucleation theory has been successfully applied to numerous precipitation systems. According to this theory nucleation rate is described by:

$$J^* = Z\beta^* N \exp(\frac{-\Delta G^*}{kT}) \exp(\frac{-\tau}{t}) \qquad \textit{Eq. 1-34}$$

Where N is the density of available sites for nucleation, Z is Zeldovich non-equilibrium factor[****], β^* is the rate at which atoms are added to the critical nucleus, ΔG^* is the free energy of activation for critical nucleus formation, τ is the incubation time, t is the reaction time and finally kT has its usual meaning. [49] Z, β^*, τ and ΔG^*, can be expressed based on the shape details of the nucleus and thermodynamic driving force ΔG_v. Nucleus shape is closely related to its crystallography. Johnson et al. [50] in their 1975 paper gave the most complete picture of this relationship. They calculated the nucleation rate for different faceted nuclei and concluded that reduced ΔG^* values by faceting may be the main reason why reproducible orientation relationships form between precipitates and their matrixes.

Jong Lee et al. [51] showed in a later study that, unless the ratio of strain energy to the driving force, ΔG_v, exceeds 0.75, the minimization of interfacial energy is enough to predict the equilibrium shape and in most precipitation cases this ratio is not reached.

To draw the equilibrium shapes for the nuclei based on surface energy considerations, the Wulff construction has been used in which ratios of perpendicular distances from the center of the crystal to its faces, equates the ratios of their interfacial energies. To obtain the Wulff construction a γ plot that is a scalar surface energy vs. orientation is drawn first. The inner envelope of planes, drawn normal to every point on the γ plot, forms the Wulff construction or the equilibrium shape of the crystal. Jong Lee and Aaronson generalized the Wulff construction to study a nucleus at the grain boundary that does or does not form a low energy planar facet with one of the boundaries. [52, 53]

Cahn and Hoffman introduced an $\boldsymbol{\varepsilon}$ vector analysis to replace the scalar γ plot and explain both isotropic and anisotropic nuclei at the boundaries. [54, 55] Main definitions of the $\boldsymbol{\varepsilon}$ vector are as follows:

[****] Zeldovich non equilibrium factor corrects for the fact that some clusters that have reached the critical size still decay to smaller sizes. It can be calculated through :

$$z = \{\frac{-1}{2\pi kT}(\frac{\partial^2 \Delta G_n}{\partial n^2})_{n^*}\}^{1/2}$$

$$\boldsymbol{\varepsilon}.\mathbf{n} = \gamma$$
$$\boldsymbol{\varepsilon}.d\mathbf{n} = d\gamma \qquad \textit{Eq. 1-35}$$

Where **n** is the unit normal vector specifying orientation of a surface element and γ is the interfacial energy per unit area. (It is implied that $\mathbf{n}.d\boldsymbol{\varepsilon}=0$)

The results of the application of this ε plot have been shown to be very similar to the generalized Wulff construction by Lee et al. [56]

1-3 Bainite

Bainite is generally known as a low-temperature product of eutectoid decomposition consisting of ferrite plates or laths with carbides precipitated either between or within the ferrite crystals. In terms of the overall reaction kinetics, bainite has its own C-curve on the TTT diagram, distinct from the pearlite curve (its position depending on the alloying element content). When the upper temperature limit of this curve is approached, the transformation becomes increasingly incomplete. Formation of bainite, like the formation of martensite, gives rise to a surface relief effect. [57]

There has been a lack of agreement and lively discussion on the nature of the bainitic transformation over the years. Initially the disagreement was focused on whether or not bainitic ferrite is a diffusional or a diffusionless (martensitic) transformation product. Researchers have proposed various ideas on the morphology, crystallography and kinetics of this transformation. Certain characteristics, for example, the overall slow kinetics of the transformation, are accepted by the majority of researchers. [1, 2] but concerning the mechanisms via which the microstructure develops there is no such convergence.

In the following two subsections, bainite will be discussed briefly from the microstructural and crystallographic perspectives. Detailed discussions on the kinetics of this transformation are not considered in the following.

1-3-1 Microstructures and their interpretations

Due to the complexity of the bainitic microstructure, many different and sometimes conflicting interpretations and reports exist in the literature.

Bainite can form with and without cementite precipitates depending on its Si content. Figures 1-8 a and b show two typical microstructures of bainite with and without cementite. In Si added alloys with no cementite, bainite has been observed via TEM to be composed of small faceted units lying in an overall sheaf structure. These sub-units were considered by Bhadeshia, Oblack and Hehemann [1] to form faster than would be allowed by carbon diffusion. It has also been suggested, based on Scanning Tunneling microscope (STM) observations (figure 1-9), that sub-units of bainite are also composed of smaller sub-units. [58] There have been suggestions that these sub-units might have formed autocatalytically or via sympathetic nucleation. [59, 60] Aaronson et al. also speculated the existence of smaller units of bainite that form through sympathetic nucleation, although they believed the kinetics of their formation was determined by carbon diffusion. [61] The changes in bainitic microstructure with temperature are gradual. At higher temperatures bainite resembles a sheaf of laths and at lower temperatures, a sheaf of plates. [2]

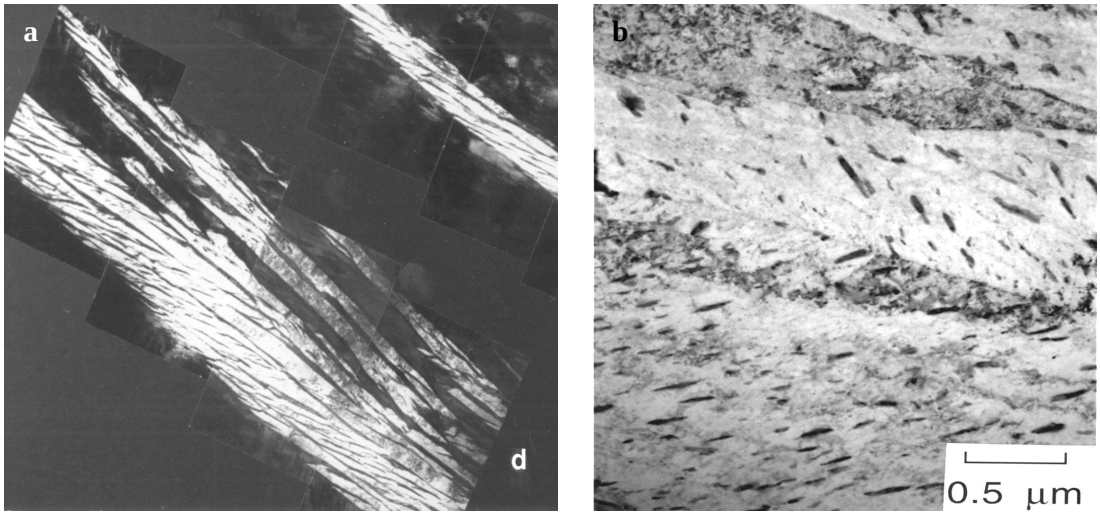

Figure 1-8a-A montage sheaf microstructure of bainite in silicon steel without cementite, b- microstructure of bainite with cementite from [1].

Some researchers placed emphasis on the similarity of bainitic microstructure to Widmanstaetten ferrite. Purdy and Hillert considered that all ferritic products are parts of the same continuous transformation sequence from austenite, but with decreasing temperature the degree of interfacial reaction control increases. [62] They believe that bainite is no different from Widmanstaetten ferrite when there is no cementite In fact they stated that the term “bainite” should only referred to a eutectoid microstructure and not to a mixture of ferrite plus austenite. [63] For simplicity in this text we refer to both microstructures; containing cementite and cementite-free, as bainite.

Without Si, cementite precipitates form within or outside a plate microstructure. This microstructure has been categorized by most studies as upper and lower bainite depending on the details of carbide precipitation and temperature of formation. [64] In these microstructures the appearance of sub-units has not been reported in the literature.. It has been suggested that carbides might have precipitated between the original subunits of ferrite in austenite, within the enriched austenite or on the interphase boundaries of ferrite

and austenite. [64, 65] [66] Borgenstam et al. used evidence from optical and replication electron microscopy to propose that cementite-ferrite phases grow side by side similar to a completely diffusional ledeburite microstructure in cast irons. [67] However, they believe that a lower baintic microstructure does not have the same level of cooperative growth between cementite and ferrite as pearlite and ledeburite.

No matter whether the smaller units of bainite are formed in a diffusionless manner or whether they develop by a process of diffusional growth,(similar to Widmanstaetten laths) , the interphase boundary nucleation of cementite could still occur. [2]

If the above argument about the precipitation of carbide is correct, the overall rather slow kinetics of bainite could be discussed as a combination of nucleation and growth of these subunits and nucleation and growth of cementite.

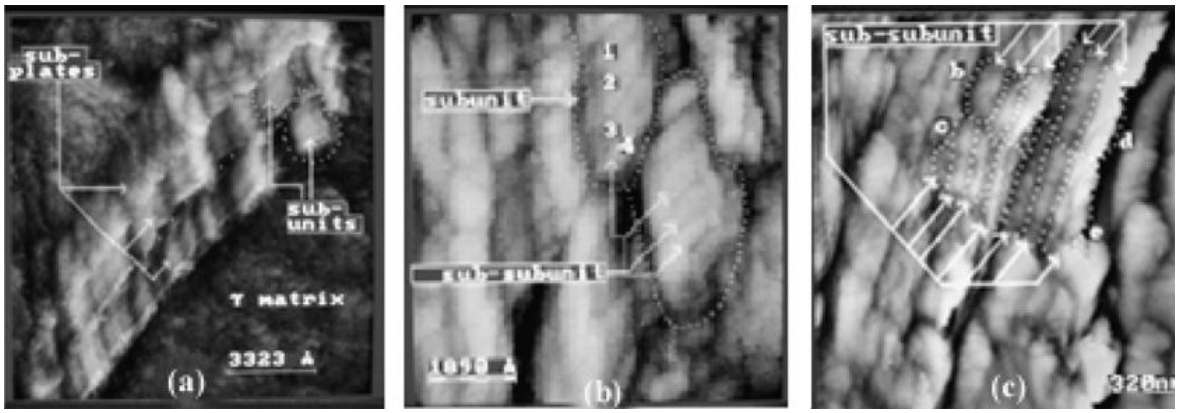

Figure 1-9- STM showing subunits and sub-subunits of a bainitic microstructure from [58].

However, Quidort and Brechet recently determined the overall kinetics of bainite with and without cementite and interpreted the results using the diffusion models of a plate growth by Trivedi. [68, 69] In other words, in their approach the entire bainite sheaf is treated as a single entity and no reference is made to the smaller units constituting the sheaf. They added the effect of cementite precipitation behind the growing front, assumed

that the cementite precipitates act as carbon sinks and reported a good agreement between the experimental TTT diagram and the calculated one. It should be mentioned that their measurements for plate growth was done on the optical microscope images of bainite.

The overall slow kinetics of bainite, in agreement with the diffusion of carbon, has been reported several times. [2]

1-3-2 Crystallography

The ferrite/austenite orientation relationship in bainite has been reported multiple times to be, similar to martensite and Widmanstaetten ferrite , a Bain[††††] related one. [19, 70]

Ferrite/cementite in bainite has been studied in detail by Kelly and Shackelton in 1961. [71] Both Isaichev and Bagaryatskii orientation relationships have been reported to describe ferrite/cementite relationship. [72, 73]

Moritani et al. studied the interfacial structure of ferrite/austenite in lath shaped bainite and lath martensite. They found a set of screw dislocations on the broad faces of bainite laths, similar to those reported for some martensites. [3] Previously, a sessile structure for the broad faces of bainite had been reported. [4]

Cementite in bainite is known to have similar crystallography to cementite in tempered martensite. The main difference between these two precipitation systems is that in tempered martensite, multiple variants of cementite have been observed and reported whereas in bainite mainly one variant of the OR is observed. [1]

To explain a similar orientation relationship and the unique variant of cementite precipitates in bainite, Srinivasan and Wayman [74] applied the phenomenological theory of martensite crystallography (PTMC) to the bainite transformation and concluded that {112}slip planes can explain the habit plane of cementite in bainite, ≈{112}b//(101)c.

[††††] NW or KS or any other relationship that originates from Bain correspondence.

On the other hand, it was speculated that if a particular variant of KS is obeyed by a ferrite/austenite interface and a particular variant of Pitsch OR is obeyed by an austenite/cementite interface, the resulting cementite/ferrite OR will be an Isaichev (or Bagaryatski) OR. [71] This unique relationship between the three phases, which can be satisfied in the interphase boundary nucleation of cementite on ferrite/austenite interface, can explain the appearance of a single variant of cementite within individual bainitic ferrite laths. Bhadeshia published a paper in 1980 [75], in which he concluded based on TEM results that austenite and cementite do not share a near Pitsch OR in bainite, and consequently, three phase matching described above does not exist.

Cementite/austenite with a Pitch[ǂǂǂ] OR [76] and cementite/ferrite with an Isaichev[§§§§] OR share the same terrace plane and the same invariant line in cementite. The similarity of the crystallography of the three phases would suggest the possibility of a three phase matching at the interface. The details of interface planes and structures between the three phases have not thus far been fully explained from an energy minimization point of view.

[ǂǂǂ] Pitsch OR: [1 1 0]f//[0 1 0]c, (2 -2 5)f//(0 0 1)c

[§§§§] Isaichev OR:[1 -1 1]b//[0 1 0]c, (1 1 0)b//(1 0 3)c

Chapter 2: Experimental procedure and methodology

2-1 Experimental Procedure

2-1-1Heat treatment

Steels samples A, B, C compositions are described in table 2-1. A and B samples were austenitized at 980°C and held at 350°c for 10 minutes to isothermally transform to bainite in a salt bath furnace . They were then quenched in brine. Steels A and B were used to study bainite with and without cementite respectively using TEM.

Steel A was austenitized at 980°C, quenched in brine and then tempered at 210° for 30 minutes to produce steel D. Steel C was austenitized at 980°C and held at 350°c for 3, 6, 10, 20, 40 and 80 minutes to study the development of a cementite- free bainite microstructure with time using optical microscopy a scanning electron microscope (SEM) equipped with focused ion (FIB) beam machining capability . Steel A was used to study ferrie/cementite interfaces and steel B and C were used to study ferrite/asuentite interfaces and the general morphology of cementite-free bainite. Steel D was used to study a tempered martensite microstructure.

Table 2-1- Compositions of steels used in the experiments

Steel	Composition (Wt %)
Steel A	0.5% C, 5% Ni, Fe Bulk
Steel B	0.5% C, 5% Ni, 1.8% Si, Fe Bulk
Steel C	0.5% C, 3% Mn, 1.8% Si, Fe Bulk

2-1-2 Sample preparation

Optical microscope and SEM samples were polished and etched using a special etchant developed in *ArcelorMittal* containing 14 g of $NaNo_3$, 40 g of NaOH and 60 g of H_2O. This etchant has been shown to distinguish clearly between ferrite (etching white) and martensite (etching brown). [77]

TEM samples were first chemically polished to ≈ 50 μm in a HF, H_2O_2 and H_2O solution and then jet polished to 50-100 nm in an electrolyte of 10% perchloric and 90% high purity methanol at 25-28V and -50°C. 3 mm disks were then punched from the thinned specimens. These conditions were chosen after several trial and error experiments with different conditions.

2-1-3 Instruments

Lattice parameters of austenite and ferrite were measured using a Bruker-AXS Smart APEX2 diffractometer with Mo source. *TOPAZ* Phase analysis software was used to fit the x-ray peaks and to find the most appropriate lattice parameters.

Table 2-2 lists the lattice parameters.

A Zeiss Axioplan Optical microscope was used along with *Northern Eclipse* image analysis software to study the microstructure development in steel C.

A Zeiss Nvision 40 double beam machine, SEM and FIB, was used for both imaging and sectioning samples of steel B to study the 3D microstructure of bainitic ferrite. The cut cross section images were taken in an ion beam imaging mode because of the visibility of the crystallographic contrast (grain contrast) in the ion mode. These images were then edited and 3D volumes were generated from the microstructure of interest in *AMIRA 5.3.3* software.

The crystallography of bainitic ferrite precipitates in an austenite matrix and cementite precipitates in the ferritic matrix were then investigated using a three lens CM12 Philips 120kV conventional TEM and a Cs corrected high resolution microscope, Titan, operating at 300kV.

Table 2-2-Experimentally determined lattice parameters of ferrite and austenite.

Austenite lattice parameter(Å)	3.6154
Ferrite lattice parameter(Å)	2.8664

2-1-4 Calibration of image and diffraction pattern

The relationship between the image and diffraction pattern can vary in a complex way by changing the magnification in the image mode and camera length in the diffraction mode. It is necessary to calibrate the rotation between the two. The procedure for the calibration has been well documented on MoO_3 crystals for years.

In MoO_3 orthorhombic faceted crystals, the long edges are normal to the smallest spacing in <1 0 0> zone axis. Double exposure image and diffraction patterns are taken to determine the rotation angle between the two. In addition to rotation angle, sometimes inversion is also present between the image and the diffraction pattern. This inversion (rotation angle $\theta \pm 180°$) can be determined by underfocusing the diffraction lens so that the image of the specimen will appear in the diffraction mode. The diffraction pattern is not inverted in the underfocused mode and the relationship will be apparent. [78]

2-1-5 Orientation measurement

Selected area diffraction pattern (SAD) and convergent beam diffraction pattern (CBED) were used for measuring the angular relationship between the planes and directions in the two crystals at the interface, respectively. The error in SAD patterns will be mainly caused by the contribution of areas outside the aperture to the diffracted beams. So the smallest area that can be used for SAD diffraction is 1μm.

Convergent beam diffraction was used to obtain Kikuchi patterns. The orientation of the beam (the direction in the crystal) can be determined with an accuracy of 0.5° using the Kikuchi lines. The convergent beam was generated by focusing the beam and reducing the probe size (and not by using a large condenser aperture in order to avoid overlapping diffracted discs). In this way, information can be recorded from areas as small as a few nanometers. [78]

To obtain the overlapped SAD patterns, the aperture was placed on the image of the boundary between the two phases. To obtain the orientation of the beam in each of the adjacent crystals, convergent beam diffraction patterns with Kikuchi maps were taken on both sides of the boundary.

2-2 Crytallographic modelling

Lattice parameters of ferrite, austenite and cementite that were used in the crystallographic models are shown in table 2-3. Cementite has an orthorhombic crystal structure with *Pnma* space group and 12 atoms of iron and 4 carbon atoms. Figure 2-1 depicts the cementite crystal.

The theory of geometric modeling of interfaces was summarized in chapter 1. More specific details about the models that have been used in this study will be discussed here. The application of the crystallographic models of 2-2-1 and 2-2-2 to ferrite/cementite interfaces will be discussed in the next chapter, section 3-1.

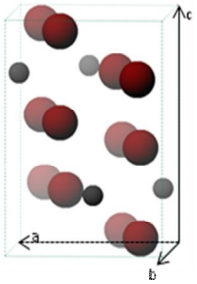

Figure 2-1- Orthorhombic cementite with iron(red) and carbon(black)atoms.

2-2-1The O-line model

Zhang and Purdy [6, 26] developed the invariant line transformation further by incorporating the two-dimensional O-Lattice idea of Bollman, (named the O-line model), to interfaces containing invariant lines and introduced several useful relationships in reciprocal space. Invariant line theory alone does not have a dislocation description but the O-line model does. Zhang and Purdy proposed that an interface with a periodic structure of the O-lines (invariant lines) separated by parallel dislocations along these lines will be the optimum interface. The O-line lattice is a special case of the O-lattice and the principal O-lattice planes containing periodic dislocation structures are possibly associated with local minimum of interfacial energy. [79] They used the concept of Moiré planes (described in section 1-1-2) in relation with the O-Lattice planes to identify interfaces. In other words, O-lattice planes are identical to Moiré planes.

It has been shown numerous times that the application of the O-line model in reciprocal space can yield information about the direct lattices because the main source of crystallographic data are usually the diffraction patterns. Recently, Zhang et al., in [80] and [28] rationalized and discussed the structure of austenite/Widmanstaetten cementite interfaces in hypereutectoid steels as reported by Howe and Spanos. [81]

In this investigation, an O-line model was used to calculate the precise orientation relationship between ferrite/cementite crystals in bainitc ferrite of sample A. Lattice parameters of austenite and cementite Zhang et al.'s study [28] were used here to enable us to compare cementite /ferrite interfaces with austenite/cementite interfaces.

Table 2-3- Lattice parameters used in crystal models.

Austenite	a=3.6 Å
Ferrite	a=2.86 Å
Cementite	a=4.52 Å, b=5.09 Å, c=6.73 Å

2-2-2 The NCS model

The "Near coincident sites" concept was briefly introduced in chapter 1. Because the O-Lattice cannot be solved in three dimensions for an orientation relationship that permits O-lines, a near coincident site model (NCS) can be used to identify optimal interfaces other than the habit plane. A good candidate for an interface usually contains a high density of good matching sites or near coincident sites. [34-36] Hall et al. [33], used the basic idea of an NCS model to define coherent regions for which dissimilar atoms at the interface are within the 15% of the nearest neighbor distance, in their investigation on f.c.c.-b.c.c. near coherent boundaries. Later Rigsbee and Aaronson [31] used a 3% (of the nearest neighbor distance) criterion to find the f.c.c.-b.c.c. habit planes by changing the lattice parameter ratio of ferrite/austenite and their Bain related ORs. They considered different layers of close packed planes {111} f// {110} b to find the NCS.

Liang and Reynolds [34], F.Ye et al. [36] and D.Qiu and Zhang [35] applied a 3D NCS model (a 3D network of atoms from both crystals was constructed) to their precipitation systems to explain their experimental dislocation structures. Even though an NCS model

does not explicitly reveal the dislocation details of an interface, when used with the O-Lattice formulation and Moiré plane concept, it can provide a model for the detailed interfacial structure.

The precise O-line OR of the previous section, was used as an input for the calculation of the near coincident sites (NCS) in 3 dimensions. 15% of the nearest neighbor distance is the commonly used criterion of matching and that was used to specify the good matching sites in this study. That is to say , after superimposing the interpenetrating two lattices, if the adjacent ferrite and cementite atoms lie closer than 15% of the length of $<111>_{b.c.c.}/2$, they are considered near-coincident or good matching sites. To calculate the good matching atoms in this study, all the atom positions of cementite crystal were taken into account and not just its lattice positions.

The results on ferrite/cementite interfaces will be discussed in chapter 3 section 3-1.

2-2-3 Austenite/ferrite interface

The experimental results on ferrite/austenite interfaces of steels B and C, including the optical/SEM and TEM results will be discussed in chaper 3 section 3-2. A FIB sectioning experiment, further discussed in chapter 3, was done to shed more light on the three dimensional nature of the bainitic ferrite microstructure in steel B. In an attempt to understand f.c.c./b.c.c. TEM results, an f.c.c./b.c.c. O-line model (based on martensite crystallography) [82] was used. Appendix C lists the details of this model that was originally used by Qiu and Zhang to explain a similar transformation in duplex stainless steels.

2-2-4 Three Phase Crystallography

Cementite in both bainite and tempered martensite shares an Isaichev/Bagaryatskii orientation relationship, described below, with ferrite.

[0 1 0] c//[1 -1 1] b

(1 0 3) c//(1 1 0) b Isaichev or (2 0 0) c// (0 1 1) b Bagaryatski

The similarity between cementite precipitation in bainite and tempered martensite, briefly explained in chapter 1 section 1-3, is the reason that their crystallography will be compared in this study. The main difference between the precipitation crystallography of cementite in bainite and tempered martensite is the number of cementite variants of the above orientation relationships that appear in the ferritic matrix. In tempered martensite, multiple variants of cementite have been reported whereas in bainite, mainly one variant of the OR is observed. [1] This observation has led to the idea of interphase boundary nucleation of cementite and a consequent three phase lattice matching of austenite, ferrite and cementite at the interface. In Chapter 3 section 3-3, details of a three phase crystallography (lattice matching between the three phases on the basis of 1-the three phase orientation relationship; and 2- the three phase interface plane matching) will be discussed first.

Assuming that interphase boundary nucleation is operative and based on morphological observations in carbide-free bainite, a theoretical model for cementite nucleation will be investigated. The main motivation for this idea discussed in chapter 3 section 3-3 is incorporation of the crystallography of interfaces in thermodynamics/kinetics of a phase transformation.

Methodology

The reciprocal lattice is the starting point for the calculation of a geometrically favored interface. It will be shown in the next chapter that the crystal structures can be described in an orthogonal coordinate system and using an O-line model the orientation relationship between them and subsequently the habit plane and the O-line direction are calculated. The OR is then used as an input in an 'NCS' model to find favored interfaces other than the habit plane. Considering that both cementite/ferrite and cementite /austenite can be described with O-line models, a three phase crystallographic relationship among them will be discussed. All of the crystallographic calculations using Bollman's O-Lattice theory and Zhang's modifications and crystallographic variant analysis have been done in *MATLAB*. As an example, the main algorithm for finding the good matching sites on the interface and the related *MATLAB* code are described in Appendix A.

2-3Thermodynamic/Kinetic modeling

The simple idea describes the nucleation of cementite on the faceted interphase interfaces of ferrite/austenite. Interfacial carbon concentration is assumed to approach paraequilibrium during ferrite growth process. The analysis does not extend to cementite growth, either independently or in cooperation with ferrite, but speaks only to the probability of cementite nucleation on a low-energy ferrite/austenite interface.

Methodology

A diffusional model originally developed to calculate the thickening kinetics of ferritic allotriomph was used for the calculation of moving interphase interface concentration versus time. Because of the lack of definite data in the literature on the mobility of faceted interfaces, the experimentally verified incoherent interface mobility has been used in the model. This mobility value is an upper limit of the actual mobility of low energy ferrite/austenite interface of our study.

Details of the diffusional model will be described in Appendix B.

The driving force for cementite precipitation in a paraequilibrium state between cementite and austenite was extracted from Thermo-calc version S. This thermodynamic driving force will be used in a classical nucleation model on the faceted f.c.c./b.c.c. interfaces to investigate the possibility of nucleation.

ΔG^*, the free energy of activation for critical nucleus formation, will be the determining factor in the investigation because of its importance in the calculation of the nucleation rate. [50] (eq. 1-33). A model of a cementite nucleus, having equilibrium faceted interfaces with both ferrite and austenite is developed. The faceted interfaces are the equilibrium habit planes determined through the O-line model, and by this means, crystallography is incorporated in the nucleation model.

The results of this section will be discussed in chapter 3 section 3-3.

Chapter 3: Results and discussion

The results on ferrite/cementite interfaces in bainite in steel A (bainite containing cementite precipitates) will be presented in section 3-1. The observations on ferrite/austenite interfaces of steels B and C (cementite-free bainite), will be summarized in section 3-2. In the last section, the multivariant appearance of cementite in tempered martensite will be compared with the univariant cementite in bainite. With the assumption of an interphase boundary nucleation, the crystallography of the three phases at the boundary and a model for the nucleation of cementite will be discussed.

3-1 Ferrite/Cementite interface

3-1-1 Application of the O-line model

Figure 3-1a is a magnified image of a cementite precipitate at [0 1 0] c// [1 -1 1] b and its correlated zone axis diffraction pattern. As can be seen from the diffraction pattern of figure 3-1b, the habit plane of cementite is close to (1 2 1)b//(3 0 3)c, at positions where the interface is sharply defined (interface is edge on). The trace of the interface is shown in figure 3-1c. However, a general view of multiple precipitates in several ferrite plates suggests a not very well-defined interface outline, which may explain other reported interface facets in the literature. [65] The variant of orientation relationship, which is close to Isaichev OR, in this figure, will be consistently used throughout this text.

The first stage in the discussion of the transformation crystallography is the calculation of the expected OR, according to an O-line model via the observed correlation between the planes in the observed diffraction pattern. One constructs a common orthogonal coordinate system in reciprocal space as displayed in figure 3-1b. In reciprocal space each reflection **g** represents a plane in each of the crystal lattices. $\mathbf{G}_{\alpha}$ and $\mathbf{G}_{\theta}$, composed of 3 non co-planar vectors; were defined in the orthogonal coordinate system and are correlated in the two crystal lattices based on the experimental orientation relationship.

The transformation strain in reciprocal lattice $\mathbf{A}_r$ will be determined by adding rotation to eq. 3-1 as in eq. 3-2.

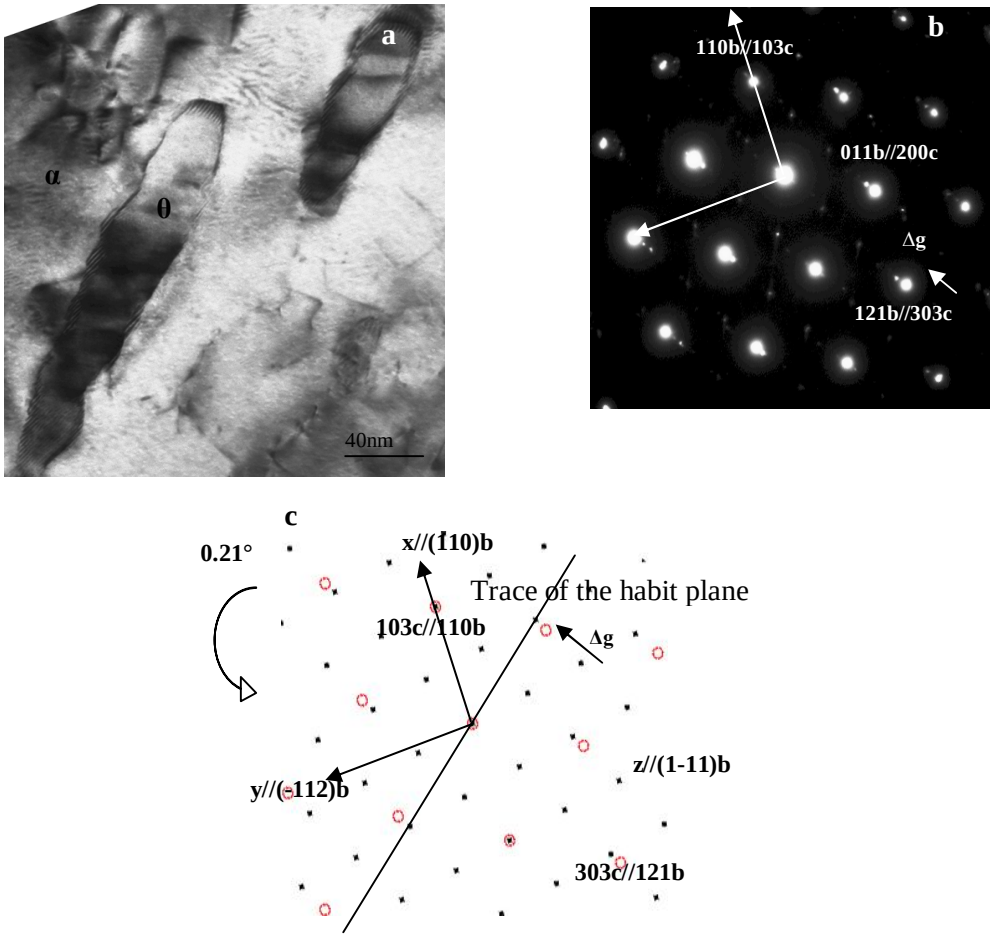

Figure- 3-1a- Cementite precipitate in [010]c//[1-11]b zone axis- 3-1b-The associated diffraction pattern. Streaking normal to stacking fault planes can be observed- 3-1c-The simulated diffraction pattern with an orthogonal coordinate system. 0.21°rotation around [010] c brings all Δ**g**s to parallelism. The trace of the habit plane is drawn and it is normal to Δ**g**. (ferrite spots are red and cementite spots are black).

Rotation was added to cementite crystal, because cementite is the reference lattice here. (Either of the two lattices can be the reference lattice) [5]

$$\mathbf{A}_r = \mathbf{G}_\alpha \mathbf{G}_\theta^{-1} \qquad \textit{Eq. 3-1}$$

$$\mathbf{A}_r = \mathbf{G}_\alpha (\mathbf{R} * \mathbf{G}_\theta)^{-1} \qquad \textit{Eq. 3-2}$$

The transformation strain in direct lattice, **A**, is then obtained as the inverse transpose of $\mathbf{A}_r$, so that abs (det (**T**)) approaches 0.Where **T** is the displacement matrix defined by eq.1-20. This condition guarantees the existence of an O-line structure. The O-line would be the eigenvector of **T**, associated with the eigenvalue closest to 1. The rotation should generally be done in three dimensions [26] or through trial and error with several pairs of low index axes and angles and then checked for consistency with the experimental diffraction patterns. Here it is assumed for simplicity that the rotation axis is [0 1 0]c//[1 -1 1]b[*****] . It will be shown later that this proves a successful assumption.

As figure 3-1c confirms, a small rotation of 0.21° from our starting condition, expressed in the form of parallel x, y and z axes, will bring all Δ**g**s to parallelism and would lead to abs(det(**T**))=0. A Δ**g** is a vector connecting the **g** reflections in the two lattices $\Delta\mathbf{g}=\mathbf{g}_\alpha - \mathbf{g}_\theta$. According to eq. 1-24 reproduced as follows, the O-lattice plane Δ**g**, also known as a Moiré plane (introduced in chapter 1, section 1-1-2), is associated with a plane **g** in the reference lattice (here cementite). [5]

$$\Delta\mathbf{g} = \mathbf{T}'\mathbf{g}_\theta \qquad \textit{Eq.1-24}$$

Low index Moiré planes are favored candidates for good-matching interfaces. [79] The predicted habit plane and invariant line are about 1° away from the rational planes (303)c//(121)b and [10-1]c//[-101]b directions. Table 3-1 summarizes the results of the above calculation.

[*****] This parallel pair was chosen because: 1- they are low index directions; 2- the misfit along this direction is very small.

The Burgers vector of a possible dislocation that accommodates the misfit in the interface plane normal to $\Delta\mathbf{g}$, lies in plane **g**. In our case, all $\Delta\mathbf{g}$s are parallel so the Burgers vector should be contained in all **g**s, in other words, it will lie along the zone axis of the diffraction pattern, [010] c// [1-11] b.

Therefore based on the O-line model (explained in section 2-2-1), we would expect the favored interface to contain one set of dislocations parallel with the O-lines accommodating the misfit in the habit plane in [010] c// [1-11] b direction.

The second important zone axis for investigating this interface, is [1 0 -1] c// [-1 0 1] b, 90° from the first zone axis as observed in figure 3-2 b that according to the previous results is close to the O-line direction. The diffraction pattern was taken from a precipitate in a different ferritic plate because of the tilt limits of the microscope. The interface in 3-2 a, where it is sharp and edge-on, is parallel to the expected habit plane again therefore it is consistent with our previous results. In addition to the habit plane, another facet of the precipitate can also be seen in an edge-on position. This observation can confirm that the direction of the electron beam is nearly parallel to an invariant line existing in several facets surrounding the precipitate as expected. [83]

Table 3-1- Calculated results compared with the experimental results.

Features:	Calculated results	Experimental results
Orientation Relationship	0.21°from Isaichev OR	Isaichev OR
Invariant line	$[1.2\ 0\ -1.2]_b/[-2.5\ 0\ 2.4]_c$	≈ [1 0 -1]b/[-1 0 1]c
Habit plane	$(1.1\ 2.3\ 1.1)_b/\ (3.7\ 0\ 3.6)_c$	≈ (1 2 1)b/(3 0 3)c
Dislocation spacing	9.24nm	2-5nm
Dislocation line	$[1.2\ 0\ -1.2]_b/[-2.5\ 0\ 2.4]_c$	≈ 10° from [10-1]b/ [-1 0 1]c

The matching between the simulated diffraction pattern and the experimental pattern in this zone axis, confirms our choice of rotation axis as an appropriate choice. Also, considering that the size of the precipitates in this zone axis only marginally differs from their size in [0 1 0] c, it can be concluded that each cementite lath has a low aspect ratio with the larger dimension close to [1 0 -1] c.

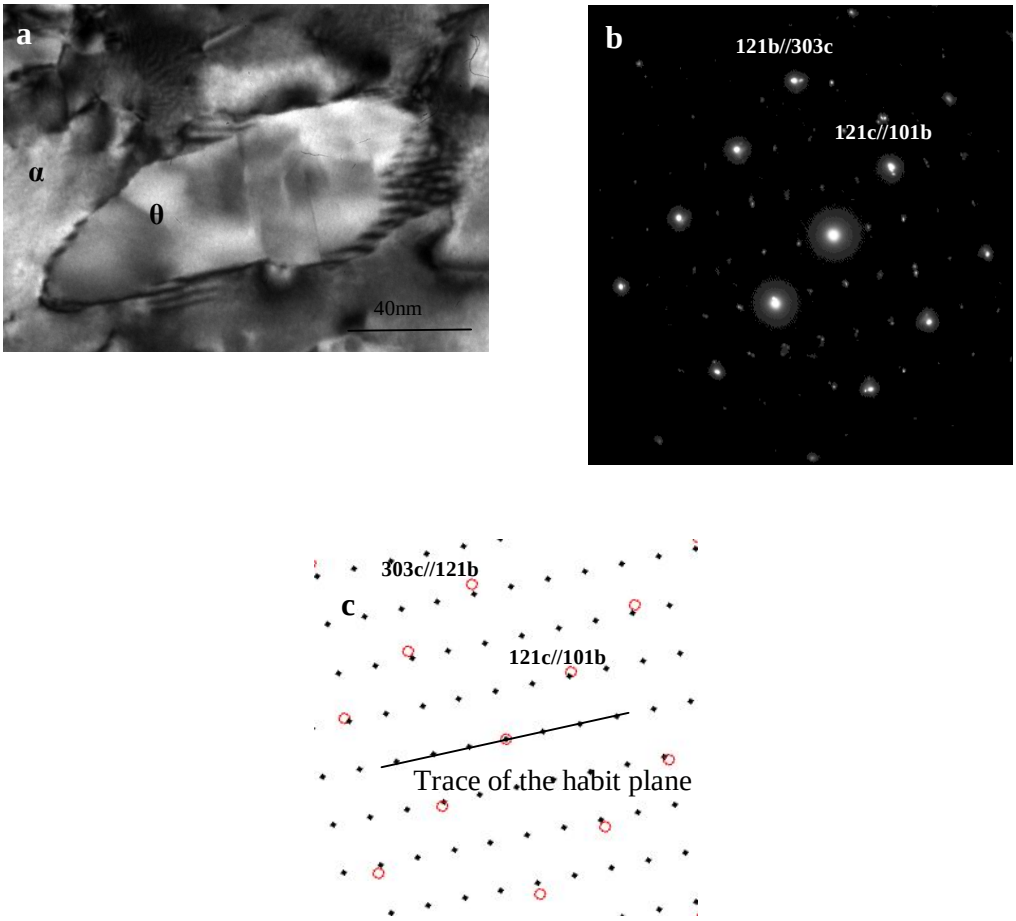

Figure- 3-2a- Cementite precipitate in [1 0 -1]c//[-1 0 1]b, 3-2 b- The associated diffraction pattern and 3-2 c- The simulated diffraction pattern. (ferrite spots are red and cementite spots are black) Care should be taken not to confuse the double diffracted spots with cementite spots.

An observation of a fringe structure was made on the interfaces of the cementite precipitates at two different zone axes. One of these zone axis images, is demonstrated in figure 3-4a, along with its diffraction pattern. Considering we expect dislocations along [-1 0 1]c//[1 0 -1]b to accommodate the misfit on the habit plane, our first guess is that they are interfacial dislocations. It can be seen from the stereogram of figure 3-5 that the direction of these linear features lies about 10° from [-1 0 1]c//[1 0 -1]b .Their spacing is about 2-5 nm taking into account the effect of projection. The very small size of the cementite precipitates coupled with the strong magnetic behavior of the TEM sample did not permit a full dislocation characterization of the interfaces. Therefore the predicted Burgers vector of misfit dislocations along [0 1 0]c//[1 -1 1]b cannot be experimentally verified. A lattice Burgers vector of 1/2[1 -1 1]b could be a good choice for ferrite but the equivalent cementite vector of 1/2[0 1 0]c is not a lattice translation vector. It will be shown in the next section (using the coincident site lattice/displacement shift lattice (CSL/DSC) construction) that 1/2[0 1 0] is a DSC vector in cementite. In other words even though it is not a lattice vector, it is a permitted dislocation Burgers vector. [7]

The dislocation spacing d_{dis} on a habit plane **n** can be calculated through eq.3-3 in which $\mathbf{Oc}^*$ signifies the reciprocal vector of the O-cell walls following [6] and can be calculated from eq.1-26.

$$d_{dis} = 1/\left|\mathbf{n}\times\mathbf{Oc}^*\right| \qquad \textit{Eq. 3-3}$$

$$\mathbf{Oc}^* = \mathbf{T}'\mathbf{b}^{L^*} \qquad \textit{Eq.1-26} \text{ (reproduced here from chapter 1)}$$

The calculated dislocation spacing is shown in table 3-1 to be 9.24nm.

The disparity between the observed experimental spacing and the calculated spacing of fringes on the interface can be the result of Moiré fringes that are parallel with interfacial dislocations, only with much lower spacings. If the interfacial dislocations had a smaller Burgers vector, a smaller spacing could be explained (using the equations above), but it will shown using the good matching sites (the NCS theory), that with the existing

transformation strain (A) , 9.24nm is the expected spacing of the good matching centers and consequently the spacing between the dislocation lines. (Because good matching sites and dislocations are alternating on the interface and have equal spacings)

To investigate the possibility of having mixed Moiré fringes and dislocations, a set of Moiré planes that is normal to these fringes was selected, as in figure 3-4b. The d spacing of these Moiré planes $\Delta\mathbf{g}$ (0 0 6)c (associated with cementite plane (0 0 6)), is about 1.47nms. Among the three sets of $\Delta\mathbf{g}$s, this one seems to be normal to the observed fringes. The d spacing of the two other $\Delta\mathbf{g}$s, $\Delta\mathbf{g}$ (-2 2 4)c and $\Delta\mathbf{g}$(-2 2 -2)c were also calculated and they are 0.93nm and 2.53nm respectively. It is therefore possible that these Moiré planes could obscure images due to dislocations, especially when the specimen is imaged in a zone axis.

Figure 3-6a depicts a high resolution image of the interface in the above zone axis. The sharp interface at this location is parallel to (1 2 1) b// (3 0 3) c that confirms our previous results. Figure 3-6 b shows the calculated image of [0 1 0] c/ [1 -1 1] b zone axis. From the calculated interface of 3c, projecting all the atoms of a cementite crystal, it can be seen that the dumbbells have not been resolved in the high resolution image of 3-5a. A similar observation was reported by Howe and Spanos. [81] Figure 3-7, contrary to the multilayer appearance of 3-6 b, is a detailed monolayer atomic model of the habit plane in the zone axis of [0 1 0] c// [1 -1 1] b. To accommodate the residual misfit in the direction of [1 0 -1] c// [-1 0 1] b and account for the 1° deviation from the terrace planes (1 0 1) c// (1 2 1) b; monatomic steps are required every 22nm. These widely spaced steps are not observed experimentally (figure 3-6 b).

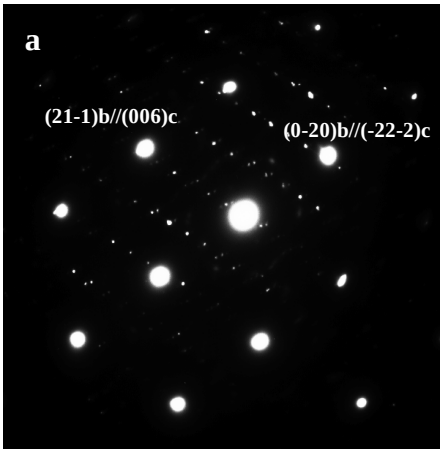

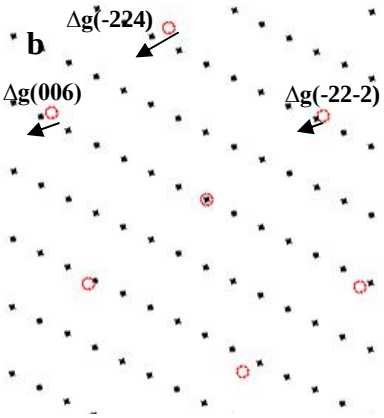

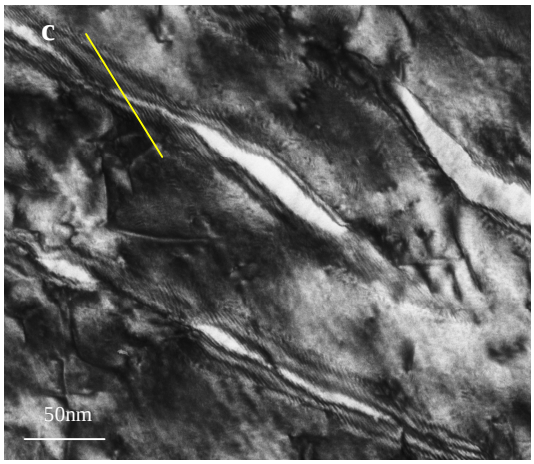

Figure 3-4a- Diffraction pattern at [1 0 2]b//[1 1 0]c zone axis along with 3-4b-Simulated diffraction pattern showing fringes that are possibly dislocations parallel with Moiré fringes on the interfaces of cementite precipitates at 3-4c the correlated image of the zone axis. (ferrite spots are red and cementite spots are black)

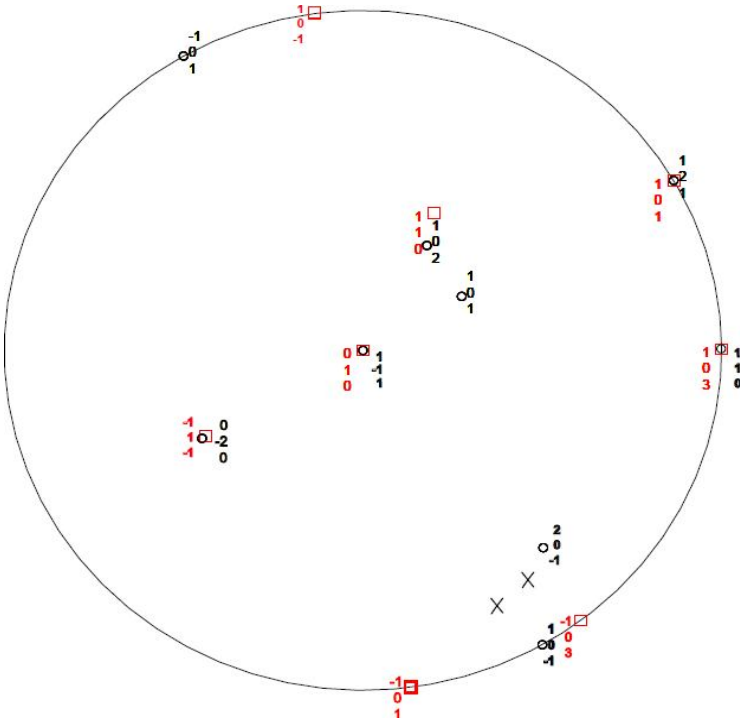

Figure 3-5- Overlapped stereograms of cementite (red) and ferrite (black) planes. Fringes of figure 3-4 were observed in the zone axes [101]b and [102]b. The two crosses indicate the direction of these fringes and are within 10° from [10-1]b//[-101]c.

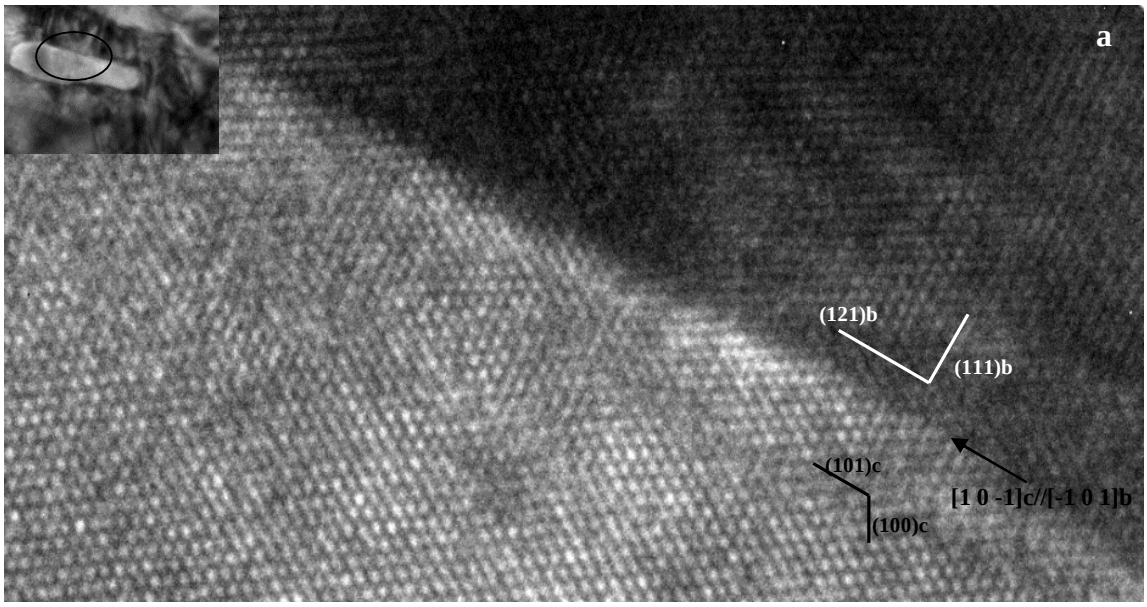

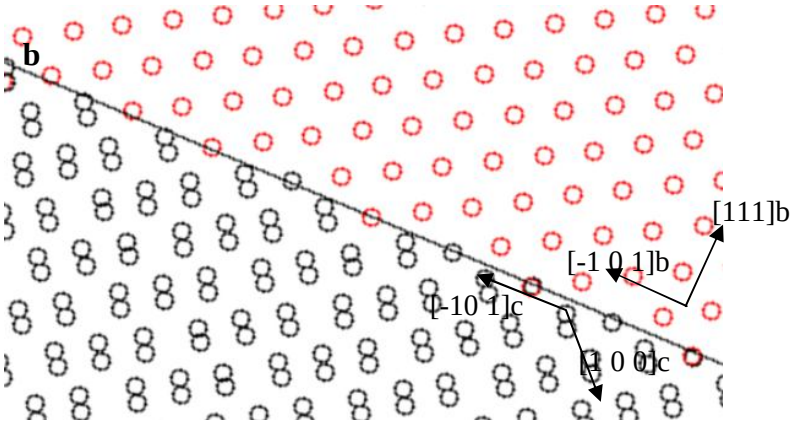

Figure 3-6 a- HRTEM image of a sharp section of cementite-ferrite interface. 3-6 b-The calculated interface, projecting all cementite atoms, matches the high resolution image but cementite dumbbells cannot be resolved and will be seen as one single atom in 3-6a.

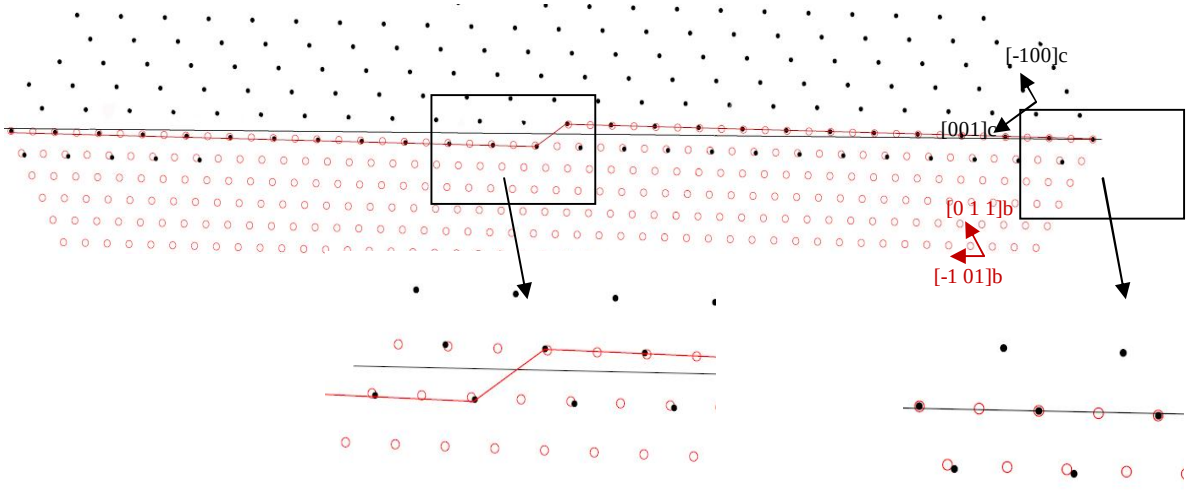

Figure 3-7- The black line is the trace of habit plane and the red line is its related terrace in the zone axis of [0 1 0]c//[1 -1 1]b. The magnified image of the step shows how the insertion of monatomic steps accommodates the small accumulated misfit in [1 0 -1]c//[-1 0 1]b.

3-1-2 CSL/DSC construction

The purpose of this section is to explain the nature of the dislocation Burgers vector of the previous section where misfit was seen to lie along [0 1 0] c//[1 -1 1] b . Even though ½[1 -1 1]b is a lattice vector in b.c.c. crystal, ½[0 1 0]c is not a lattice vector in cementite crystal, due to the large difference between cementite and ferrite lattice parameters. In Bollman's terminology, [7] in a secondary system where atoms of the two crystals do not have a one-to-one correspondence, a coincident site lattice/displacement shift lattice (CSL/DSC) construction would help to explain the dislocation Burgers vectors in the interface.

As described in chapter 1, the CSL is a lattice composed of perfectly matching lattice points of the two crystals and DSC is the lattice of translational vectors that leave the symmetry and the structure of CSL unchanged. To apply the CSL concept to heterophase

interfaces where the different lattice parameters of the two lattices do not permit perfect matching sites, lattice parameters of one phase can be constrained to form the CSL. Fe ye and Zhang [28] used this concept in their austenite/cementite investigation by constraining the cementite crystal to form the CSL. In this study, cementite was also constrained according to table 3-2 and figure 3-8 shows that in plane DSC lines, in other words the permitted dislocation Burgers vectors. It can be seen that a ½[0 1 0] c is a permitted DSC vector.

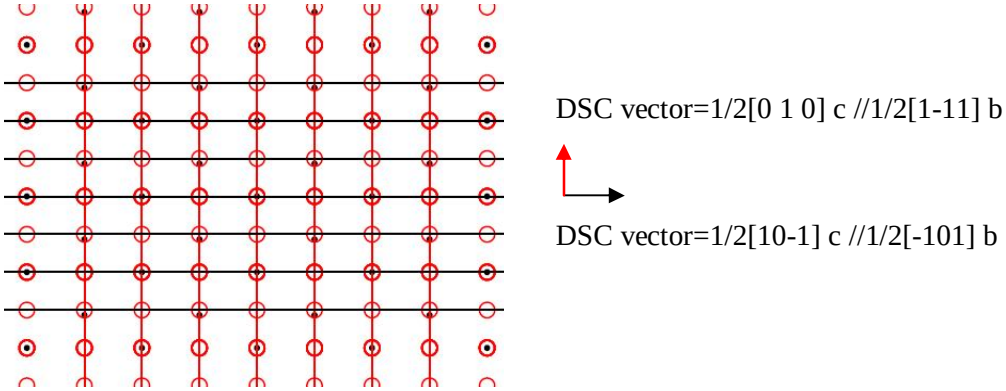

Figure 3-8- CSL/DSC construction on (1 0 1)c//(1 2 1)b. Translation of the atoms along the red and black DSC lines does not change the CSL matching structure.

Table 3-2- Lattice parameters of cementite before and after the constraint to construct a CSL lattice.

Cementite Lattice parameters:	a(nm)	b(nm)	c(nm)	A	β	γ
Cementite lattice parameters (Before constraint)	0.452	0.509	0.673	90	90	90
Cementite lattice parameters (After constraint)	0.4044	0.4953	0.7005	90	90	89.9

3-1-3 Near coincident site (NCS) model

As noted in chapter 2, in order to find favored interfaces other than the habit plane discussed previously, a 3-dimensional near-coincident site model was used. The calculated O-line orientation relationship of the previous section was used as an input in the NCS model. The details of the model are discussed in the introductory part of chapter 2 section 2-2-2 and further in appendix A. Figure 3-9 depicts the NCS in a convenient coordinate system that depicts the good matching pattern well, with three axes parallel to the invariant line, habit plane normal and their vector product. This coordinate system was used for the first time by Luo and Weatherly. [24]

As confirmed in other studies, the NCS forms periodic patterns. [35, 36] Traces of the 4 linearly correlated Moiré planes (possibly favored interfaces) were drawn to show that each intersecting point of these planes defines the center of an NCS cluster. These clusters (that are seen in 2 dimensions in this figure) are extended along the invariant line direction, which is normal to the page in figure 3-9. The favored interfaces are characterized to contain a high density of such clusters and are considered likely candidates for naturally occurring interfacial facets. [34-36]

The 4 Moiré planes have the following linear relationships (which will be evident from table 3-3):

$$\Delta\mathbf{g}_2 - \Delta\mathbf{g}_1 = \Delta\mathbf{g}_3 \qquad \textit{Eq. 3-5}$$

$$\Delta\mathbf{g}_2 + \Delta\mathbf{g}_3 = \Delta\mathbf{g}_4 \qquad \textit{Eq. 3-6}$$

Table 3-3, lists their associated **g** in both ferrite and cementite lattices in addition to the fraction of good matching sites on each of these possible interface planes. To calculate the good matching fraction, it was assumed that the thickness of each of these interface planes is about 0.3nm (close to the lattice parameter of ferrite). The NCS ratio was defined as the number of atoms of cementite that satisfy the criterion of matching to the

total number of cementite atoms in the plane. According to table 3-3, $\Delta\mathbf{g}_1$, the habit plane, is the best candidate for an interface.

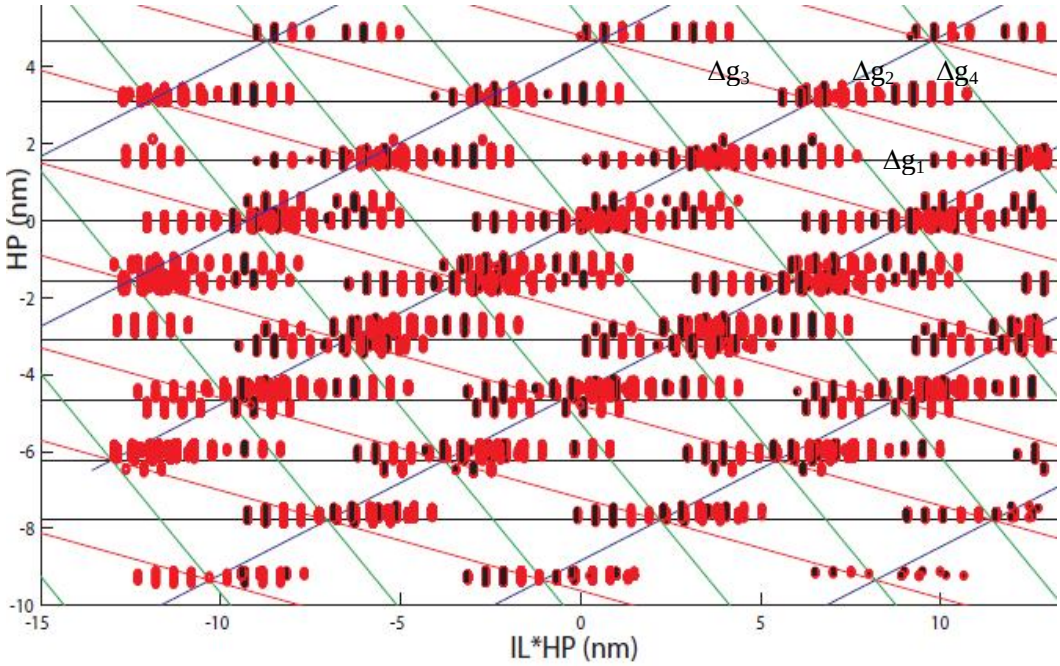

Figure 3-9 - The near coincident sites (NCS) in the zone axis of the invariant line. The intersection of all the Moiré planes defines the center of the NCS clusters. Red circles represent ferrite and black dots represent cementite. Due to high number of overlapped projected atoms, individual atoms cannot be distinguished.

Table3-3- A comparison between the Moiré planes of figure 3-9.

Possible Interfaces	Related **g**	NCS fraction	NCS spacing(nm)
Δg_1	(-1 0 3)c/(1 0 -1)b	0.54	9.24
Δg_2	(0 -2 2)c/(0 1-1)b	0.29	3.61
Δg_3	(1 -2 -1)c/(-1 1 0)b	0.22	6.19
Δg_4	(1 -4 1)c/(1 -2 1)b	0.08	2.07

Selection of possible equilibrium interfaces:

The habit plane

As discussed before, the ferrite/cementite broad interface is normal to all the parallel $\Delta\mathbf{g}$s such as $\Delta\mathbf{g}_{(2\,0\,0)}$, $\Delta\mathbf{g}_{(-1\,0\,3)}$and $\Delta\mathbf{g}_{(1\,0\,3)}$ in the zone axis of [1 -1 1] b// [0 1 0] c which can be seen in figure 3-1. (Cementite is the reference lattice.) Using an O-line model, the displacement (misfit) direction in the habit plane was found to be parallel to [1 -1 1]b//[0 1 0]c. It was also shown that the habit plane contains the highest fraction of matching sites among all candidates. Figure 3-10 shows the structure of the habit plane. The periodic fit/misfit pattern of good matching sites and dislocation lines between them is the typical O-Line structure of the broad faces. Misfit on this plane lies in the direction normal to the invariant line, [0 1 0] c// [1 -1 1] b and an edge dislocation with the Burgers vector of ½[1 -1 1] b//½[0 1 0] c can accommodate all the misfit strain on the plane. The spacing of dislocations is the same as NCS spacing on the plane which is 9.24nm.

The wide distribution of the good matching sites on this plane can be attributed to the fact that in addition to the invariant line, [0 1 0] c// [1 -1 1] b direction also has a very small misfit.

The edge facets

In an invariant line transformation, in contrast to the broad faces, the edge facets around a precipitate have been usually found to contain two sets of dislocations. [34-36] Among the Moiré planes in table 3-3, those labeled $\Delta\mathbf{g}_2$ and $\Delta\mathbf{g}_3$, can confine two Burgers vectors of the type <111>/2 or <100> in their associated planes of (0 1 -1) b and (-1 1 0) b respectively. A $\Delta\mathbf{g}_4$ plane associated with (1 -2 1)b can only contain one set of dislocations so we have focused our attention on $\Delta\mathbf{g}_2$ and $\Delta\mathbf{g}_3$.

The displacement in all interface planes, containing the invariant line, can be defined as follows:

$$\mathbf{d_u} = \mathbf{Tu} \qquad \textit{Eq. 3-7}$$

[3] , where **u** is a unit vector in the plane of $\Delta\mathbf{g}$ and perpendicular to the invariant line. **T** defines the displacement calculated using the transformation strain **A**:

$$\mathbf{T} = \mathbf{I} - \mathbf{A}^{-1} \qquad \textit{Eq. 1-20} \text{ (reproduced from chapter 1)}$$

In order to accommodate the misfit in $\Delta\mathbf{g}_2$ and $\Delta\mathbf{g}_3$ fully, the geometric relation between the dislocation Burgers vectors and their spacings can be described by:

$$\mathbf{d_u} = \sum_{i=1,2} \frac{1}{D_i}\mathbf{b}_i \qquad \textit{Eq. 3-9}$$

In which $\mathbf{b}_i$ and D_i are the Burgers vector and spacing of each dislocation set. Table 3, shows the possible dislocation Burgers vectors and their related spacing in $\Delta\mathbf{g}_2$ and $\Delta\mathbf{g}_3$. Type III in both of these candidates contains one set of dislocations with very large spacing and another set has a spacing similar to the NCS cluster spacing from table 1. The widely spaced dislocations are believed to be energetically more favorable. The occurrence of coarse/fine dislocation sets was also observed on the edge facets of Ti/Cr and Duplex stainless steel. [35, 36] In this work, the spacing of the coarse dislocations is about an order of magnitude larger than the reported cases in other alloy systems. In figure 3-11 a and b, the two possible candidates for edge facets are illustrated. The same fit/misfit pattern exists on these planes with a spacing similar to that of their good matching sites on the plane. The displacement vector $\mathbf{d_u}$ and Burgers vector of the related set of dislocations are shown. It can be seen in figure 3-11a, that a misfit dislocation with the Burgers vector of **b**=1/2[-1 1 1] b can almost completely accommodate the misfit on the plane. The residual strain can be accommodated with widely spaced dislocations with the Burgers vector of **b**= [1 0 0] b, inserted every 66.1 nm. Thus the second set would not be seen on the plane. The same argument applies to figure 3-11b. It can be seen from table 3-4 that type I of dislocation sets on both interfaces, contains 2 sets of closely spaced dislocations which may not be preferred energetically. In type II configuration, the spacing of the finer dislocations does not exactly match the NCS spacing from table 3-

3.Therefore type III, was chosen as the most likely candidate for the dislocation sets on both $\Delta\mathbf{g}_2$ and $\Delta\mathbf{g}_3$.

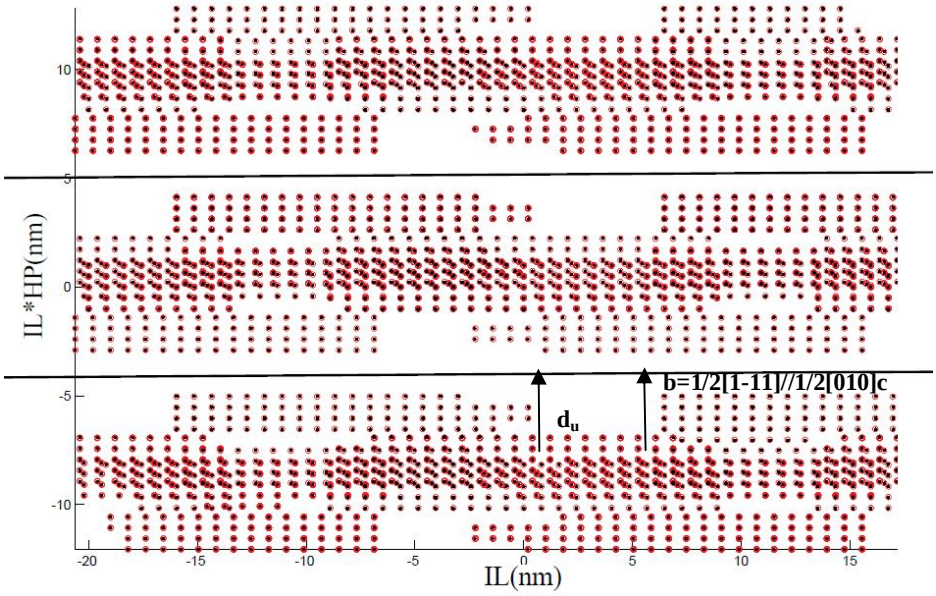

Figure 3-10- Alternating good matching sites (that are spread widely) and dislocation lines (black lines) on the habit plane. Misfit is fully accommodated by a perfect edge dislocation.

Table3-4- Candidates for the edge facets and their associated possible dislocation configurations

Possible side facets	Type	Possible Burgers vectors (b.c.c.)	Dislocation Spacing (nm)
$\Delta\mathbf{g}_2$	I	[1 1 1]/2-[1 0 0]	3.56-3.38
	II	[1 1 1]/2-[-1 1 1]/2	3.38-66.6
	III	[-1 1 1]/2-[1 0 0]	3.56-66.1
$\Delta\mathbf{g}_3$	I	[1 1 1]/2-[1 1 -1]/2	6.19-5.84
	II	[1 1 1] /2-[0 0 1]	90-5.82
	III	[1 1 -1]/2-[1 0 0]	91.57-6.22

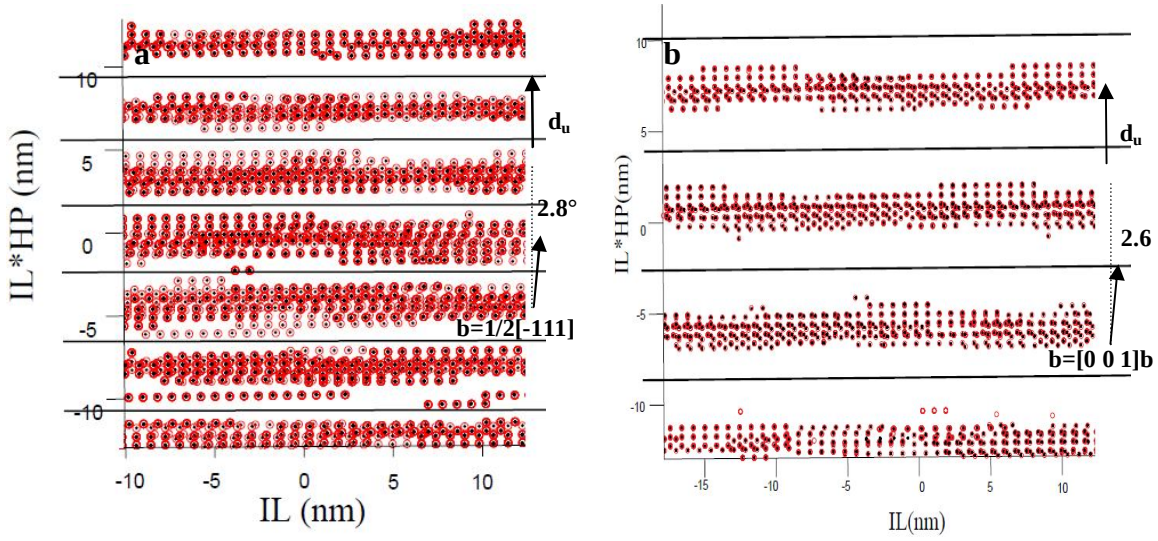

Figure 3-11a and 3-11b- Possible NCS (good matching sites) and dislocation configuration on $\Delta\mathbf{g}_2$ and $\Delta\mathbf{g}_3$ .Dislocation lines (black lines) on all the facets are parallel with the invariant line (the same fit/misfit pattern that was observed on the habit plane, is observed here). $\mathbf{d_u}$ will be accommodated by the displayed dislocations and a second widely spaced set that is not shown here.

Figure 3-12 a, is a conventional TEM image of a cementite precipitate in the zone axis of [1 0 -1] c// [-1 0 1] b close to the invariant line direction. The edge on side facet of the precipitate lies almost 15° from $\Delta\mathbf{g}_3$ and also $\Delta\mathbf{g}_4$. Therefore not only does it not coincide with the higher NCS density interface $\Delta\mathbf{g}_2$, but it is also deviated from the Moiré planes $\Delta\mathbf{g}_3$ and $\Delta\mathbf{g}_4$.The edge facet is close to a $\Delta\mathbf{g}_{3+}\Delta\mathbf{g}_4$ plane , that lies between $\Delta\mathbf{g}_3$ and $\Delta\mathbf{g}_4$, but this plane does not contain the dense NCS clusters. Our experimental study shows that, even though the orientation of the broad face seems to be consistent among different ferrite variants, multiple edge facets appear in different precipitates.

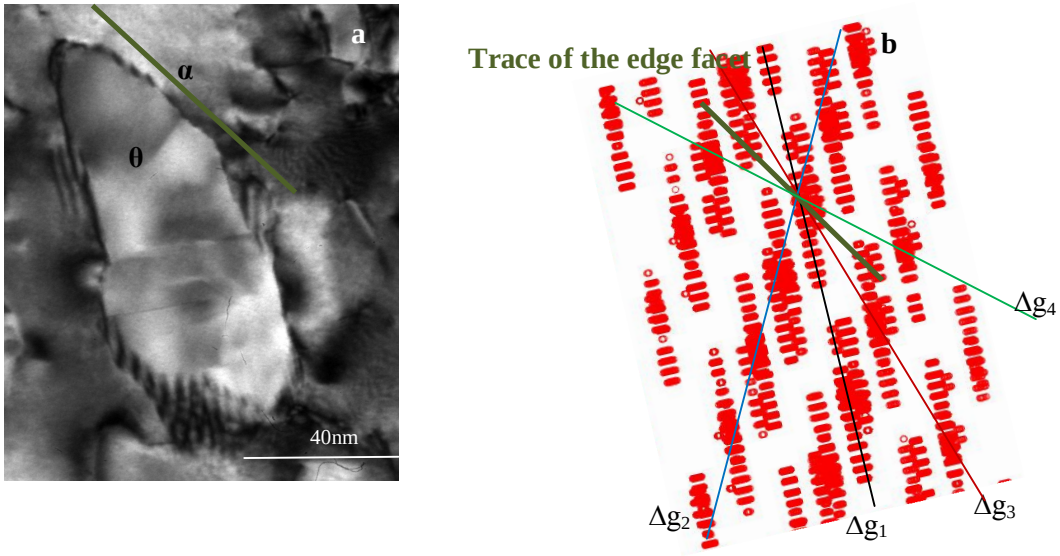

Figure 3-12 a- TEM micrograph of a cementite precipitate in [1 0 -1]c//[-1 0 1]b. b-The matching pattern in the zone axis of invariant line. The three interface candidates are displayed. The trace of the edge facet in a is about 15° away from $\Delta\mathbf{g}_3$ and 15° away from $\Delta\mathbf{g}_4$ in other words it would be parallel with a $\Delta\mathbf{g}_3+\Delta\mathbf{g}_4$ plane.

More precipitate images especially at the zone axis of [1 0 -1] c// [-1 0 1] b would be helpful in reaching a final conclusion concerning the observed deviation from the dense NCS planes. It can also be argued that at this stage of the transformation, (10 minutes in the bainite region at 350^{o}C) it is possible that the particle's surrounding facets are not necessarily in energy minimum configurations. The following summary includes more discussion on this observation. The calculated ferrite/cementite habit plane will be used in section 3-3; the interphase boundary nucleation of cementite.

Summary and discussion of section 3-1

Conventional and high resolution electron microscope observations of the OR between ferrite and cementite and the ferrite/cementite habit plane in the bainitic plate of sample A (containing bainite with cementite) were obtained. The observed orientation relationship

is a near-Isaichev OR, and it was shown that if this observed OR is rotated 0.21° about [0 1 0] c, a special case of an O-line OR in which all $\Delta\mathbf{g}$s in the diffraction pattern are parallel will be achieved. The calculated habit plane, orientation relationship and invariant line direction based on the O-line model are in agreement with the experimental results.

Linear features resembling interfacial dislocations were also observed with a spacing less than the expected dislocation spacing. Dislocation contrast (**g.b**) analysis could not be done to characterize interfacial dislocations experimentally because of the small size of the precipitates. Moiré fringes (with smaller spacings), parallel with interfacial dislocations could help explain this observed small spacing. According to the O-line model, the dislocation Burgers vector on the habit plane that accommodates the entire misfit was predicted using a CSL/ DSC lattice as 1/2[0 1 0]c//1/2[1 -1 1]b . Also it was shown that widely spaced structural ledges could accommodate the remaining misfit on the interface at [0 1 0] c//[1 -1 1] b.

The calculated precise OR was then used in an NCS model to determine all possible favored interfaces. The observed habit plane matches the most densely packed predicted interface from the NCS.

The possible low energy edge facets according to the NCS model are those designated $\Delta\mathbf{g}_2$, $\Delta\mathbf{g}_3$ (refer to figure 3-9 and table 3-4). Dislocation structures on these two potentially favored interfaces were investigated theoretically. The observed edge facet in an orientation close to the invariant line zone axis however, was deviated 15° from the $\Delta\mathbf{g}_3$ (refer to figure 3-12). In other word it lies parallel to a $\Delta\mathbf{g}_3+\Delta\mathbf{g}_4$ plane that does not contain a dense NCS structure.

It has been shown that such geometrically favored interfaces are likely to possess local energy minima when the interface energy is calculated using atomistic simulations. [84, 85] Therefore, assuming the calculated favored interfaces $\Delta\mathbf{g}_2$, $\Delta\mathbf{g}_3$ and $\Delta\mathbf{g}_4$ are correlated with local energy cusps, if they are not experimentally observed, one must question whether or not the transformation time and temperature were suitable for capturing

equilibrium interfaces. In other words, if the growth of cementite took place through both the end faces and the edge facets, and the particle in our study was captured in the middle stages of growth, the observed facet might be a non-equilibrium one, kinetically determined.

Even though there have been studies on the orientation relationship/habit plane between ferrite and cementite in bainite, [64, 65] their detailed interfacial structures have not been reported before. Also, cementite/ferrite interfaces other than the habit plane have not previously been discussed. Section 3-1 aimed at determining the dislocation and step structure of the habit plane and determining other possible edge facets. The geometrical modeling procedure, implicitly aiming at minimizing interfacial energy, was used systematically to discuss the possible interfaces of a cementite precipitate and their structures.

3-2 Austenite /Ferrite interface

3-2-1 Overall microstructure

Following chapter 2 section 2-2-3, in this section the experimental optical, SEM and conventional TEM results on steel B and C (containing cementite-free bainite) will be presented and discussed in an effort to shed more light both on the overall morphology of bainitic ferrite and the ferrite/austenite interfacial structure. In addition, the principles of martensite crystallography and an O-line model have been employed in a treatment of the crytsallography of the ferrite/austenite interface. The optical micrographs of figure 3-13 show the development of the bainitic ferrite microstructure in steel C with time. Each bainitic ferrite component seems to be composed of small laths or platelets, or in other words, of subunits. With increasing time the overall plate-like microstructure both lengthens and thickens, possibly through nucleation and growth of new units. Figure 3-14

is a more highly magnified SEM image of bainitic ferrite after 3 minutes of transformation. Plane AA′ cuts the microstructure in 3-14a at the displayed position. The FIB cross section is shown in 3-14 b. The appearance of the two outlined laths in the cross section suggests that smaller units on the surface have a long growth direction normal to the surface. In order to have a better understanding of what the microstructure looks like in 3 dimensions, a FIB serial sectioning experiment was done on a plate microstructure of bainite in steel C after 10 minutes of the transformation. Figure 3-15 a, b and c show how different cuts of 1 μm thickness can be put together[†††††] to outline the 3D microstructure of the bainitic ferrite. The rather weak contrast of the FIB images only allows the general outline of the microstructure to be displayed, as in 3-15 b, but it can be seen that the same complex microstructure on the surface persists deeply within the sample. Therefore it can be argued that a number of accumulated long units of bainitic ferrite have given rise to the 3D microstructure of figure 3-15 d. In Figure 3-15 c, the back view of the selected bainitic ferrite volume is shown to be composed of several overlapping plate-like layers, giving rise to a corrugated appearance. In short, the generated 3D volume shows that a 2D observation (outlined in 3-15b) can be misleading in anticipating the overall microstructure of bainitic ferrite.

It is also worth noting that the microstructure of figure 3-15 (formed after 10 min of the transformation) has apparently developed and thickened to a more complex aggregate than the microstructure after 3 minutes of the transformation.

Both optical and SEM images correspond to steel C, whereas all the TEM work of the next section has been done of steel B. The similarity of the microstructure between Mn and Ni steels, (C and B respectively) permits us to compare the results.

It will be shown in the next section that all the small units within one single volume correspond to the same crystallographic variant.

[†††††] Using AMIRA software.

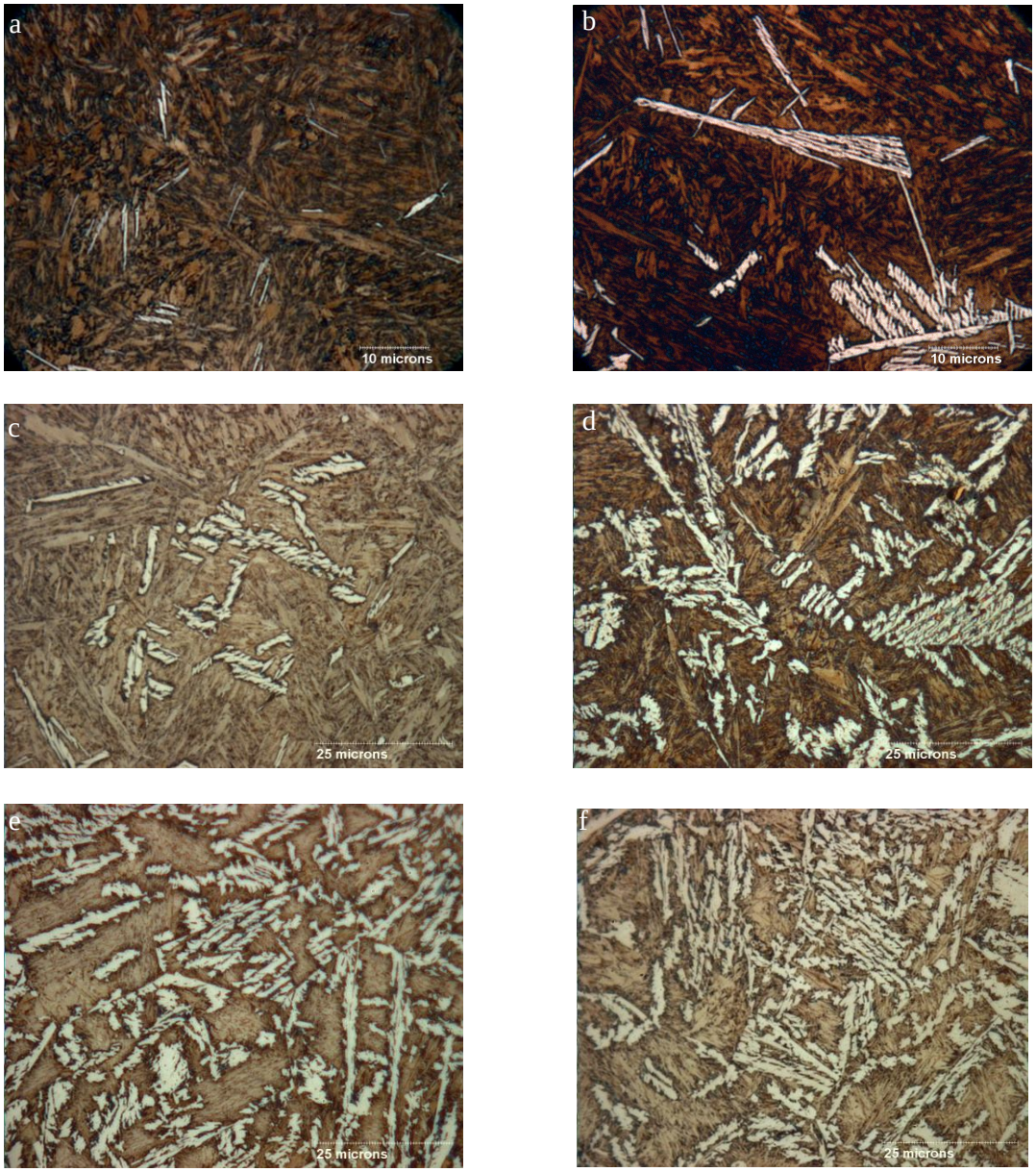

Figure 3-13- Development of bainitic ferrite in steel C (etched white) in a matrix of martensite (etched brown) with time at 350°c. a- After 3min, b- 6min, c- 10min, d- 20min, e- 40 min and f- 80 min. The plate microstructure is seen to be composed of smaller units.

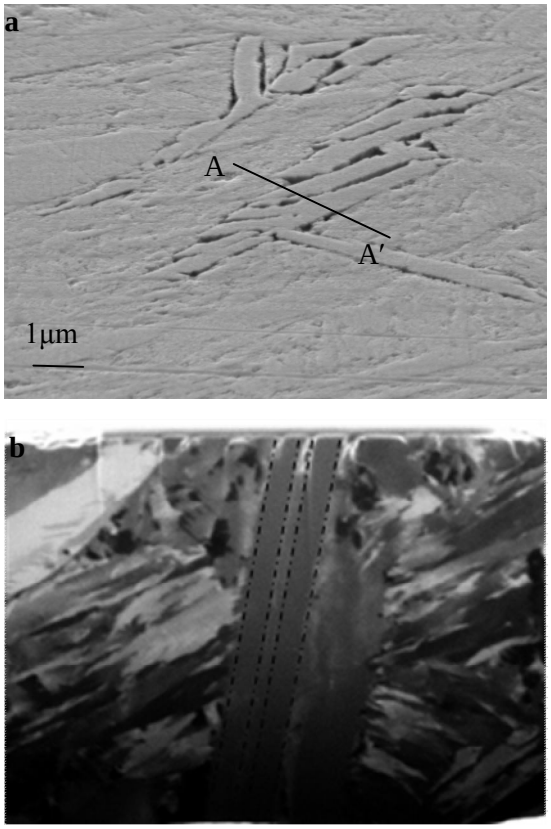

Figure 3-14- a- SEM image of bainitic ferrite in steel C formed after 3 minutes of transformation at 350°c shows several ferritic laths from one crystallographic variant and one perpendicular lath from a second variant .b- The laths on the surface have a longer direction (outlined in dashed black) at the cross section.

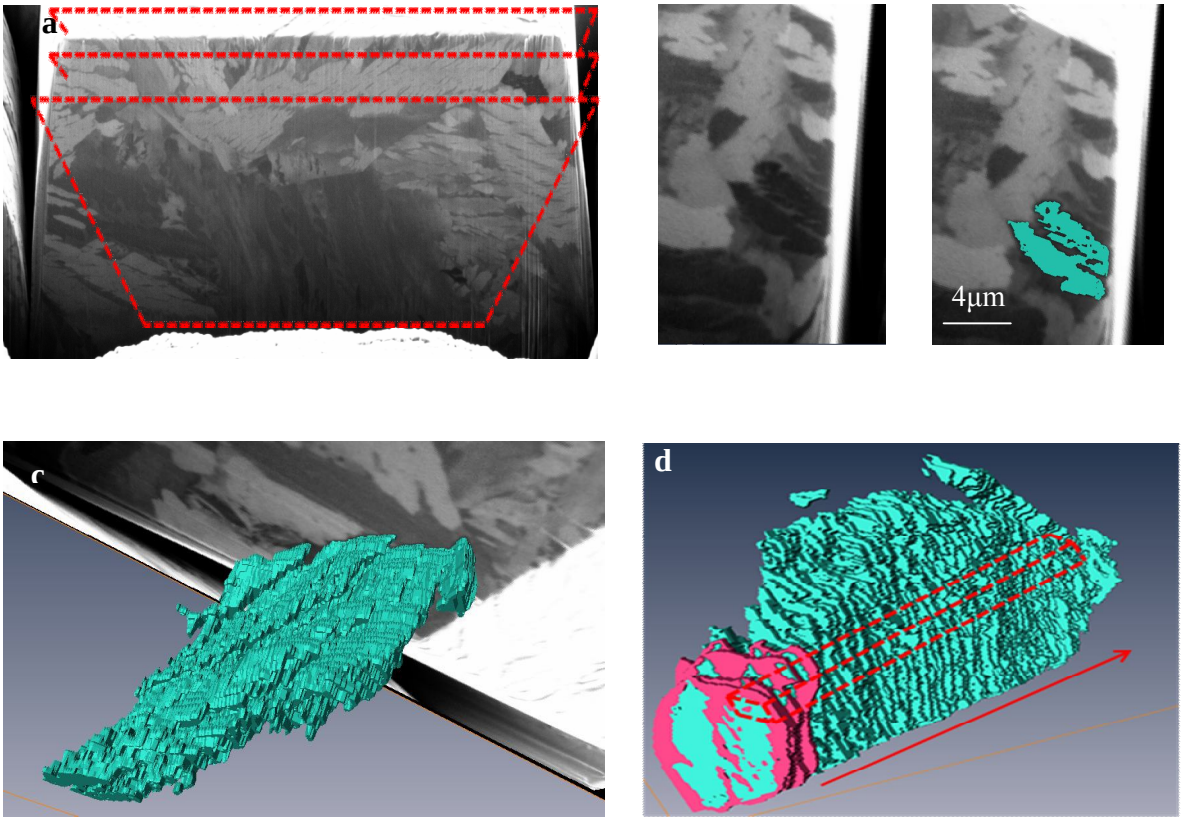

Figure 3-15-a The rectangles represent the serial sectioning procedure on a bainitic plate in a FIB contrast cross section. b- The selected plate will be marked in every section to form a 3D volume of the microstructure. c- A view from the back of the generated volume of the bainitic ferrite aggregate. d- The final volume of the bainitic ferrite is depicted in green (pink coloration was used to make the details stand out) It can be seen that the bainitic ferrite volume had a longer direction normal to the surface .

3-2-2 Conventional TEM results

The cross sections of different units of bainitic ferrite in a [1 1 1] b zone axis are shown in figure 3-16 a. The weak beam dark field image (WBDF) of 3-16 b, shows the dark field image of one of the {110} b.c.c. reflections. Separate interfacial fringes and small misorientations (signified by a the slight change of contrast) around each unit is an

indication that in addition to being separated from one another, the long axes of the bainitic ferrite laths do not lie in the plane of this section.

The long axes of ferrite laths have been assumed to be invariant lines in upper bainite. [86] To investigate that, the O-line model by Qiu and Zhang [82] was applied to the measured lattice parameters of ferrite and austenite of table 2-2. The results will be discussed in the next section. The observed laths in figure 3-16 seem to be surrounded by several facets. In order to characterize these facets along with the possible long axis of the laths, several tilting paths (including the unit triangle around the [1 1 1] b zone axis in stereogram of figure 3-20) were tested to find the orientation that is parallel to all facets, in other words the axis of the lath.

Figure 3-17 a and b show the orientation in which, facets of figure 3-17c are close to an edge on orientation. Two facets of these units are characterized using trace analysis [16] as (5 -3 3) f// (0 3 5) b and (1 -1 1) f// (0 1 1) b. The former is generally known as the habit plane and the latter is normal to the close packed planes of austenite and ferrite. The orientation of the beam, when these interfaces are close to edge on positions, is about 5° and 3° away from the [0 1 1] f and [1 0 0] b respectively. (Displayed in figure 3-20)

The orientation relationship between ferrite and austenite was seen to lie between KS and NW ORs. It was confirmed by investigating two other ferritic precipitates (in different locations) that this OR in most locations applies to the ferrite/austenite interfaces. Figure 3-18 a, b, c and d show the two SAD patterns taken at the two correlated directions on the close packed planes, [1 1 0] f//[1 -1 1] b and [0 1 1] f//[1 0 0] b, in other ferrite units. Their images confirm our previous results on facet orientations. One other facet is added to our previous results, (1 -1 3) f//(1 2 1) b. The stereogram of figure 3-20, summarizes the experimental results on the observed dislocation structure and observed facets.

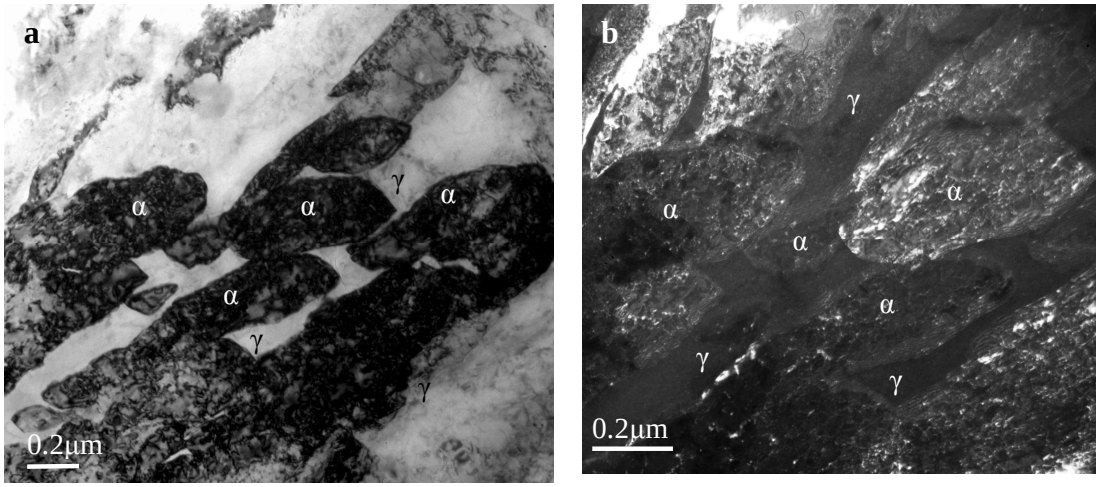

Figure 3-16a- Faceted units of bainitic ferrite in a matrix of austenite in steel B (heat treated at 350°c for 10mins).b-WBDF image of the same area of a <110> reflection close to the [1 1 1]b zone axis, showing the interfacial fringes around these units which implies that narrow layers of retained austenite exist between these units. The ferritic units seem to belong to the same variant of the orientation relationship.

The unit triangle in this figure shows the tilting path used to study the facets (to find the edge on interfaces) of figure 3-17.

The **g.b** invisibility criterion was used to characterize the dislocation structure of the facets. Three different reflections of (1 0 1) b, (-1 1 0) b and (0 -1 1) b were used. The first two gave rise to a fringe contrast and in the third one, these interfacial fringes disappeared. Figure 3-19a and b depict the dislocation contrast.

Projected line direction of dislocations, measured using trace analysis, was determined to lie within the ellipse (due to experimental uncertainty) on the stereogram of figure 3-20.

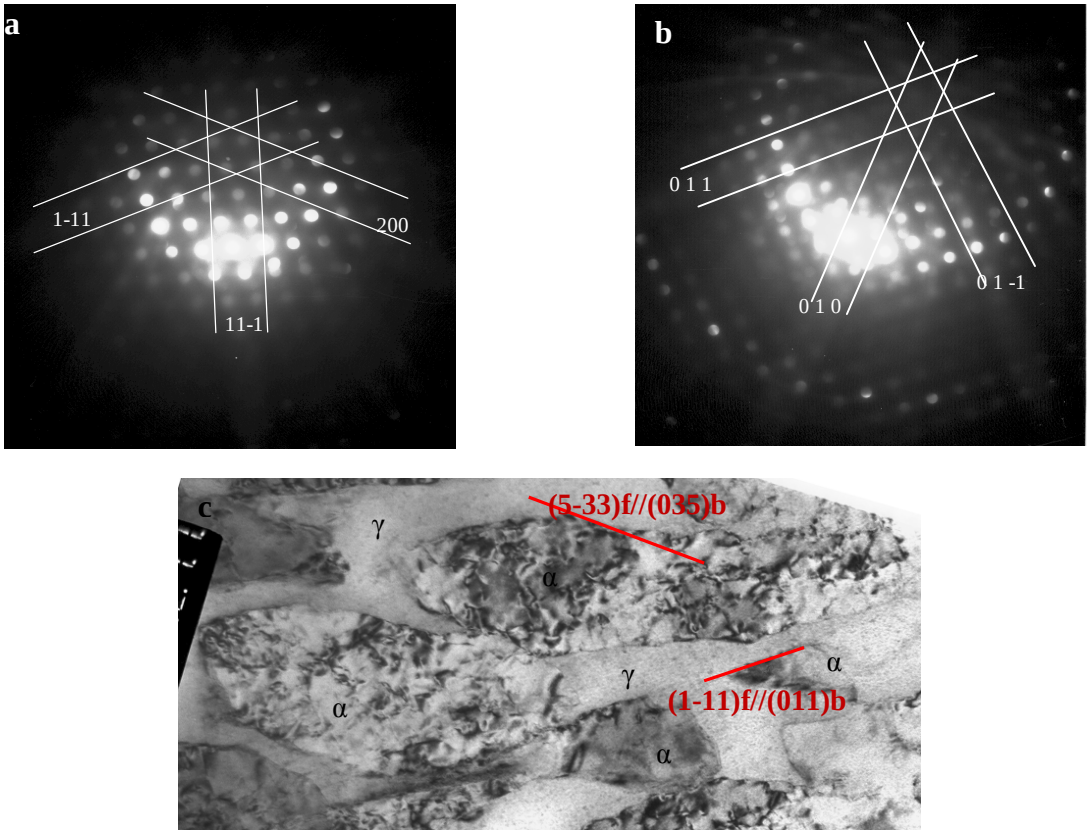

Figure 3-17 a- The orientation of the edge-on position of the facets of figure 3-16 in f.c.c. can be shown to be 3° from [0 1 1]f. b-The same orientation in b.c.c. is about 5°from [1 0 0]b. c- The almost edge on orientation of the facets of ferrite in a matrix of austenite.

Based on the invisibility criterion, there are two possibilities for the Burgers vector of these dislocations, [1 0 0] b and [-1 1 1] b. It can be seen that both of these directions lie almost 90° from the projected direction of the dislocation lines. Based solely on the observations made on the facets of figure 3-16, one can argue that these dislocations have an edge character. These results differ from Moritanti et al [3]'s report of screw dislocation pairs on the broad faces of bainitic ferrite. The transformation time in their study is of the order of a few seconds whereas, the isothermal bainite reaction in our samples lasted 10 minutes.

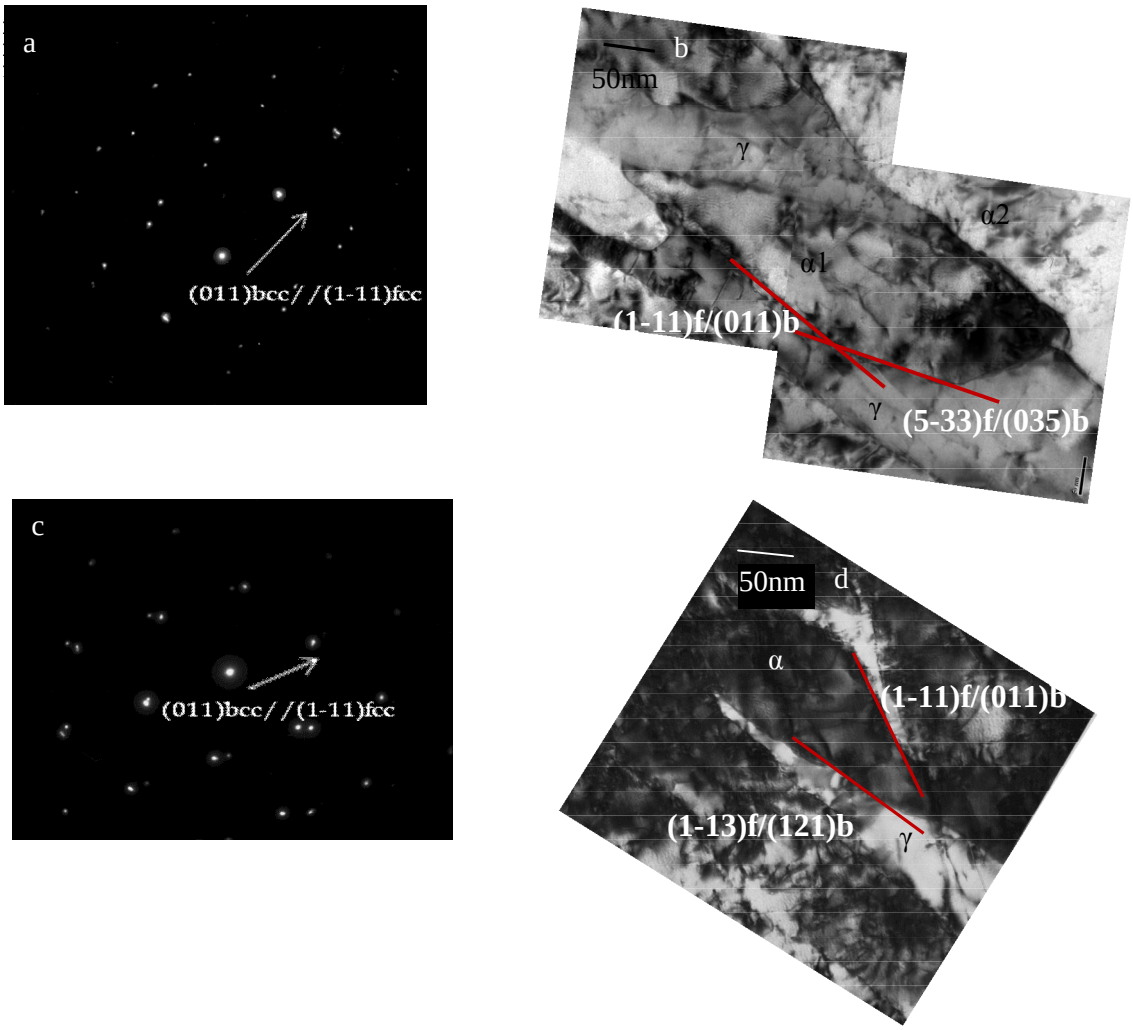

Figure 3-18 a- Zone axis of [1 00] b//[0 1 1]f. b- Its correlated image.c- Zone axis of [1-11]b//[110]f and d- Its correlated image. On both precipitates and their SAD diffraction patterns, the close packed planes of (1-11)f//(011)b are depicted. It can be seen that three different facets were characterized.

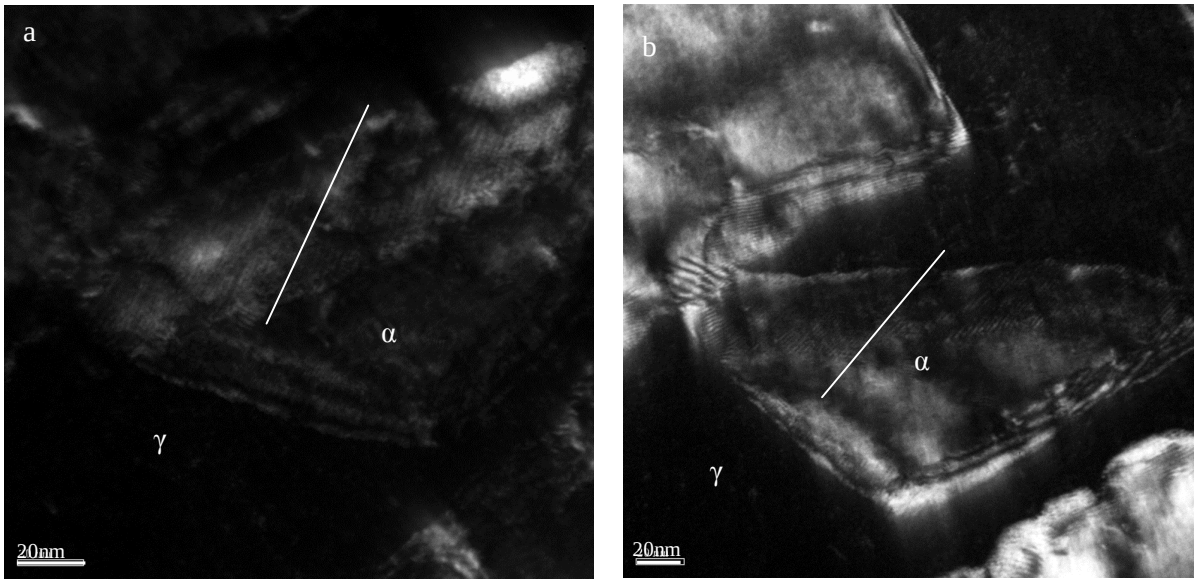

Figure 3-19a -Interfacial dislocations on facets of figure 3-16 imaged at reflections [-1 1 0] f and b- [-1 0 1] f.

It can be argued that the starting dislocations have a different role in the bainitic transformation and their behavior and character change after the progress of time.

Moritani et al. [3] also used this argument to explain the difference between their dislocation character and those of previously reported ones in the literature. In the next section, the possibility that the observed long axis of the observed faceted units will match an invariant line of an f.c.c./b.c.c. transformation will be considered.

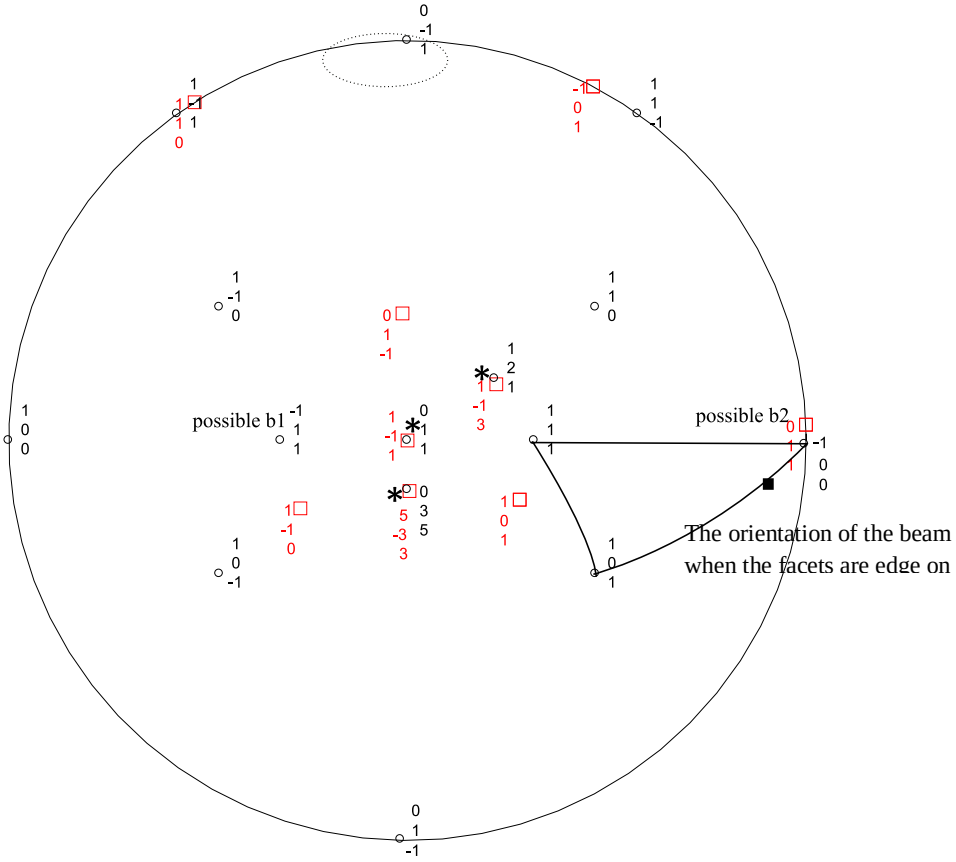

Figure 3-20- The overlapped stereogram showing the OR between ferrite and austenite, the ellipse outlines the projected dislocation direction, the stars represent the observed facets and the unit triangle is the path of investigation. Possible dislocation Burgers vectors are marked as b1 and b2. Black square shows the approximate orientation of the beam when the facets are close to an edge on orientation.

3-2-3 O-line Model

It was pointed out by Christian [10] that the invariant line for a martensitic transformation must lie in the cone of unextended lines. Therefore for a known Bain correspondence and a selected shear system, the invariant line in both direct and reciprocal lattice will be fixed. The shear does not always apply to non-martensitic transformations, therefore other criteria must be used to define the invariant line.

Qiu and Zhang [82] used the O-line criterion to limit the invariant line selection. This criterion implies that an optimum interface contains dislocations that are parallel to the O-lines and accommodate the remaining misfit at the interface. In addition to the O-line criterion more constraints need to be applied such as achieving the widest dislocation spacing on the interface. Details of their method will be discussed in appendix C.

In order to investigate whether the edge-on direction of the previous section lies close to an invariant line, the analytical method by Qiu and Zhang was used.

The first step is to find the invariant line in reciprocal lattice by solving the three linear equations below:

$$\mathbf{x}^{*\prime}_{\mathbf{i}} \cdot \mathbf{x}^{*}_{\mathbf{i}} = 1 \qquad \textit{Eq. 3-10}$$

$$\mathbf{x}^{*\prime}_{\mathbf{iB}} \cdot \mathbf{x}^{*}_{\mathbf{iB}} = 1 \qquad \textit{Eq. 3-11}$$

$$\mathbf{b}^{\mathbf{L}\prime} \cdot \mathbf{x}^{*}_{\mathbf{i}} = 0 \qquad \textit{Eq. 3-12}$$

Where $\mathbf{x}^{*}$ is the invariant normal (or invariant line in reciprocal lattice), i represents either of the crystal lattices, $\mathbf{x}^{*}_{\mathbf{B}}$ is the invariant line after the transformation by Bain strain and $\mathbf{b}^{\mathbf{L}}$ represents the chosen lattice Burgers vector for the O-lines. Equation 3-12 satisfies the O-line criterion. Its equivalent in martensite crystallography expresses that the invariant line must lie in the shear plane.

The stereogram of figure 3-21 shows the results of the calculation of $\mathbf{x}^*$. Initial and final cones of unextended lines in reciprocal lattice are drawn on a stereogram based on the Bain correspondence between f.c.c. and b.c.c. crystals. To draw the cones, the measured lattice parameters of table 2-2 were used. The two possible answers are given to equations above from two main categories of lattice Burgers vectors. The <1 0 0>//<1 1 0>/2 is designated as $\mathbf{b_1}$ and <1 1 1>/2//<1 1 0>/2 as $\mathbf{b_2}$. The solution of the above equations can be graphically determined as the intersection of the initial cone of unextended lines in reciprocal lattice (the blue line) with the great circle of the corresponding Burgers vectors.

Qiu and Zhang conclude in their investigation that the invariant line in the direct lattice, will have to lie within a radius of 15° around the $\mathbf{x}^*$(designated by dashed circles in figure 3-21) to satisfy the O-line condition as well as keeping the Bain correspondence intact. [82]

The two possible solutions, within the dashed circles in figure 3-21, lie far away from [1 0 0] b that is in the proximity of the observed direction of the lath in figure 3-17. Simply put, an O-line OR is not consistent with our observations. Due to the complexity of cementite-free bainite microstructure in our study, the observations were not conclusive on the long direction of the lath. Also, in order for the long axis to match an invariant line direction, the transformation time can play an important role. It is possible that the agreement between the axis of the laths and the invariant line direction exists at an earlier transformation time.

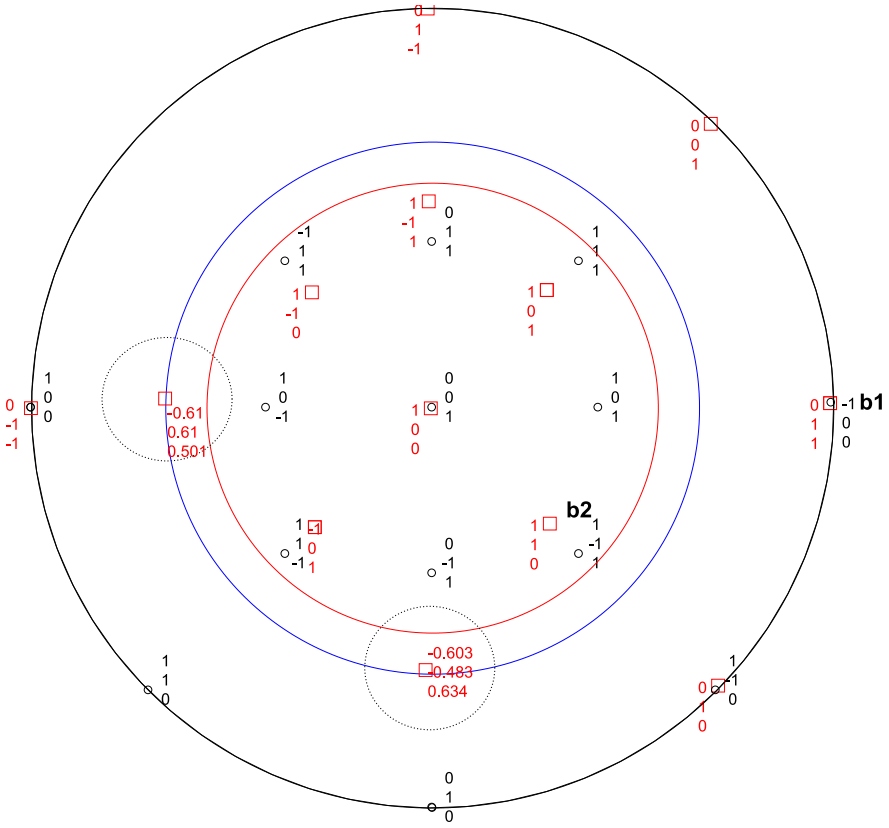

Figure 3-21- Overlapped stereogram at Bain OR between ferrite and austenite of the lattice parameters measaured in this study. Two possible solutions for the invariant line are represented by the 15° circles around the **x***s.

Summary and discussion of section 3-2

In this section, the results on overall microstructure of bainitic ferrite, ferrite/austenite interfaces and their dislocation content were displayed.

Based solely on our optical images, the slow development of carbide free bainite is in agreement with previous works on the kinetics of bainite [87] , the observations of a thermionic emission microscope study done at high temperatures in General Motors company in 1972 and a recent *in situ* synchrotron study. [88, 89]

It is very likely based on all the microscopic evidence in steel B, that at the temperature of interest in this study (350°), bainitic ferrite forms in units that share the same orientation. Similar observations have been reported in the literature. [2] Sympathetic nucleation [61] and/or autocatalysis [90] have been used to explain the appearance of ferritic bainite units. In order for the former to be valid, observations of ferrite/ferrite grain boundaries between subunits would be required but the latter is based on the concept that nucleation of new units separated from existing units, will be facilitated by the elastic interaction between the existing and nucleating units, so that small films of austenite would remain between ferritic bainite units. In this study, ferrite/ferrite grain boundaries have been occasionally observed, but in most cases, given that the transformation was at an advanced stage it would seem that the units had thickened, WBDF (weak beam dark field) images have shown narrow films of austenite in between the units implying that it is more likely that the consecutive formation of bainitic units is facilitated by autocatalysis.

From the above discussion it can be inferred that, a bainitic microstructure in steel B, could develop by a series of nucleation and growth events and in steel A, nucleation and growth of the bainitic units along with interphase boundary cementite precipitation can account for the overall kinetics. The assumption of a single plate growth that treats the entire bainite sheaf as a single entity cannot explain this complex microstructure. If this is

the case, a more physically meaningful kinetic model in bainite should include successive nucleation and growth stages of the smaller units within a sheaf.

On the other hand, on careful examination, the complex microstructure of bainite may have developed via branching of the initial interfaces. Even though crystallographic constraints can act as barriers to branching at the low temperatures of the bainitic transformation, the steep carbon gradient in the enriched austenite could favor branching or in other words, an anisotropically moderated morphological instability could develop as the transformation proceeds. A high resolution *in situ* microscopic study and/or further high-resolution microscopic studies on a series of heat treated samples at different times and temperatures are required to draw final conclusions on how morphological development occurs in bainite.

Based on the results of the FIB experiments, the microstructure composed of several faceted aggregates was seen to penetrate deeply in the sample in a direction perpendicular to their surface. It was also seen that several layers of bainitc plates were connected to each other.

Several facets were observed to surround bainitic units and the dislocations on the interface ((5 -3 3) f//(0 3 5) b interface) were characterized as edge dislocations. The previously observed dislocation sets in bainite showed a screw character and this disparity was rationalized by taking the transformation time into account. In other words, it is possible that the interfacial structure of the habit plane changes with transformation time. [3]

The experimental results on ferrite/austenite were displayed in the stereogram of figure 3-20. It was observed that the surrounding facets of bainite will be edge-on in an orientation near [1 0 0]b//[0 1 1]f. An O-line model using the measured lattice parameters of ferrite and austenite did not confirm this orientation as an invariant line. It was discussed that the agreement between the axis of the laths and the invariant line direction might have existed at an earlier transformation time. Overall, it appears that the crystallography of the

bainitic ferrite, including its lath axis orientation, interface orientation and dislocation character may change appreciably with transformation time.

3-3 Interphase boundary nucleation

As explained in chapter 2, section 2-2-4, the crystallography of cementite in bainite resembles that in tempered martensite and for this reason they will be compared in this section. The crystallography and morphology of cementite in bainite were described in section 3-1. Cementite in tempered martensite is known to have a similar morphology and to follow Isaichev and/or Bagaryatskii orientation relationships summarized below:

[0 1 0]c//[1 -1 1]b

(1 0 3)c//(1 1 0)b Isaichev or (2 0 0)c//(0 1 1)b Bagaryatski

These two orientation relationships are only 3 degrees deviated about [0 1 0]c//[1 -1 1]b axis, and are sometimes very hard to distinguish experimentally. In section 3-1, cementite was shown to share an Isaichev OR with its matrix in bainite.

The main difference between the precipitation crystallography of cementite in bainite and tempered martensite is the number of cementite variants of the above orientation relationships that appear in the ferritic matrix. In tempered martensite, multiple variants of cementite have been observed and reported whereas in bainite mainly one variant of the OR is observed. [1]

Ideally all the equivalent crystallographic variants of a second phase will be present within the matrix when precipitation occurs in a supersaturated matrix unless an external stress or the transformation strain would encourage selective variants. In the literature of bainitic transformation, one of the main reasons accounting for the univariant appearance of cementite in bainite, is the idea of interphase boundary nucleation of cementite. [86] Crystallographic reasoning for the interphase precipitation will be discussed in section 3-3-1 under the title of tempered martensite vs. bainite. The next section, 3-3-2 will deal with the nucleation of cementite on ferrite/austenite interfaces from a thermodynamic/kinetic point of view.

3-3-1 Three phase crystallography:Tempered martensite vs. bainite

Figure 3-22a shows a tempered martensite structure in steel D. The DF images of at least two variants can be detected. The fine multivariant microstructure is the typical tempered martensite microstructure observed in steel D. Figure 3-23 on the other hand is a typical image of univariant cementite in bainite. One major variant of Isaichev OR is observed inside each bainitic ferrite plate and another variant trails the ferrite/ferrite boundaries.

Figure 3-24 compares the <1 1 1>b//<0 1 0>c experimental diffraction pattern in bainite a, and tempered martenite, b to the simulated diffraction pattern satisfying the O-line strain. It appears that ferrite/cementite relationship in tempered martensite is slightly deviated from Isaichev OR towards Bagaryatski OR.

All possible variants of an Isaichev OR are depicted on a standard stereogram centered on [0 0 1] ferrite grain in figure 3-25. Table 3-5 demonstrates the relationship between all 24 variants relative to variant number 1. To calculate all these variants 24 symmetry matrices of the cubic matrix were multiplied by one variant of Isaichev OR as described in eq. 1-27. These 24 variants are composed of 4 sets of equivalent parallel directions <1 1 1>b//<0 1 0>c each consisting of 6 sets of parallel planes that are produced by rotation around each <1 1 1>b//<0 1 0>c. These 4 parallel directions are depicted by black squares in figure 3-25. The misorientation angles between variant number one and the other 5 variants in each pack of parallel directions are 30°, 30°, 37.2°, 22.8° and 7.2°.

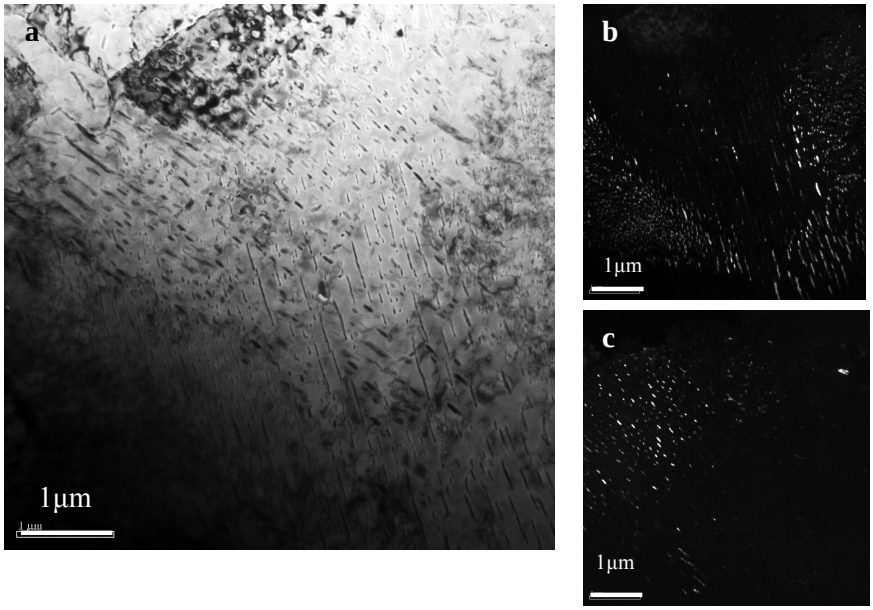

Figure 3-22a- A typical bright field microstructure of tempered martensite. b and c are the dark field images of two strongly diffracting variants.

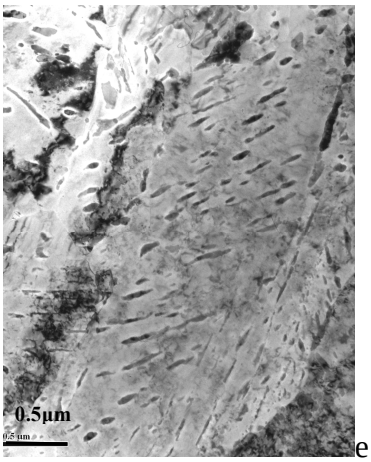

e

Figure 3-23, A typical bainitic microstructure. Cementite follows only one variant of the OR inside each ferritic plate.

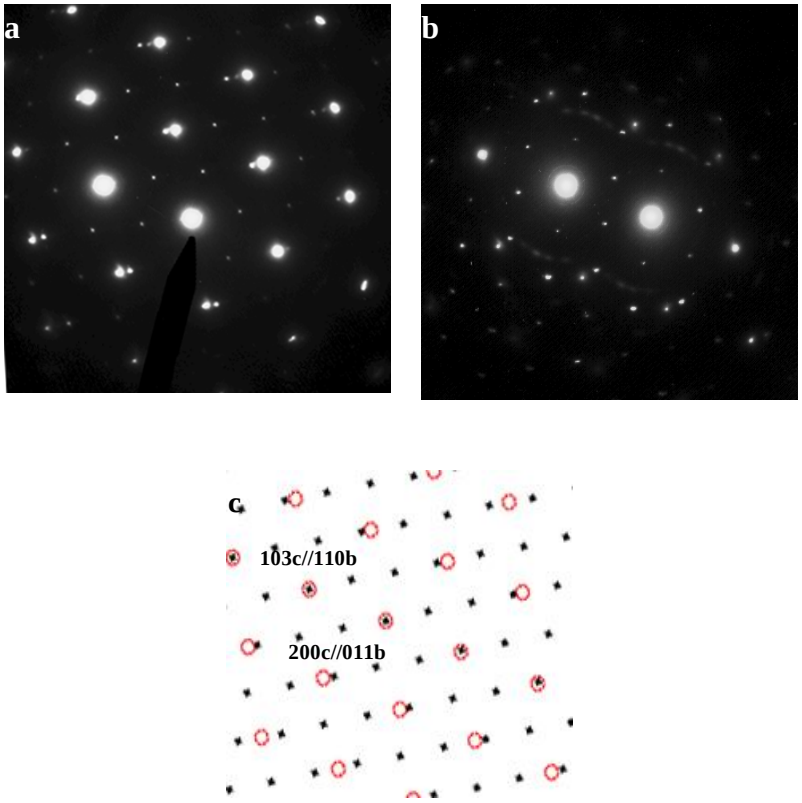

Figure 3-24a- Diffraction patterns in <111>b//<0 1 0>c zone axis in a- bainite and b- tempered martensite compared to the simulated Isaichev OR in c.

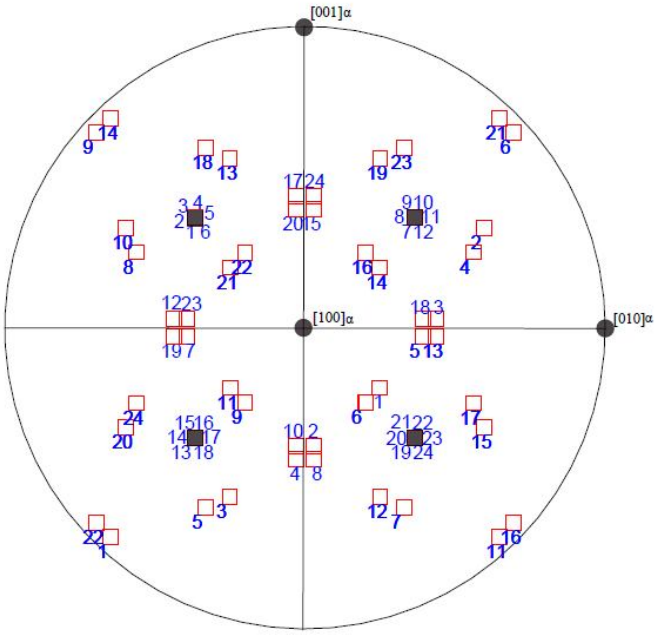

Figure 3-25- Projected <1 0 0>c orientations of 24 variants of an Isaichev OR on a [1 0 0]/(0 1 0) b.c.c. matrix. Each black square is a rotation direction of the type <1 1 1>b//<0 1 0>c.

Table 3-5- The relationship between all 24 Isaichev variants with respect to variant number one.

Variant	**Parallel directions**	**Parallel planes**	**Rotation from V1**	
No.	[θ]//[α]	(θ)//(α)	Axis([θ])	Angle(deg.)
V1	[010]//[1-11]	(103)//(110)	-	0
V2		(103)//(011)	[010]	30
V3		(103)//(10-1)	[010]	30
V4		(-103)//(110)	[010]	37.2
V5		(-103)//(011)	[010]	22.8
V6		(-103)//(10-1)	[010]	7.2
V7	[010]//[111]	(103)//(0-11)	[-0.56 0.56 -0.59]	46.91
V8		(103)//(-110)	[0.058 0.85 -0.52]	38.32
V9		(103)//(-101)	[0.62 0.74 -0.22]	49.69
V10		(-103)//(0-11)	[0.23 0.86 -0.45]	39.38
V11		(-103)//(-110)	[0.69 0.69 -0.16]	54.47
V12		(-103)//(-101)	[-0.45 0.65 -0.6]	43.2
V13	[010]//[-111]	(103)//(101)	[0.03 -0.78 0.61]	32.39
V14		(103)//(110)	[0.67 -0.67 0.28]	44.54
V15		(103)//(0-11)	[-0.65 -0.45 0.60]	43.2
V16		(-103)//(101)	[0.74 -0.62 0.22]	49.69
V17		(-103)//(110)	[-0.54 -0.54 0.63]	38.86
V18		(-103)//(0-11)	[0.23 -0.80 0.54]	33.37
V19	[010]//[11-1]	(103)//(101)	[-0.45 0.23 0.86]	39.38
V20		(103)//(011)	[-0.61 -0.03 0.78]	32.39
V21		(103)//(-110)	[-0.95 0.2 -0.2]	20.23
V22		(-103)//(101)	[-0.97 0.15 0.15]	20.01
V23		(-103)//(011)	[-0.54 0.23 -0.80]	33.37
V24		(103)//(-110)	[-0.52 -0.05 0.85]	38.32

This would mean that if a tempered martensite grain (cementite in a ferritic matrix inside an original grain of austenite) was investigated at a <1 1 1>b//<0 1 0>c zone axis, the observed cementite precipitates would be expected to show the above misorientations. The observations in this study confirm the literature reports that some variants dominate over others as can be seen in figure 3-22 in tempered martensite. Considering the parallel directions of figure 3-22 is of the type <1 1 1>b//<0 1 0>c, it is possible that only the 6 variants that have the parallel direction in common, appear in tempered martensite. In an

analogy to the observed variants in each packet of martensite that are the ones that share the close packed planes in a KS OR. [44, 91]

From the 24 variants of the Isaichev OR described above, usually only one will be observed in bainite as seen in figure 3-23. A three phase crystallographic relation between ferrite, austenite and cementite at the nucleation stage could account for this unique orientation. Kelly and Shackelton [71] were the first to point out that, if a particular variant of KS is obeyed by ferrite/austenite interface and a particular variant of Pitsch OR is obeyed by austentite/cementite, the resulting cementite/ferrite OR will be an Isaichev (or Bagaryatski) OR.

This three phase correlation also referred to as three phase crystallography in this text, has always been limited to the related ORs between the three phases as explained above. In this study we will demonstrate that the crystallographic relationship between the three phases, can also extend to their favored interfaces: ferrite/austenite, ferrite/cementite and austenite/cementite interfaces. Ferrite/cementite near Isaichev O-line OR[‡‡‡‡] and habit plane were discussed in section 3-1. The structure of the habit plane was shown in figure 3-7.

The Pitsch OR in austenite/Widmanstaetten cementite has also been investigated using an O-line OR by Ye et al. [28] and the results have been reproduced here. The variant of the Pitsch OR used in this investigation is shown in the simulated diffraction pattern of [1 1 0]f//[0 1 0]c in figure 3-26a. (The lattice parameters of table 2-3 were used for ferrite, austenite and cementite and the indices have been used consistently throughout this text) The correlated interface (habit plane) in this zone axis is shown in 3-26b.

Figure 3-27 shows the three phase orientation relationship when b.c.c./cem and f.c.c./cem both follow an O-line relationship which in both cases has been confirmed with experimental results. Their calculated habit planes have been shown to be 1°away from (1 2 1)b/(3 0 3)c and ≈6° away from (1 -1 3)f/(3 0 3)c respectively. [80] The resulting

[‡‡‡‡] When we refer to an O-line OR in this text, an orientation relationship that satisfies the O-line condition of chapter 3, is implied.

f.c.c./b.c.c. OR in figure 3-6 will be of a KS type that also follows an O-line OR with the habit plane of (1 2 1)b//(1 -1 3)f . In other words, this f.c.c./b.c.c. habit plane will be the terrace plane for both f.c.c./cem and b.c.c./cem. Clearly to maintain this relationship between the three phases, the lattice parameters of table 2-3 need to be imposed. Further on in this investigation it is assumed that at the moment of nucleation of cementite, this set of lattice parameters and consequently three phase relationships exist between the phases. Figure 3-27 b shows how the traces of interface planes of b.c.c./cem and f.c.c./cem lie about 5° apart. Table 3-6 compares the interfacial details of f.c.c./cem and b.c.c./cem habit planes.

There is no universal agreement as to whether cementite in bainite would match both ferrite and austenite crystallographically. In fact Bhadeshia [75] in 1980 published a paper on a bainitic steel containing the three phases (austenite/ferrite/cementite) in which he maintained that austenite and cementite have no tendency to lattice match. No other study has been reported on the correlation between the present three phases in a single bainitic microstructure. Because of the limiting fact that with the addition of Si to the steel, precipitation of cementite will be suppressed and without Si, retaining austenite to room temperature is not possible, the observation of the coexistence of the three phases, ferrite, austenite and cementite in a bainitic microstructure proves to be challenging.

Table 3-6- Comparing the structure of ferrite/cementite and austenite/cementite interfaces

Structural features	Ferrite/Cementite	Austenite/Cementite
Habit plane	1° away from (1 2 1)b/(3 0 3)c	≈6° away from (1 -1 3)f/(303)c
Step spacing	22 nm	5.8nm
Dislocation Burgers vector of the steps	_	[0 0 1/3]c
Dislocation Burgers vector on the habit plane	1/2[0 1 0]c	_

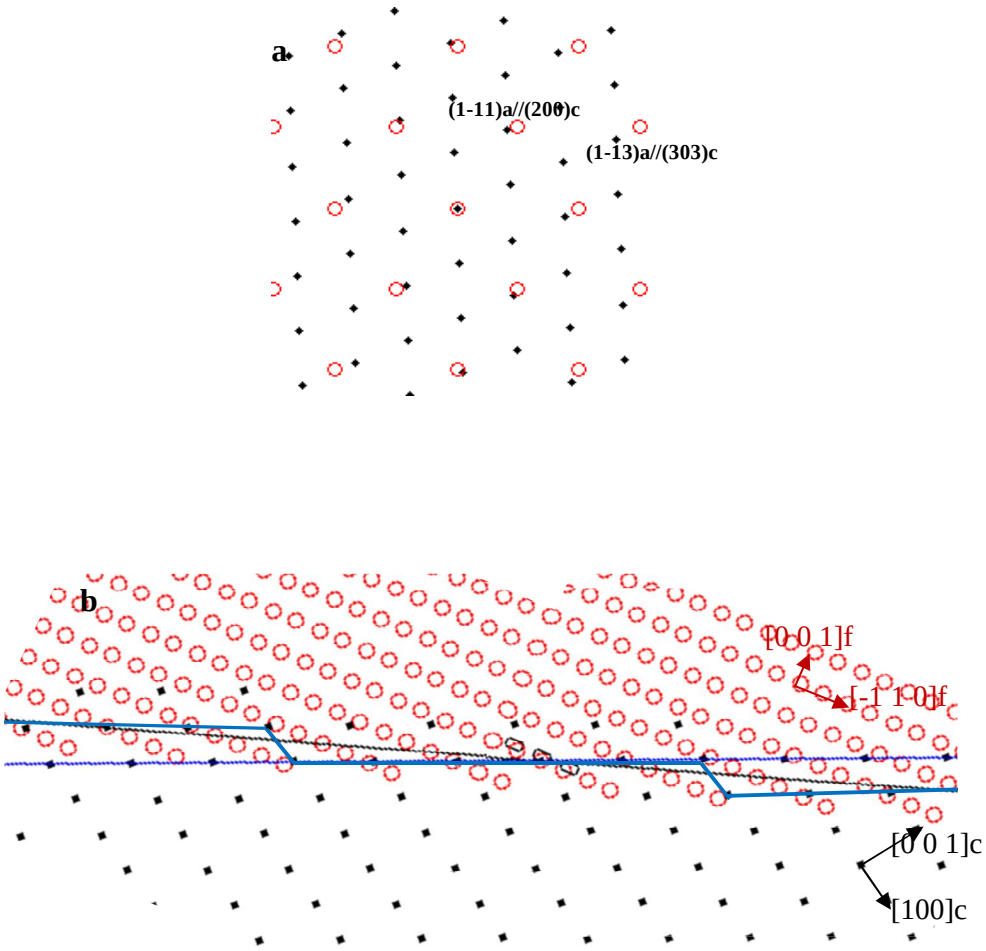

Figure 3-26 a- Simulated diffraction pattern of the Pitsch OR at [1 1 0]a//[0 1 0]c. Black represents cementite and red represents austenite. b-The interface between austenite and cementite .habit plane trace is the black line the blue lines show the terrace plane and the step direction on the interface.

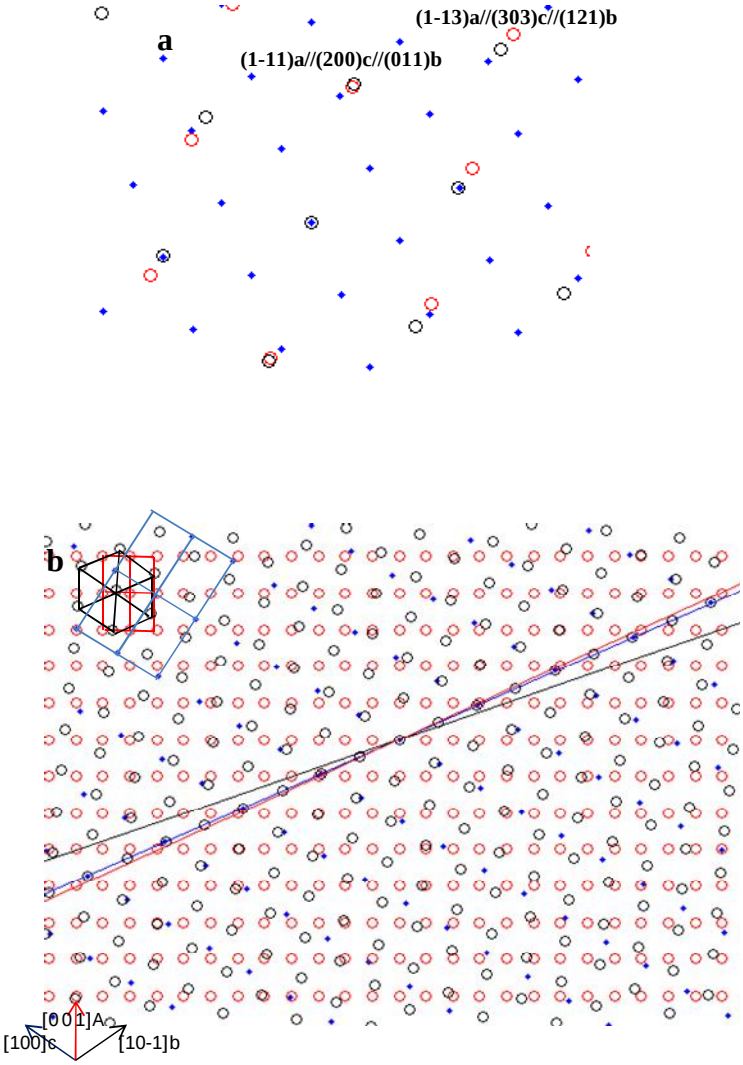

Figure 3-27a- Three phase OR between ferrite/austenite/cementite when ferrite/cementite and ferrite/austenite satisfy O-line ORs of Isaichev and Pitsch. The zone axis is parallel to [1 1 0]a//[1 -1 1]f//[0 1 0]c. The resulting ferrite/austenite OR is a variant of KS, b- The overlapped image of the three phases in the same zone axis. Traces of austenite/cementite interface plane (the black line) and ferrite/cementite interface (the red line) are shown to lie about 5°apart. Blue,black and red spots represent cementite,ferrite and austenite atoms respectively.

Ohmori [65] suggested an interphase nucleation model for cementite when he reported an observation of parallelogram cross sections of cementite-free bainite needles that form at the early stage of bainite transformation. With the same three phase OR expressed before, He explained that cementite is likely to have nucleated on the facets of these ferrite needles or laths in the austenite matrix. Figure 3-28, summarizes this idea. At the end of the transformation, there will be no trace of austenite in the final bainite plate.

Experimental findings of section 3-2 including the orientation of f.c.c./b.c.c. facets, the 3D reconstruction of a bainitic microstructure and the FIB sectioning results can all be explained on the basis of this type of interphase precipitation in our Fe-C-Ni system. On the other hand, it should be noted that the emphasis of this study is to investigate the possibility of nucleation of cementitie on ferrite/austenite interfaces and the correlation of the nucleation morphology of cementite to the growth stage microstructure of cementite in bainite (as discussed by Ohmori) is not the objective of this work. Ohmori uses the experimental interface planes between ferrite and cementite, but in this study the calculated equilibrium interfaces of ferrite/cementite and ferrite/austenite (assuming the O-line ORs also existed at the nucleation stage) will be used as facets of the nucleus in the next section. Achievement of the equilibrium shape at the nucleation stage of a precipitate is an assumption inherent in classical nucleation theory.

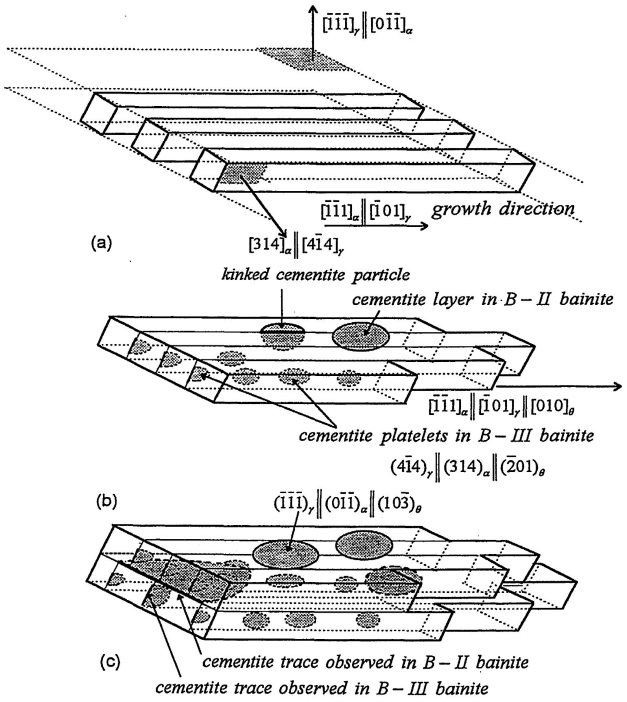

Figure 3-28a- Nucleation of needle like ferrite units.b- precipitation of cementite and c-Coalescence of bainite units into a bainite plate from [65].

3-3-2Thermodynamics/kinetics of interphase boundary nucleation:

In the previous section, interphase boundary nucleation of cementite on ferrite/austenite boundaries was rationalized based on a crystallographic point of view. In this section, this idea will be discussed from thermodynamic/kinetic aspect. In other words, it will be asked whether there will be enough driving force for cementite to nucleate and at what point in the transformation the nucleation event may occur. In order to address this question, a model for the critical nucleus that accounts for the crystallography of the interfaces involved will be developed. First we need to clarify a similar term "interphase boundary precipitation"(IBP) that exists in the literature.

When Honeycomb and Okamoto et al. referred to IBP of carbides at high temperatures, [92, 93] what they meant was the formation of fine banded dispersions (layers) of alloy carbides within the ferrite as shown in Figure 3-29. They provided microscopic evidence that these carbides form on immobile terrace planes of the moving α/γ interfaces. The interfaces were assumed to migrate via a lateral (ledge) mechanism. Aaronson et al. discussed that a similar type of precipitation can also be operative when cementite precipitates in bainite. They proposed that at the nucleation stage, it is highly likely that cementite projects equally into both ferrite and austenite. Later it is thought to grow faster in austenite.

In this work we focus on the possibility of nucleation of cementite on a low energy ferrite/austenite interface ((121) b//(1-13) f) and not the terrace planes. Some of the nucleation equilibrium facets may still appear as observed interfaces after the growth. For example, the observed ferrite/cementite habit plane of the previous section is the equilibrium facet of the nucleation stage but the same statement cannot be true about all the equilibrium interfaces of the nucleation stage. Following our previous discussion on

the crystallography of these three phases, some simplifying assumptions have been made, such as: the faceted ferrite/austenite interfaces form before cementite precipitates; ferrite/austenite, ferrite/cementite and austenite/cementite should share (close to) KS, Isaichev and Pitsch ORs respectively; the lattice parameters of table 2-3 are used. Cementite is considered to penetrate equally in ferrite and austenite. It is also assumed that these low energy semicoherent facets form at the moment of nucleation.

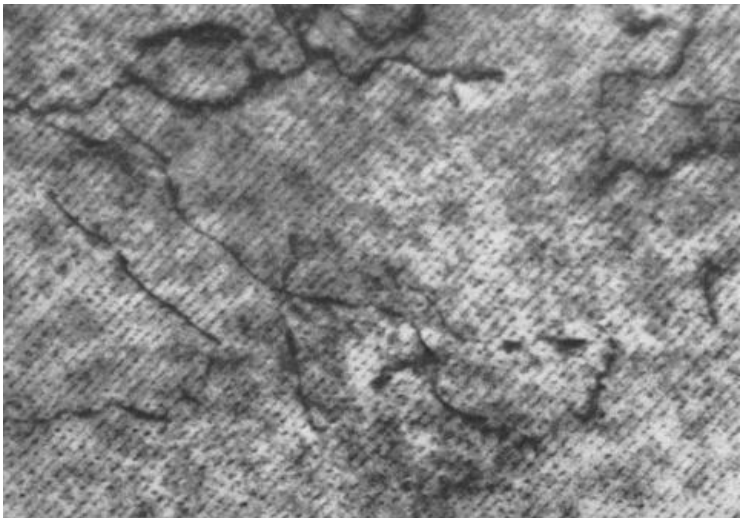

Figure 3-29- Interphase boundary carbide has trailed the prior ferrite/austenite terraces at high temperatures from [92].

The idea can be described by looking at the schematic figure 3-30 when the cross sections of two ferrite laths (similar to those of the experimental observations of section 3-2) are depicted. It is shown that, assuming the interface has a finite intrinsic mobility; it takes the interface a finite time to approach a local equilibrium (in this case a paraequilibrium) interfacial value. At t_3, when the two interfaces have slowed , the carbon content of the retained austenite is assumed to be the one dictated by paraequilibrium (defined in chapter 1, section 1-2-1). This is a reasonable assumption because the alloy composition lies within the PE region of the isothermal section of Fe-C-Ni according to figure 3-31, and the temperature is sufficiently low that substitutional solute mobilities will be

vanishingly small. The picture will be completed by cementite precipitation at the interface. These cementite precipitates then act as carbon sinks, allowing the ferrite to continue growing and fill the entire volume, leaving the cementite surrounded. This picture describes our original assumption that the nucleation of cementite will probably be viable when the interfaces approach paraequilibrium. It will be shown at the end of this section that the higher interfacial carbon content in austenite plays a role in determining the probability of nucleation.

The program for determining the carbon content in the austenite, was originally developed to study the effect of Ni on the thickening kinetics of planar ferritic allotriomphs at high temperatures by Hutchinson et al. [94] In order to do that, the following energy balance on the interface, was solved iteratively to provide interfacial compositions (through the definition of driving force over the interface) as well as interface velocity.

$$\frac{v}{M} = \Delta G_{DF} - \Delta G_{\text{int}}^{diss} \qquad \textit{Eq. 3-13}$$

Where v is the interface velocity, M is the intrinsic mobility, ΔG_{DF} is the driving force for interface migration and ΔG^{diss} is the free energy dissipated by diffusion within the interface.

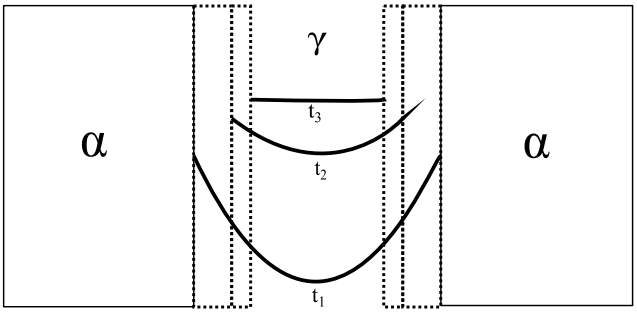

Figure 3-30- The schematic image showing the carbon concentration profiles in austenite at different times between two ferrite laths.

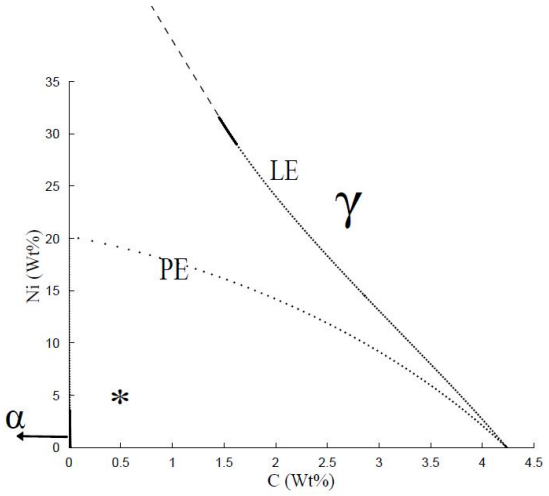

Figure 3-31- Isothermal section of Fe-C-Ni calculated by ThermoCalc. The composition of our steel sample is signified by the asterisk. .

Ni has been known as the alloying element that interacts weakly with the interface, thus ΔG^{diss} is assumed to be 0. Therefore the driving force over the interface is dissipated through volume diffusion and interface migration.

The following interface mobility relationship was assumed:

$$M = M_0 \exp(\frac{-\Delta G}{RT})$$ ***Eq. 3-14***

The M_0 is the exponential prefactor and ΔG is the activation energy for the interface mobility. Incoherent interface values of M_0=5000 M mol/J s and ΔG=147000 J/mol for α/α grain boundaries were used due to lack of mobility data for coherent boundaries. Clearly, semi-coherent α/γ boundaries should have lower mobility values by several orders of magnitude.

Figure 3-32 shows the carbon concentration of the interface with time. Interfacial concentration will reach the paraequilibrium value very quickly. A smaller value of mobility would result in a smaller initial carbon concentration value and a lower slope of the concentration vs. time curve, but the overall behavior would remain the same.

Figure 3-33 displays the cementite nucleation driving force with respect to carbon concentration in austenite, starting from the bulk carbon content and ending in a paraequilibrium carbon content. Similar to the no-partitioning assumption of the α/γ kinetics, driving force data for cementite nucleation were also extracted at paraequilibrium between austenite and cementite. The same assumption has been made in an investigation on carbide precipitation in tempered martensite. [95] (Again, similar to ferrite/austenite case, because of the low transformation temperature and because the substitutional solute diffusional relaxation times are essentially negligible relative to the transformation times.)

Classical nucleation theory has been used to investigate the possibility of the nucleation of cementite on low energy ferrite/austenite boundaries assuming the geometry of the nucleus shape will be determined by favored ferrite/cementite and austenite/cementite interfaces defined in the previous sections.

The aim of this section is to investigate whether with the available driving force will be sufficient for cementite precipitation. i.e. that the Wulff constructed shape of figure 3-34,

is likely to have a noticeable nucleation rate at our temperature of interest. This nucleus shape was drawn using auxillary gamma plots introduced by Jong Lee. [52, 53]

The activation energy for critical nucleus formation ΔG^* depends on the nucleation driving force, interfacial energies of the nucleus surfaces and several geometric parameters of the nucleus shape. Johnson et al. derived the ΔG^* for different possible geometries of a nucleus having crystallographiclly favored facets. Nucleation of an α phase on the interphase boundary between the Guinier-Preston (GP) zones (β) and the matrix γ that only differ compositionally and not crystallographically was among their studied morphologies. They assumed the new α phase would have two parallel facets with both the GP precipitate and the matrix. [50] (in other words the nucleus of figure 3-34 would look like their nucleus if the two facets were parallel)

The present interphase boundary nucleation event will be a more general case in which the nucleation happens on a heterophase boundary. Eq. 3-15 was derived from the nucleation energy balance. f defined by eq. 3-16 is a convenient function that has been repeatedly used in the nucleation literature and g is a new function defined in eq. 3-17 to facilitate the calculation of ΔG^* in this study.

$$\Delta G^* = \Delta G^*_h\{f(\psi_2) - f(\varphi_2)\} + (\frac{\sigma_{\alpha\theta}}{\sigma_{\gamma\theta}})^3 \Delta G^*_h\{f(\psi_1) - g(\theta+\delta)\}$$

Eq. 3-15

$$f(\varphi) = \frac{2 - 3\cos\varphi + \cos^3\varphi}{4}$$

Eq. 3-16

$$g(\theta+\delta) = \frac{(2 + 2\cos^3(\theta+\delta) + 3\cos\delta - 3\cos^3\delta)}{4}$$

Eq. 3-17

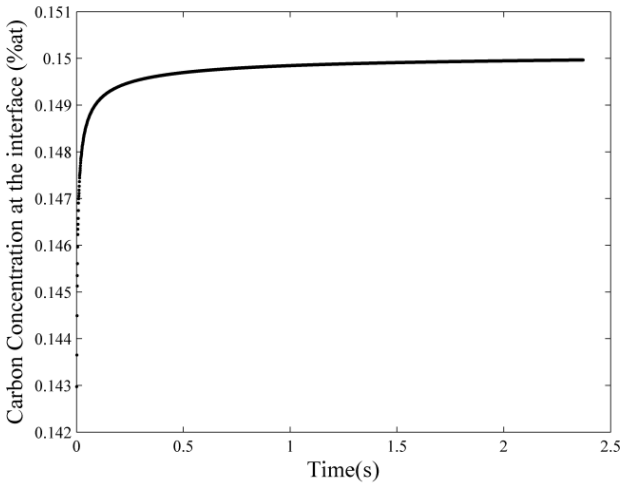

Figure 3-32- Estimated interface concentration (in austenite) vs. time. The paraequilibrium carbon content is reached in a short time when a high mobility interface is

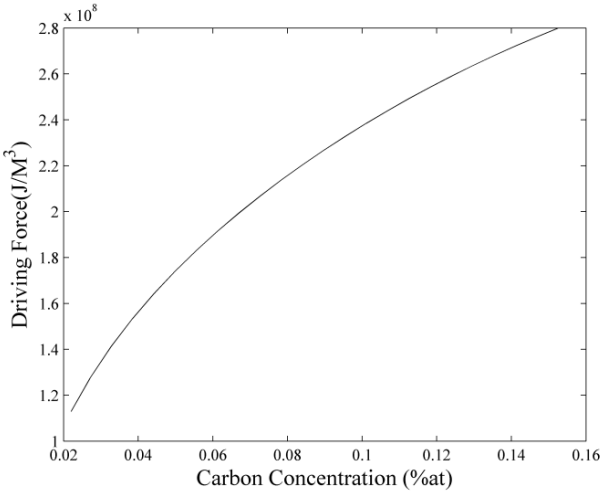

Figure 3-33- Driving force for the precipitation of paraequilibrium cementite vs. carbon concentration.

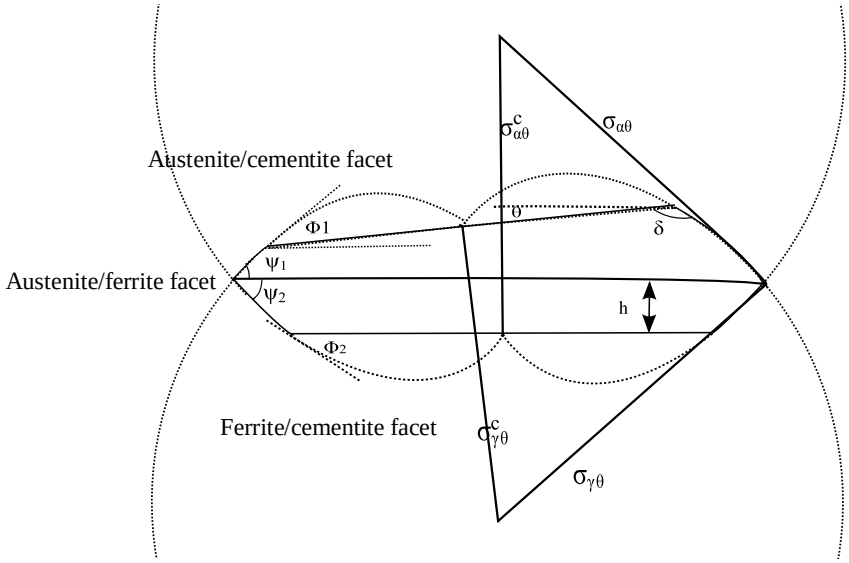

Figure 3-34- Wulff constructed interphase boundary cementite nucleus, drawn using auxiliary gamma plots (the dashed line). The calculated equilibrium interfaces of the previous section were used as the two facets, austenite/cementite and ferrite/cementite.

ΔG^*_h, is the activation energy for a homogenous nucleus, obtained through Eq. 3-18, and $\sigma_{\alpha\theta}$ and $\sigma_{\gamma\theta}$ are incoherent boundary energies between cementite/ferrite and cementite/austenite respectively (as can be seen in figure 3-34).

$$\Delta G^*_h = \frac{16\pi\sigma^3_{\alpha\theta}}{3\Delta G_v^2} \qquad \textit{Eq. 3-18}$$

At $\theta=0$,

$$g(\theta+\delta) = f(\varphi_1) \qquad \textit{Eq. 3-19}$$

The expression for ΔG^* will resemble the one for parallel faceted precipitates. [50] It can be seen in figure 3-34 that the radii of auxiliary gamma plots representing $\sigma_{\alpha\theta}$ and $\sigma_{\gamma\theta}$ are equal. It is physically reasonable to assume that these incoherent interfacial energies have the same magnitude. Consequently ψ_1 and ψ_2 are equal. The critical nucleus radius is represented as follows:

$$r = \frac{2\sigma_{\alpha\theta}}{\Delta G_v} \qquad \textbf{\textit{Eq.}}\ 3\text{-}20$$

Equation 3-12 was derived using the following force balances:

$$\sigma_{\alpha\theta}{}^{c} = \sigma_{\alpha\theta}\cos\varphi_2 \qquad \textbf{\textit{Eq. 3-21}}$$

$$\sigma_{\gamma\theta}{}^{c} = -\sigma_{\gamma\theta}\cos\delta \qquad \textbf{\textit{Eq. 3-22}}$$

$$\sigma_{\gamma\alpha} = \sigma_{\alpha\theta}\cos\psi_1 + \sigma_{\gamma\theta}\cos\psi_2 \qquad \textbf{\textit{Eq. 3-23}}$$

Also for the geometry of figure 3-34 to hold the following relationship should exist:

$$\pi - \delta < \psi_1 \qquad \textbf{\textit{Eq. 3-24}}$$

The angles, ψ_1 and ψ_2, φ_1 and φ_2, δ and θ are shown in figure 3-34. θ is the deviation angle between the calculated equilibrium interfaces of cementite/ferrite and austenite/ferrite from the previous section. h is the height of the nucleus in ferrite. Three layers of (1 2 1) b (the facet plane in ferrite) seems to be a realistic assumption for the height of the nucleus in order to keep the geometry of figure 3-12.

As expressed before, ΔG^* plays a most influential role in the nucleation rate. Therefore in this study we use the criterion of $\Delta G^* = 60$ kT as the highest value which will allow a detectable nucleation rate and investigate the effect of several parameters on the possibility of nucleation. [50]

The calculation results show that for ΔG^* to lie close to the acceptable range of 0-60 kT, the following limitations need to be imposed:

$$\sigma_{\alpha\theta} = \sigma_{\gamma\theta} \leq 0.26 \frac{J}{m^2} \qquad \textit{Eq. 3-25}$$

$$90° \leq \delta \leq 110° \qquad \textit{Eq. 3-26}$$

$$70° \leq \psi_1 = \psi_2 \leq 90° \qquad \textit{Eq. 3-27}$$

Figure 3-35 displays the ΔG^* as a function of carbon concentration, for fixed δ and ψ values of 110° and 70°. θ is taken to be 5° in accordance with the deviation angle between the calculated equilibrium interfaces of cementite/ferrite and cementite/austenite (this incorporates the known crystallography of these facets from the previous section). It can be seen that at the limiting value of interfacial energy, $\sigma_{\alpha\theta}$ = 0.26 J/m^2, ΔG^* approaches the acceptable range for nucleation near the paraequilibrium interfacial carbon content (≈ 0.15 at %). For lower values of interfacial energies, the diagram will be shifted towards the lower left. In other words, nucleation will be feasible for a wider range of carbon contents. The intersection between the ΔG^* = 60kT line and these graphs at varying interfacial energies, will give the lowest critical carbon content required for the nucleation to be possible. The fixed δ and ψ values, used to draw the graphs of figure 3-35 delineate the lower limit of the ΔG^* vs. carbon concentration curves, thus the critical values of carbon content can be extracted. It can be seen that for $\sigma_{\alpha\theta} \leq 0.15$ J/m^2 nucleation will be viable even at bulk carbon concentration of 0.02% C. Therefore it can be seen that the interfacial energy of the facets play a more important role in facilitating the nucleation than a critical carbon content (or driving force).

Figure 3-36 shows the activation energy versus the deviation angle θ at fixed δ, ψ and C% values shown on the diagram. Evidently ΔG^* increases with increasing θ. The acceptable range for θ is $0 \leq \theta \leq 7°$. (7° will be the upper limit of θ for any given δ, ψ and C% values) Therefore the deviation angle of 5° between the known facets of ferrite/cementite and austenite/cementite is acceptable.

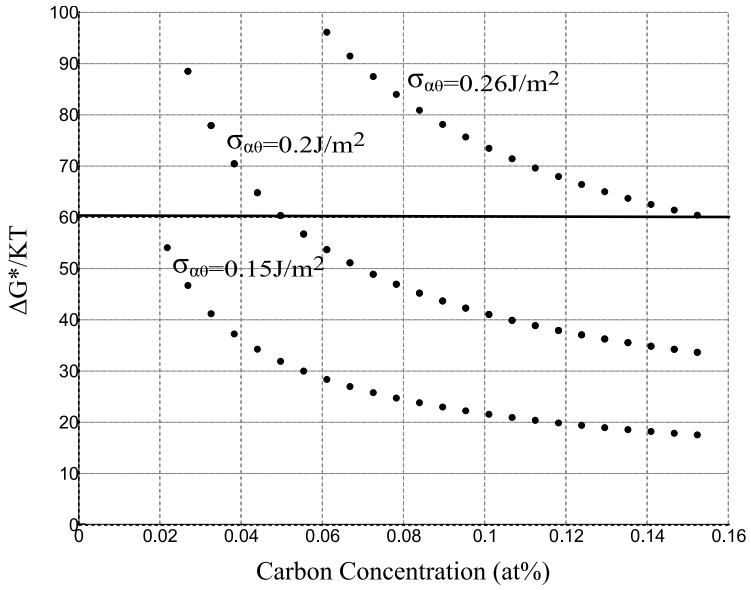

Figure 3-35 - Activation energy for nucleation as a function of carbon content of austenite for varying σαθ interfacial energy values and θ=5°, δ=110° and ψ=70°.

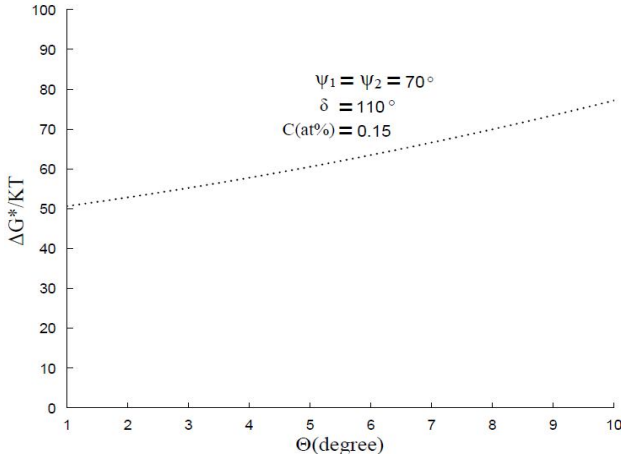

Figure 3-36 - Activation energy for nucleation as a function of the deviation angle θ between the equilibrium ferrite/cementite and austenite/cementite interfaces. The diagram has been drawn for constant values of ψ, δ and carbon content shown on the graph.

Overall, the interphase boundary nucleation of cementite under the range of available austenite carbon contents and a crystallographically meaningful geometry seems to be possible according to a classical nucleation theory.

The range of acceptable ψ and δ values, in addition to the acceptable interfacial energy values, suggests the possibility of a pillbox nucleus model that was already rationalized and used by Enomoto et al. [96] and Tanaka et al. [97] This matter will be further discussed in the summary of section 3-3.

Discussion on the ε plot construction

The Wulff construction of figure 3-34 was drawn based on the derivations by Jong lee et al. [52, 53] and Johnson et al. [50] Around the same time that Jong Lee and Aaronson introduced their extended Wulff construction technique (used in this study), Cahn and Hoffman introduced a vector thermodynamics definition that was briefly described in chapter 1. [54, 55] ε vector defined as follows is a more general term than the scalar γ or the length dependent σ (defined as force per unit length):

$$\boldsymbol{\varepsilon} = \gamma \mathbf{n} + (\partial\gamma / \partial\theta)_{\max} \mathbf{t} \qquad \textit{Eq. 3-28}$$

γ describes the scalar interfacial energy of a surface. n is the unit vector normal to the surface and t is the unit vector tangent to it. It will be shown here that the same conclusion would have been made in this study, had the ε vector methodology been applied.

The relationship between ε and σ is defined through:

$$\boldsymbol{\sigma} = \boldsymbol{\varepsilon} \times \mathbf{l} \qquad \textit{Eq. 3-29}$$

Cahn and Hoffman show that the **ε** vector plot is geometrically similar to Gibbs-Wulff (G-W) construction. An equilibrium shape defined by **ε**-plot if scaled by $-2/\Delta G_v$, yields the same shape in **r** space defined by the G-W form. For example figure 3-34 would remain the same if drawn on the basis of **ε** plot.

The main difference between the G-W form and **ε**-plot arises when sharp corners of the nucleus shape are approached. In the G-W construction, some orientations will be physically unstable and therefore missing from the final equilibrium shape. These missing orientations in the **ε**-plot are introduced as the self intersecting ears of reverse curvature that will eventually be discarded from the final shape. Figure 3-37a depicts this phenomenon.

Johnson et al. after deriving Wulff shapes for multiple faceted morphologies, consider that the same shapes will be concluded by the **ε** vector approach when the **ε** triangle rule at the line junctions are satisfied. [50]

$$\boldsymbol{\varepsilon}_{12} + \boldsymbol{\varepsilon}_{23} + \boldsymbol{\varepsilon}_{31} = 0 \qquad \textit{Eq. 3-30}$$

In Figure 3-37b, this balance along with its correlated surface tension, **σ** , balance can be seen. Johnson et al have shown that after scaling **ε** plot by $-2/\Delta G_v$, the same r_* and h were obtained for this homogenous faceted nucleus.

It can be argued that **ε** plots for heterogeneous nucleation on the grain and interphase boundaries can also lead to the same G-W form. Cahn and Hoffman [55]show that in order for the **ε** plot to be applied to the boundary nucleus in other words for the triangle rule to work, the boundary plane needs to be flat and planar, similar to the nucleus in this study. Thus the nucleus shape of figure 3-34 agrees with Cahn and Hoffman's **ε** vector construction as well.

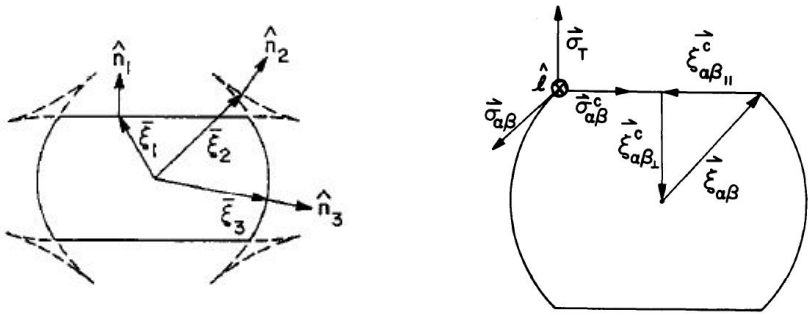

Figure 3-37a- Extended form of equilibrium shape for unstable surfaces from [55] b- Balance of ε vectors for a faceted homogenous nucleus from [50]

Summary and discussion of section 3-3

The idea of cementite nucleation on the interfaces of bainite units in austenite was investigated. When two bainite units start to thicken, the low energy ferrite/austenite interfaces that have a small mobility will approach paraequilibrium condition. It was investigated at what stage of the thickening process the nucleation of cementite will be viable.

The Wulff-constructed nucleus of this study was composed of equilibrium austenite/cementite and ferrite/cementite facets of the type discussed in section 3-1. The nucleation rate of cementite will depend on interfacial energies $\sigma_{\alpha\theta}$ and $\sigma_{\gamma\theta}$, interfacial carbon concentrations and the geometric parameters that were introduced in 3-3-2 (ψ, δ and θ).

The $\Delta G^* \leq 60KT$ criterion was used to test the viability of heterogeneous nucleation of cementite on the ferrite/austenite habit plane, and it was determined that the cemetite/ferrite and cementite/austenite interfacial energies $\sigma_{\alpha\theta}$ and $\sigma_{\gamma\theta}$ (incoherent energy values of the curved region of the nucleus) would need to be $\leq$ 260 mJ (close to the lower

end of 200-500mJ range for the semi-coherent interfaces) for nucleation to be probable. This is an indication that all interfaces surrounding the nucleus should be low-energy facets. For $\sigma_{\alpha\theta} = \sigma_{\gamma\theta} = 260$mJ, nucleation will be only viable at the end of the thickening process, in other words when the carbon content is close the paraequilibrium value. While if $\sigma_{\alpha\theta} = \sigma_{\gamma\theta} < 260$mJ, nucleation will be feasible at a wider range of carbon contents. Therfore a critical interface energy, rather than a critical carbon content is required for a nucleation event to be viable.

Also, the nucleation rate would be significant if the equilibrium facets are less than 7°deviated from each other ($\theta \leq 7^{\circ}$). The equilibrium interfaces in this study are 5°apart.

Finally considering the range of acceptable angles, ψ and δ and low interfacial energies $\sigma_{\alpha\theta}$ and $\sigma_{\gamma\theta}$, the nucleus tends to resemble a coherent pillbox model. The idea of a pillbox model was used by Enomoto et al. for the first time to explain the experimental nucleation rates for ferrite on disordered austenite grain boundaries. [96] Figure 4-1 depicts the pillbox nucleus considered in this study.

As opposed to the previous pillbox models in which the nucleus only extends in one grain, the present cementite pillbox nucleus would extend in both ferrite and austenite. Further discussion on this nucleus model, will depend on evaluation of the edge energy terms. Enomoto et al. used experimental nucleation rate data to derive values for these terms. This study is less deterministic; it does however define a more rigorous formal approach to the problem of interphase boundary nucleation.

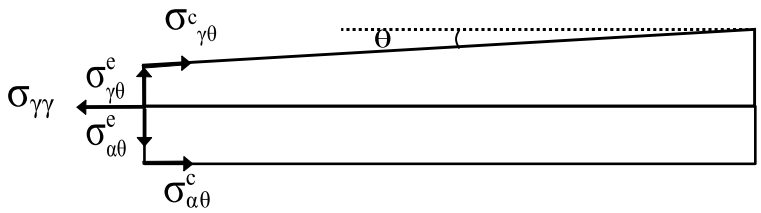

Figure 3-38-The possible pillbox model for the nucleus of figure 3-42.

Chapter 4: Conclusion and suggestions for future work

1- The microstructure of a non silicon containing steel, isothermally transformed to bainite (containing cementite) at 350°c was studied. Ferrite/cementite crystallography and interfacial structure in bainite was studied both experimentally using conventional and high resolution TEM and investigated theoretically using geometrical interfacial models. The observed orientation relationship between ferrite and cementite, the observed habit plane and the O-line direction of cementite precipitates were determined to be a near Isaichev OR, ≈(121)b//(303)c plane and [-1 0 1]b//[1 0 -1]c direction respectively. It was shown that these results were in agreement with the predictions of an O-line model. The observed fringe spacing on ferrite/cementite interfaces had a lower spacing than the dislocation spacing dictated by the O-line model. This disagreement was attributed to the existence of Moiré fringes at the interface. The calculated O-line orientation relationship was used as an input in an NCS model to find favored interfaces other than the habit plane. The highest density NCS plane (Moiré plane) coincides with the habit plane but the observed predominant edge facet of cementite precipitates, did not match a high density NCS plane. This disagreement could be a result of kinetically determined edge facets (rather than equilibrium facets) in cementite.

For the future: Atomistic simulations could be used to calculate the γ-plot for ferrite/cementite system following an Isaichev orientation relationship and to predict the energy cusps corresponding to equilibrium interfaces. The results could be compared with our NCS predictions of favored interfaces. Studies of this type will shed more light on our understanding of optimum interfacial structures.

2- The microstructure of a silicon containing steel, isothermally transformed to bainite at 350°c was studied. The microstructure and crystallography of cementite-free bainite were studied using optical microscopy, SEM and conventional TEM. At low transformation times, cementite-free bainite was composed of accumulated

laths with a common long direction. At longer times, the 3D microstructure of bainite became more complex, presumably composed of a series of overlapping layers that gave rise to a corrugated morphology. The microstructure can still be interpreted as an accumulation of the laths with a long direction that is usually not observed on the 2D surface section. The slow development of bainitic microstructure with time, evident from the optical micrographs, was in qualitative agreement with previously reported kinetic studies, which strongly suggest a diffusional growth process. The orientation relationship and the facet planes of the f.c.c./b.c.c. interface system were characterized. The observed OR lies between KS and NW ORs. Three different facet planes of (1 -1 1)f//(0 1 1)b, (5 -3 3)f//(0 3 5)b and (1 -1 3)f// (1 2 1)b were observed. The first set of planes is the close packed planes in the observed OR.

Also, one set of misfit dislocations were observed on f.c.c./b.c.c. (5 -3 3)f//(0 3 5)b facets and characterized as edge dislocations. The predicted O-line direction with the experimental lattice parameters of ferrite and austenite (following the principles of martensite crystallography and an O-line condition) did not match the observed long direction of the laths which lies close to [0 1 1]f//[-1 0 0]b . It was speculated that the interfacial dislocation structure can change with transformation time. The possible importance of the transformation time on the interfacial structure has been previously emphasized in the literature.

For the future: As discussed in chapter 3, the growth and development of bainitic microstructure in Si containing steels (with no cementite) is complex. More SEM/FIB, conventional TEM and *In situ* experiments on a series of heat treated samples at different times (and temperatures) are required to study the development of the evolution of this microstructure with time. Only then, a more comprehensive theory on its development can be put forward.

3- The multiple variant appearance of cementite in tempered martensite was compared with the single variant appearance of cementite in bainite. The unique

orientation of cementite was attributed to its interphase boundary nucleation on low energy austenite/ferrite interface. The three phase relationship between ferrite, austenite and cementite was discussed crystallographically. It was argued that if ferrite and cementite were to follow a variant of Isaichev OR and cementite and if austenite were to follow a variant of Pitsch OR, then a variant of the KS OR could be detected between ferrite and austenite. This three phase crystallography was shown to also extend to the correlated interfaces between the three phases. A model for cementite nucleation was proposed in which the crystallographiclly calculated interface planes of austenite/cementite and ferrite/cementite surround the nucleus. The purpose of the nucleation model was to find out whether the nucleation of cementite would be viable at the available driving forces of cementite precipitation in our study. It was shown that interfacial energies between ferrite/cementite and ferrite/austenite play a more important role than the interfacial carbon content (nucleation driving force) in lowering the barrier for nucleation. $\sigma_{\theta\gamma}$ and $\sigma_{\theta\alpha}$ should be lower than 0.26 J/m^2 for ΔG^* to be $\leq$ 60 kT at any interfacial carbon content value. This limit for interfacial energy along with the range of possible geometric angles of the nucleus suggests a pillbox model for cementite nucleus. A similar model has been used in the literature to explain grain boundary nucleation of a second phase on high energy austenite grain boundaries. The pillbox nucleus of this study is a more general form than the ones described before and has been more rigorously defined.

For the future: *In situ* SEM studies at high resolutions where cementite can be resolved and at early transformation times could be used to confirm the interphase boundary nucleation of cementite. The details of the crystallography of the three phases at the moment of nucleation on the other hand, will be difficult to experimentally detect, unless one could find an alloy composition that would allow the coexistence of the three phases and would enable us to study the three phase orientation relationship.

Appendix A

In order to define NCS or good matching sites at the interface, atomic positions of cementite atoms need to be determined. The O-line model is used to define these positions on a certain interface and the transformation strain **A** between cementite and ferrite. **A** is then used to define ferrite atoms around each cementite atom at the interface.

For each cementite atom position xc, its b.c.c. neighbors in other words, a 3D network of ferrite atoms positions, will be created around the transformed atom CAx_c through A-1. (n is an integer, the bigger the n value, the wider the range of b.c.c. atoms created)

C is the correspondence matrix that relates the atom positions in b.c.c. and cementite defined in A-2.

$$x_b = CAx_c + \sum_{l=1}^{9} \sum_{i,j,k=-n}^{n} b_{lijk} \qquad \text{A-1}$$

$$X_b = CX_c \qquad \text{A-2}$$

The misfit between cementite atoms and their neighbors will be checked each time. The near coincident criterion of <=15% $|b^L|$ misfit will define the good matching clusters of atoms and consequently favored interfaces.

$$\left|x_b - x_c\right| \le 15\% \left|b^L\right| \qquad \text{A-3}$$

The following *MATLAB* code will first calculate the O-line OR and then the NCS sites in a coordinate system defined by the invariant line, the habit plane normal and their cross product.

```
clear all;
close all;
format long
aalpha=0.452; % Lattice parameters of cementite
balpha=0.509;%
calpha=0.673;%
abeta=0.286;  % Lattice parameter of ferrite

Salpha=structurematrix([aalpha,balpha,calpha,90*pi/180,90*pi/180,90*pi/1
80]);
Salphar=Salpha^(-1)';   % A funtion that defines cubic lattices
Sbeta=structurematrix([abeta,abeta,abeta,90*pi/180,90*pi/180,90*pi/180])
;
Sbetar=Sbeta^(-1)';  % A funtion that defines cubic lattices

       gal=[-1 0 -3;2 0 0; 0 6 0];  % The correlated b.c.c./orthorhombic
                                              vectors in recip.lattice
gbl=[-1 -1 0;0 1 1;2 -2 2];
Cr=gbl'*(gal')^(-1);      % Defining the correspondence
Corres=Cr^(-1)';
bx=Sbeta^(-1)'*[-1 -1 0]'/norm(Sbeta^(-1)'*[-1 -1 0]');
  %Defining an orthogonal coordinate in b.c.c.
by=Sbeta^(-1)'*[1 -1 -2]'/norm(Sbeta^(-1)'*[1 -1 -2]');
bz=Sbeta^(-1)'*[2 -2  2]'/norm(Sbeta^(-1)'*[2 -2  2]');
gb=[dot(Sbeta^(-1)'*gbl(1,:)',bx) dot(Sbeta^(-1)'*gbl(1,:)',by)
dot(Sbeta^(-1)'*gbl(1,:)',bz);dot(Sbeta^(-1)'*gbl(2,:)',bx) dot(Sbeta^(-
1)'*gbl(2,:)',by) dot(Sbeta^(-1)'*gbl(2,:)',bz);dot(Sbeta^(-
1)'*gbl(3,:)',bx) dot(Sbeta^(-1)'*gbl(3,:)',by) dot(Sbeta^(-
1)'*gbl(3,:)',bz)]
Sbeta^(-1)'*gbl(1,:)'
ax=Salpha^(-1)'*[-1 0 -3]'/norm(Salpha^(-1)'*[-1 0 -3]');
%Defining an orthogonal coordinate in orthorhombic
az=Salpha^(-1)'*[0 6 0]'/norm(Salpha^(-1)'*[0 6 0]');
ay=cross(Salpha*[0 1 0]',Salpha^(-1)'*[-1 0 -3]');
ay=ay/norm(ay);
ga=[dot(Salpha^(-1)'*gal(1,:)',ax) dot(Salpha^(-1)'*gal(1,:)',ay)
dot(Salpha^(-1)'*gal(1,:)',az);dot(Salpha^(-1)'*gal(2,:)',ax)
dot(Salpha^(-1)'*gal(2,:)',ay) dot(Salpha^(-
1)'*gal(2,:)',az);dot(Salpha^(-1)'*gal(3,:)',ax) dot(Salpha^(-
1)'*gal(3,:)',ay) dot(Salpha^(-1)'*gal(3,:)',az)]
Salpha^(-1)'*gal(1,:)';

 a0r=gb'*(ga^(-1)'); % original A0 trans. strain

%Transformation matrix from lattice to orthogonal coordinates
%r stands for in the recip.space.
    qalphar=ga'*(gal^(-1)')
    qbetar=gb'*(gbl^(-1)')

 %transformation in the direct space.
    qalpha=qalphar^(-1)';
    qbeta=qbetar^(-1)';
```

```
%determine the rotation angle necessary to get to delta g parallel
state(to define OR):

for Rangle = 0.11:0.0000001:0.22

Rangle=Rangle/180*pi;
% rotate counter clockwise around [010]c
R=[cos(Rangle) -sin(Rangle) 0; sin(Rangle) cos(Rangle) 0; 0 0 1];
 Ar=gb'*ga^(-1)'*R';
qalphar=R*ga'*(gal^(-1)');
qalpha=qalphar^(-1)';
A=Ar^(-1)';
 [v,d]=eig(Ar);
 T=eye(3)-inv(A);
 if  abs(det(T))<1e-7


   break;

 end

end

 Ar=gb'*ga^(-1)'*R';
Rangle/pi*180
 A=Ar^(-1)';
 [v,d]=eig(A)
 T=eye(3)-inv(A);
qalphar=R*ga'*(gal^(-1)');
qalpha=qalphar^(-1)';

%% Now that transformation strain and orthogonal coords are there, we
calc the NCS%%
l=0
p=[0 0 0;1 0 0;0 1 0;0 0 1;1 1 0;1 0 1;0 1 1;1 1 1;0.5 0.5 0.5];% atom
positions in b.c.c.
v1=qalpha*[1 0 -1]';
cem =[0.1841 0.0571 0.3329;0.8159 0.9429 0.6671; 0.3159 0.9429 0.8329;
0.6841 0.0571 0.1671; 0.8159 0.5571 0.6671; 0.1841 0.4429 0.3329; 0.6841
0.4429 0.1671; 0.3159 0.5571 0.8329; 0.0336 0.25 0.8409; 0.9664 0.75
0.1591;  ...
    0.4664 0.75 0.3409;0.5336 0.25 0.6591];
cem_atom=[cem(:,3) cem(:,1) cem(:,2)]' %atom positions in a cem unit
cell pnma space group with the old lattice parameter order , taken from
crystal data bases
sub=[0 0 0]-[0.6591 0.5336  0.25]; %shifting cem atoms to match our
b.c.c. crystal at (0 0 0)


z=0;% creating a 3D cube of cementite
hold on
```

```
for i=-25:25
    for j=-25:25
        for k=-25:25
            for f=1:12
                r=cem_atom(:,f);
                r=r+sub';
                s=[r(1)+i r(2)+j r(3)+k]';
                x=qalpha*s;
                z=z+1;
                keepc(:,z)=s;
                cemc(:,z)=x;
                xb.c.c.=Corres*A*keepc(:,z);
                xb.c.c.c=floor(xb.c.c.);
                 for ii=1:9
                    for aa=-5:5
                        for bb=-5:5
                            for cc=-5:5
                                pp(ii,:)=[p(ii,1)+aa p(ii,2)+bb
p(ii,3)+cc];
                                ppc=xb.c.c.c+pp(ii,:)';
 % creating the b.c.c. neighbors of each cementite atom
                                if norm(qbeta*ppc-
qalpha*keepc(:,z))<=0.035 % checking the criterion of matching
                                    l=l+1;
                                    cemm=qalpha*keepc(:,z);
                                    lee(:,l)=cemm;
                                    b.c.c.p=qbeta*ppc;
                                    bee(:,l)=b.c.c.p;
                                                % plotting the NCS
                                    plot3(cemm(1),cemm(2),cemm(3),'k.')


plot3(b.c.c.p(1),b.c.c.p(2),b.c.c.p(3),'bo')

                                end
                            end

                        end
                    end
                end
            end
            %
        end
    end
end
axis('equal')
view(qalpha*[0 1 0]')
[vv dd]=eig(A)
view(qalphar*[1 0 1]')
view(vv(:,1))
% definition of interface planes, deltags%%
% principal delta gs
deltag7=T'*qalphar*[1 0 1]' ;%green
```

```
deltag8=T'*qalphar*[1 2 1]';%dark green[0 0.5 0]
deltag9=T'*qalphar*[0 3 4]';% brown[0.8 0.5 0]
deltag10=T'*qalphar*[1 0 -3]';%cobalt blue [0.25 0.25 0.9]%HP
deltag11=T'*qalphar*[0 -2 2]';%cyan, the best trace (0 1 -1)b.c.c.
deltag12=T'*qalphar*[0 2 4]';%magenta
deltag13=T'*qalphar*[2 -2 2]';%black
deltag14=T'*qalphar*[2 2 -2]';%blue
deltag15=T'*qalphar*[1 0 3]';%HP
deltag16=T'*qalphar*[2 0 0]';%HP
deltag17=T'*qalphar*[1 -2 -1]'

% saving the position of good matching sites (or NCS
) for future use
 fid = fopen('num5Lee.txt', 'w');
fprintf(fid, '%12.6f %12.6f %12.6f\n', lee);
fclose(fid);
fid = fopen('num5Bee.txt', 'w');
fprintf(fid, '%12.6f %12.6f %12.6f\n', bee);
fclose(fid);

%% drawing NCS from the saved positions of NCS atoms %%
pee=importdata('num5Lee.txt');
mee=importdata('num5Bee.txt');
sizepee=size(pee)
sizemee=size(mee)
% w=deltag7
% defining a coordinate system with x, y and z parallel with IL,HP
normal and their cross product
[vv dd]=eig(A)
xx=vv(:,1)/norm(vv(:,1))
zz=-n/norm(n)
yy=cross(xx,zz)/norm(cross(xx,zz));
transM=[xx yy zz];
transM=transM^(-1);
delta=qalphar*[2 -2 2]'

figure
hold on
sheri=0;%% drawing the NCS on different interface planes that are
defined by deltags%%
for l=1:sizemee(1,1)
peer(:,l)=transM*pee(l,:)';
meer(:,l)=transM*mee(l,:)';
if abs(peer(:,l)'*(transM*delta))<=0.05
    sheri=sheri+1;
plot3(peer(1,l),peer(2,l),peer(3,l),'k.')
plot3(meer(1,l),meer(2,l),meer(3,l),'ro','MarkerSize',4)

 %end
end
view([1 0 0])
view(-transM*delta)
xlabel('IL (nm)','FontName','Times New Roman','FontSize',16)
```

```
ylabel('IL*HP (nm)','FontName','Times New Roman','FontSize',16)
zlabel('HP (nm)','FontName','Times New Roman','FontSize',16)
axis('equal')

 %axis([-20 20 -20 20 -20 20])

%% drawing the traces deltags 10=deltag1,11=deltag2,5=deltag4 and
17=deltag3

hold on
delta=T'*qalphar*[0 -2 2]'
del1=(transM*delta)/norm(transM*delta)
btranslate=(1/norm(delta))*del1

hold on % function to draw an interface Trace
for i=-10:10
    plotline(i*btranslate-60*cross([1 0
0]',transM*delta),i*btranslate+60*cross([1 0 0]',transM*delta),'b')

end
```

Appendix B

Fick's second law for a planar geometry can be easily programmed using the Murray-Landis finite difference method as follows:

$$\frac{C_i^{t2} - C_i^{t1}}{\Delta t} = D\frac{(C_{i-1} - 2C_i + C_{i+1})}{\Delta x^2} + v\frac{(n-i)}{(n-1)}\frac{(C_{i+1} - C_{i-1})}{2\Delta x} \qquad \textbf{B-1}$$

The explicitly discretized equation above is used to solve carbon concentration in austenite for a moving interface (moving grid) and it will be stable when:

$$\Delta t \le (\Delta x^2)/(2D) \qquad \textbf{B-2}$$

Where Δt is the time increment and Δx is the changing grid size. Ni is the alloying element in our system and it is thought to interact weakly with the interface.

Boundary condition for the diffusion problem in our case will be the paraequilibrium carbon concentration in the bulk.

The Driving force over the interface is calculated through:

$$\Delta G^{DF} = \frac{(U_{Ni}^{fcc} + U_{Ni}^{bcc})}{2}.(\mu_{Ni}^{fcc} - \mu_{Ni}^{bcc}) + \frac{(U_{Fe}^{fcc} + U_{Fe}^{bcc})}{2}.(\mu_{Fe}^{fcc} - \mu_{Fe}^{bcc}) - v/M \qquad \textbf{B-3}$$

Where v is the velocity of interface and M is a finite mobility.

Also U fractions are defined as:

$$U_{x \neq c} = \frac{Xx}{1 - Xc} \qquad \textbf{B-4}$$

Where X is the mole fraction of a component.

This equation will reduce to the paraequilibrium eq. when the substitutional alloying element content is the same in both ferrite and austenite.

At each loop the driving force is set to 0 to obtain carbon concentration of the interface and subsequently interface velocity will be updated from a mass balance in ferrite and austenite:

$$v(C^{\gamma/\alpha} - C^{\alpha}) = J^{\gamma} - J^{\alpha} \qquad \textbf{B-5}$$

J is the flux of carbon in the two phases. J_{α} is assumed to be 0. Also diffusion coefficient of C in both ferrite and austenite will be updated using Agren's diffusivity data.[98]

Appendix C

In section 3-2, the f.c.c. -b.c.c. O-line model was briefly described. The goal is finding the invariant line x, in direct lattice in a non-martensitic transformation. After obtaining the invariant line in reciprocal lattice, x^*, invariant line strain can be determined through C-1:

$$[(R_1 B)^{-1}]' x^* = x^* \qquad \textbf{C-1}$$

Where B is the Bain strain and R_1 is defined by C-2:

$$R_1 = R_a R_b' \qquad \textbf{C-2}$$

The three columns in R_a include x^*, $b^L/|b^L|$, and their cross product. The three columns that constitute R_b are x^*_B (reciprocal IL after the Bain strain), $b^L_B/|b^L_B|$ (b^L_B is the Burgers vector after the Bain strain) and their cross product. It can be shown that R_1 rotates x^*_B and b^L_B into x^* and b^L respectively. A third rotation around x^* does not violate the O-line condition which gurantees that x^* is normal to b^L.

Rotation from -15° to 15° around x^*, to find the IL x, in direct lattice needs to be confined with more conditions. Qiu and Zhang [82], introduced minimum deviation from a rational OR (such as KS or NW) and maximum dislocation spacing on the interface to be good criteria for obtaining the IL in direct lattice x.

References

[1] H. K. D. H. Bhadeshia, *Bainite in steels : transformations, microstructure and properties*, 2nd ed. IOM Communications: London, 2001.

[2] *Phase transformations in steels: Fundamentals and diffusion-controlled transformations, edited by E.Pereloma, D.V.Edmonds* vol. 1, part 3: bainite and diffusional-displacive phase transformations: Woodhead online publishing, 2012.

[3] T. Moritani, N. Miyajima, T. Furuhara, and T. Maki, "Comparison of interphase boundary structure between bainite and martensite in steel," *Scripta Materialia,* vol. 47, pp. 193-199, 8/2/ 2002.

[4] C. Li, V. Perovic, and G. R. Purdy, in *proceeding of the conference on Phase Transformations, edited by G.W.Lorimer*, London, 1987, pp. 326–329.

[5] W. Z. Zhang and G. C. Weatherly, "On the crystallography of precipitation," *Progress in Materials Science,* vol. 50, pp. 181-292, 2005.

[6] W.Z.Zhang and G.Purdy, "O-lattice analyses of interfacial misfit. I. General considerations," *Philosophical Magezine A,* vol. 68, pp. 279-290, 1993.

[7] W.Bollmann, *Crystal lattices, interfaces, matrices*. Geneva: W.Bollmann, 1982.

[8] W. Bollmann, *Crystal defects and crystalline interfaces*. Springer-Verlag: Berlin ;, 1970.

[9] C. M. Wayman, *Introduction to the crystallography of martensitic transformations*. Macmillan: New York, 1964.

[10] J. W. Christian, *The theory of transformations in metals and alloys : an advanced textbook in physical metallurgy*, 2d ed. Pergamon Press: Oxford ;, 1975.

[11] J. K. Lee, "Morphology of coherent precipitates via a discrete atom method," *Materials Science and Engineering: A,* vol. 238, pp. 1-12, 10/30/ 1997.

[12] A. G. Khachaturyan, *Theory of structural transformations in solids*. Wiley: New York, 1983.

[13] H. Okamoto and M. Oka, "Coupling of thin plate martensite in Fe-Ni-C alloy," *Materials Transactions JIM,* vol. 19, pp. 674-684, 1978.

[14] D. B. Williams, *Transmission electron microscopy : a textbook for materials science*. Plenum Press: New York, 1996.

[15] B. Fultz and J. M. Howe, *Transmission Electron Microscopy and Diffractometry of Materials*, Third ed. Springer-Verlag Berlin Heidelberg: Berlin, Heidelberg, 2008.

[16] J. W. Edington, *Practical electron microscopy in materials science*. Van Nostrand Reinhold Co.: New York, 1976.

[17] G. V. Kurdjumov, *Zhur. Tekhn. Fiziki.*, vol. 18, 1948.

[18] B. P. J. Sandvik and C. M. Wayman, "Characteristics of lath martensite: Part II. The martensite-austenite interface," *Metallurgical Transactions A,* vol. 14, pp. 823-834, 1983/04/01 1983.

[19] G. R. Srinivasan and C. M. Wayman, "The crystallography of the bainite transformation—I," *Acta Metallurgica,* vol. 16, pp. 621-636, 5// 1968.
[20] B. C. Muddle, J. F. Nie, and G. R. Hugo, "Application of the theory of martensite crystallography to displacive phase transformations in substitutional nonferrous alloys," *Metallurgical and Materials Transactions A,* vol. 25, pp. 1841-1856, 1994/09/01 1994.
[21] U. Dahmen, "Orientation relationships in precipitation systems," *Acta Metallurgica,* vol. 30, pp. 63-73, 1// 1982.
[22] U. Dahmen, P. Ferguson, and K. H. Westmacott, "Invariant line strain and needle-precipitate growth directions in Fe-Cu," *Acta Metallurgica,* vol. 32, pp. 803-810, 5// 1984.
[23] U. Dahmen, "The role of the invariant line in the search for an optimum interphase boundary by O-lattice theory," *Scripta Metallurgica,* vol. 15, pp. 77-81, 1// 1981.
[24] C. P. Luo and G. C. Weatherly, "The interphase boundary structure of precipitates in a Ni-Cr alloy," *Philosophical Magazine A,* vol. 58, pp. 445-462, 1988/09/01 1988.
[25] C. P. Luo and G. C. Weatherly, "The invariant line and precipitation in a Ni-45 wt% Cr alloy," *Acta Metallurgica,* vol. 35, pp. 1963-1972, 8// 1987.
[26] W.Z.Zhang and G.Purdy, "O-lattice analyses of interfacial misfit. II. Systems containing invariant lines," *Philosophical Magezine A,* vol. 68, pp. 291-303, 1993.
[27] H. Grimmer, "A reciprocity relation between the coincidence site lattice and the DSC lattice," *Scripta Metallurgica,* vol. 8, pp. 1221-1223, 11// 1974.
[28] F. Ye and W. Z. Zhang, "Coincidence structures of interfacial steps and secondary misfit dislocations in the habit plane between Widmanstätten cementite and austenite," *Acta Materialia,* vol. 50, pp. 2761-2777, 6/28/ 2002.
[29] M. G. Hall, J. M. Rigsbee, and H. I. Aaronson, "Application of the “0” lattice calculation to f.c.c./b.c.c. interfaces," *Acta Metallurgica,* vol. 34, pp. 1419-1431, 7// 1986.
[30] R. C. Ecob and B. Ralph, "A model of the equilibrium structure of F.C.C./B.C.C. interfaces," *Acta Metallurgica,* vol. 29, pp. 1037-1046, 6// 1981.
[31] J. M. Rigsbee and H. I. Aaronson, "A computer modeling study of partially coherent f.c.c.:b.c.c. boundaries," *Acta Metallurgica,* vol. 27, pp. 351-363, 3// 1979.
[32] W. Z. Zhang and G. R. Purdy, "A TEM study of the crystallography and interphase boundary structure of α precipitates in a Zr-2.5 wt% Nb alloy," *Acta Metallurgica et Materialia,* vol. 41, pp. 543-551, 2// 1993.
[33] M. G. Hall, H. I. Aaronson, and K. R. Kinsma, "The structure of nearly coherent fcc: bcc boundaries in a Cu-Cr alloy," *Surface Science,* vol. 31, pp. 257-274, 6// 1972.
[34] Q. Liang and W. T. Reynolds, "Determining interphase boundary orientations from near-coincidence sites," *Metallurgical and Materials Transactions A,* vol. 29A, 1998.

[35] D. Qiu and W. Z. Zhang, "An extended near-coincidence-sites method and the interfacial structure of austenite precipitates in a duplex stainless steel," *Acta Materialia,* vol. 56, pp. 2003-2014, 5// 2008.

[36] F. Ye, W. Z. Zhang, and D. Qiu, "Near-coincidence-sites modeling of the edge facet dislocation structures of α precipitates in a Ti–7.26 wt.% Cr alloy," *Acta Materialia,* vol. 54, pp. 5377-5384, 12// 2006.

[37] J. W. Cahn and G. Kalonji, in *Proceedings of the conference on solid–solid phase transactions,edited by H. I.. Aaronson, D. E. Laughlin, R. F. Sekerka and C. M.. Wayman, (AIME) Pittsburgh,* 1981, p. 3.

[38] R. C. Pond, X. Ma, Y. W. Chai, and J. P. Hirth, "Chapter 74 Topological Modelling of Martensitic Transformations," in *Dislocations in Solids*. vol. Volume 13, F. R. N. Nabarro and J. P. Hirth, Eds., ed: Elsevier, 2007, pp. 225-261.

[39] J. M. Howe, R. C. Pond, and J. P. Hirth, "The role of disconnections in phase transformations," *Progress in Materials Science,* vol. 54, pp. 792-838, 8// 2009.

[40] G.Nolze, "Characterization of the fcc/bcc orientation relationship by EBSD using pole figures and variants," *Zeitshrift Fuer Metallkunde,* vol. 95, pp. 744--755, 2004.

[41] H. Kitahara, R. Ueji, M. Ueda, N. Tsuji, and Y. Minamino, "Crystallographic analysis of plate martensite in Fe–28.5 at.% Ni by FE-SEM/EBSD," *Materials Characterization,* vol. 54, pp. 378-386, 5// 2005.

[42] H. Kitahara, R. Ueji, N. Tsuji, and Y. Minamino, "Crystallographic features of lath martensite in low-carbon steel," *Acta Materialia,* vol. 54, pp. 1279-1288, 3// 2006.

[43] G. Miyamoto, N. Takayama, and T. Furuhara, "Accurate measurement of the orientation relationship of lath martensite and bainite by electron backscatter diffraction analysis," *Scripta Materialia,* vol. 60, pp. 1113-1116, 6// 2009.

[44] S. Morito, H. Tanaka, R. Konishi, T. Furuhara, and T. Maki, "The morphology and crystallography of lath martensite in Fe-C alloys," *Acta Materialia,* vol. 51, pp. 1789-1799, 4/2/ 2003.

[45] A. Van der Ven and L. Delaey, "Models for precipitate growth during the $\gamma \rightarrow \alpha + \gamma$ transformation in Fe-C and Fe-C-M alloys," *Progress in Materials Science,* vol. 40, pp. 181-264, // 1996.

[46] M. Hillert and M. Rettenmayr, "Deviation from local equilibrium at migrating phase interfaces," *Acta Materialia,* vol. 51, pp. 2803-2809, 6/11/ 2003.

[47] M. Hillert and B. Sundman, "A treatment of the solute drag on moving grain boundaries and phase interfaces in binary alloys," *Acta Metallurgica,* vol. 24, pp. 731-743, 8// 1976.

[48] M.Hillert, "Paraequilibrium", *Internal report swedish Inst. Metal. Res.,* 1953.

[49] K. Russell, "Nucleation in solids: The induction and steady state effects," *Advances in Colloid and Interface Science,* vol. 13, pp. 205-318, 1980.

[50] W.C.Johnson, C.L.White, P.E.Marth, and P.K.Ruf, "Influence of Crystallography on aspects of Solid-Solid Nucleation Theory," *Metallurgical Transactions A,* vol. 6A, pp. 911-919, 1975.

[51] J. Lee, D. M. Barnett, and H. I. Aaronson, "The elastic strain energy of coherent ellipsoidal precipitates in anisotropic crystalline solids," *Metallurgical Transactions A,* vol. 8, pp. 963-970, 1977/06/01 1977.

[52] J. K. Lee and H. I. Aaronson, "Influence of faceting upon the equilibrium shape of nuclei at grain boundaries—I. Two-dimensions," *Acta Metallurgica,* vol. 23, pp. 799-808, 7// 1975.

[53] J. K. Lee and H. I. Aaronson, "Influence of faceting upon the equilibrium shape of nuclei at grain boundaries—II. Three-dimensions," *Acta Metallurgica,* vol. 23, pp. 809-820, 7// 1975.

[54] D. W. Hoffman and J. W. Cahn, "A vector thermodynamics for anisotropic surfaces: I. Fundamentals and application to plane surface junctions," *Surface Science,* vol. 31, pp. 368-388, 6// 1972.

[55] J. W. Cahn and D. l. Hoffman, "A vector thermodlnamics for anisotropic surfaces—II. Curved and faceted surfaces," *Acta Metallurgica,* vol. 22, pp. 1205-1214, 10// 1974.

[56] J. K. Lee, D. W. Dooley, D. E. Graham, S. P. Clough, C. L. White, and H. I. Aaronson, "Two families of analytic γ-plots and their influence upon homogeneous nucleation kinetics," *Surface Science,* vol. 62, pp. 695-706, 2// 1977.

[57] H. I. Aaronson, W. T. Reynolds, Jr., and G. R. Purdy, "The incomplete transformation phenomenon in steel," *Metallurgical and Materials Transactions A,* vol. 37, pp. 1731-1745, 2006/06/01 2006.

[58] H.-S. Fang, J.-J. Wang, Z.-G. Yang, C. M. Li, Y. K. Zheng, and C. X. Li, "Formation of bainite in ferrous and nonferrous alloys through sympathetic nucleation and ledgewise growth mechanism," *Metallurgical and Materials Transactions A,* vol. 27, pp. 1535-1545, 1996/06/01 1996.

[59] V. Perovic, G. R. Purdy, and L. M. Brown, "Autocatalytic nucleation and elastic stabilization of linear arrays of plate-shaped precipitates," *Acta Metallurgica,* vol. 29, pp. 889-902, 5// 1981.

[60] E. S. K. Menon and H. I. Aaronson, "Overview no. 57 Morphology, crystallography and kinetics of sympathetic nucleation," *Acta Metallurgica,* vol. 35, pp. 549-563, 3// 1987.

[61] H. I. Aaronson, G. Spanos, R. A. Masamura, R. G. Vardiman, D. W. Moon, E. S. K. Menon, *et al.*, "Sympathetic nucleation: an overview," *Materials Science and Engineering: B,* vol. 32, pp. 107-123, 7// 1995.

[62] G. R. Purdy and M. Hillert, "Overview no. 38: On the nature of the bainite transformation in steels," *Acta Metallurgica,* vol. 32, pp. 823-828, 6// 1984.

[63] M. Hillert and G. R. Purdy, "On the misuse of the term bainite," *Scripta Materialia,* vol. 43, pp. 831-833, 10/16/ 2000.

[64] Y. Ohmori, Y. C. Jung, K. Nakai, and H. Shioiri, "Bainite transformation and the diffusional migration of bainite/austenite broad interfaces in Fe-9%Ni-C alloys," *Acta Materialia,* vol. 49, pp. 3149-3162, 9/20/ 2001.
[65] Y. Ohmori and Y.-C. Jung, "Crystallographic Analysis of Upper Bainite in Fe-9%Ni-C Alloys," *Materials Transactions JIM,* vol. 37, pp. 1665-1671 1996.
[66] G. Spanos, "The fine structure and formation mechanism of lower bainite," *Metallurgical and Materials Transactions A,* vol. 25, pp. 1967-1980, 1994/09/01 1994.
[67] A. Borgenstam, M. Hillert, and J. Ågren, "Metallographic evidence of carbon diffusion in the growth of bainite," *Acta Materialia,* vol. 57, pp. 3242-3252, 6// 2009.
[68] R. Trivedi, "The role of interfacial free energy and interface kinetics during the growth of precipitate plates and needles," *Metallurgical Transactions,* vol. 1, pp. 921-927, 1970/04/01 1970.
[69] D. Quidort and Y. J. M. Brechet, "Isothermal growth kinetics of bainite in 0.5% C steels," *Acta Materialia,* vol. 49, pp. 4161-4170, 12/3/ 2001.
[70] B. P. J. Sandvik, "The Bainite reaction in Fe-Si-C Alloys: The primary stage," *Metallurgical Transactions A,* vol. 13, pp. 777-787, 1982/05/01 1982.
[71] D. N. Shackleton and P. M. Kelly, "The crystallography of cementite precipitation in the bainite transformation," *Acta Metallurgica,* vol. 15, pp. 979-992, 6// 1967.
[72] B. YU, *Dokl. Akad. Nauk. SSSR.* , vol. 73, 1950.
[73] I. Isaichev, *Zhur. Tekhn. Fiziki.* , vol. 17, 1947.
[74] G. R. Srinivasan and C. M. Wayman, "Transmission electron microscope study of the bainite transformation in iron-chromium-carbon alloys," *Acta Metallurgica,* vol. 16, pp. 609-620, 5// 1968.
[75] H. K. D. H. Bhadeshia, "The lower bainite transformation and the significance of carbide precipitation," *Acta Metallurgica,* vol. 28, pp. 1103-1114, 8// 1980.
[76] W. Pitsch, "Der Orientierungszusammenhang zwischen Zementit und Austenit," *Acta Metallurgica,* vol. 10, pp. 897-900, 9// 1962.
[77] M.Goune, ALEMI meeting, Stockholm 2009.
[78] M. H. Loretto, *Electron beam analysis of materials,* 2nd ed. Chapman & Hall: London ; 1994.
[79] W. Z. Zhang and X. P. Yang, "Identification of singular interfaces with Δgs and its basis of the O-lattice," *Journal of Materials Science,* vol. 46, pp. 4135-4156, 2011/06/01 2011.
[80] W. Z. Zhang, F. Ye, C. Zhang, Y. Qi, and H. S. Fang, "Unified rationalization of the Pitsch and T–H orientation relationships between Widmanstätten cementite and austenite," *Acta Materialia,* vol. 48, pp. 2209-2219, 5/29/ 2000.
[81] J. M. Howe and G. Spanos, "Atomic structure of the austenite-cementite interface of proeutectoid cementite plates," *Philosophical Magezine A,* vol. 79, pp. 9-30, 01/01 1999.
[82] D. Qiu and W. Z. Zhang, "A systematic study of irrational precipitation crystallography in fcc-bcc systems with an analytical O-line method," *Philosophical Magazine,* vol. 83, pp. 3093-3116, // 2003.

[83] D. Qiu and W. Z. Zhang, "A TEM study of the crystallography of austenite precipitates in a duplex stainless steel," *Acta Materialia,* vol. 55, pp. 6754-6764, 12// 2007.

[84] T.Nagano and M.Enomoto, "Calculation of the Interfacial Energies between α and γ Iron and Equilibrium Particle Shape," *Metallurgical and Materials Transactions A,* vol. 37A, pp. 929-937, 2006.

[85] X. Gu and W. Zhang, "An energetic study on the preference of the habit plane in fcc/bcc system," *Solid State Phenomena,* vol. 172-174, pp. 260-266, 2011.

[86] H. K. D. H. Bhadeshia and J. W. Christian, "Bainite in steels," *Metallurgical Transactions A,* vol. 21, pp. 767-797, 1990/03/01 1990.

[87] M. Hillert, "Paradigm shift for bainite," *Scripta Materialia,* vol. 47, pp. 175-180, 8/2/ 2002.

[88] R. F. Hehemann, K. R. Kinsman, and H. I. Aaronson, "A debate on the bainite reaction," *Metallurgical Transactions,* vol. 3, pp. 1077-1094, 1972/05/01 1972.

[89] P. Kolmskog, A. Borgenstam, M. Hillert, P. Hedström, S. Babu, H. Terasaki, *et al.*, "Direct Observation that Bainite can Grow Below MS," *Metallurgical and Materials Transactions A,* vol. 43, pp. 4984-4988, 2012/12/01 2012.

[90] K. C. Russell, D. M. Barnett, C. J. Altstetter, H. I. Aaronson, and J. K. Lee, "Strain energy interactions, the To concept and sympathetic nucleation," *Scripta Metallurgica,* vol. 11, pp. 485-490, 6// 1977.

[91] S. Morito, X. Huang, T. Furuhara, T. Maki, and N. Hansen, "The morphology and crystallography of lath martensite in alloy steels," *Acta Materialia,* vol. 54, pp. 5323-5331, 11// 2006.

[92] R. W. K. Honeycombe and R. F. Mehl, "Transformation from austenite in alloy steels," *Metallurgical Transactions A,* vol. 7, pp. 915-936, 1976/07/01 1976.

[93] R. Okamoto, A. Borgenstam, and J. Ågren, "Interphase precipitation in niobium-microalloyed steels," *Acta Materialia,* vol. 58, pp. 4783-4790, 8// 2010.

[94] C. R. Hutchinson, A. Fuchsmann, and Y. Brechet, "The diffusional formation of ferrite from austenite in Fe-C-Ni alloys," *Metallurgical and Materials Transactions A,* vol. 35, pp. 1211-1221, 2004/04/01 2004.

[95] G. Ghosh and G. B. Olson, "Precipitation of paraequilibrium cementite: Experiments, and thermodynamic and kinetic modeling," *Acta Materialia,* vol. 50, pp. 2099-2119, 5/8/ 2002.

[96] M. Enomoto, W. F. Lange, and H. I. Aaronson, "The kinetics of ferrite nucleation at austenite grain edges in Fe-C and Fe-C-X alloys," *Metallurgical Transactions A,* vol. 17, pp. 1399-1407, 1986/08/01 1986.

[97] T. Tanaka, H. I. Aaronson, and M. Enomoto, "Nucleation kinetics of grain boundary allotriomorphs of proeutectoid ferrite in Fe-C-Mn-X2 alloys," *Metallurgical and Materials Transactions A,* vol. 26, pp. 547-559, 1995/03/01 1995.

[98] J. Ågren, "A revised expression for the diffusivity of carbon in binary Fe-C austenite," *Scripta Metallurgica,* vol. 20, pp. 1507-1510, 11// 1986.